DYNAMICAL AND THERMODYNAMICAL INFLUENCES OF THE TROPICS AND MIDLATITUDES ON ARCTIC HYDROCLIMATE VARIABILITY

A Dissertation
Presented to
The Academic Faculty

By

Bradley M. Hegyi

In Partial Fulfillment
Of the Requirements for the Degree
Doctor of Philosophy in the
School of Earth and Atmospheric Sciences

Georgia Institute of Technology

August 2015

DYNAMICAL AND THERMODYNAMICAL INFLUENCES OF THE TROPICS AND MIDLATITUDES ON ARCTIC HYDROCLIMATE VARIABILITY

Approved by:

Dr. Yi Deng, Advisor
School of Earth and Atmospheric Sciences
Georgia Institute of Technology

Dr. Robert X. Black
School of Earth and Atmospheric Sciences
Georgia Institute of Technology

Dr. Jingfeng Wang
School of Civil and Environmental Engineering
Georgia Institute of Technology

Dr. Violeta Toma
School of Earth and Atmospheric Sciences
Georgia Institute of Technology

Dr. Zhigang Peng
School of Earth and Atmospheric Sciences
Georgia Institute of Technology

Date Approved: April 28, 2015

ACKNOWLEDGEMENTS

This dissertation is a product of the love, support, and guidance of several important people. I would like to thank the following people and organizations who have helped make the research and preparation of this dissertation possible. First, I would like to thank my advisor Dr. Yi Deng and Dr. Robert X. Black, who were the primary influence on my research throughout my doctoral studies. I would also like to recognize the efforts and input of my PhD defense committee members, Dr. Violeta Toma, Dr. Zhigang Peng, and Dr. Jingfeng Wang. I am grateful for the support of NASA, specifically through the NESSF fellowship and a future postdoctoral research opportunity. I am also grateful for former officemates and research group members who have shaped my research in both large and small ways. Special recognition and thanks goes to Rebecca Westby, my officemate from day one at Georgia Tech, for her support, manuscript-editing acumen, and baking skills.

Finally, on a personal note, I would like to thank my parents, who have always encouraged me to achieve and have always given me steady and loving support throughout my college experience, in the almost 10 years since I started at Purdue University in 2005. Last but not least, I give my heartfelt thanks to my fiancée and teammate for life Andrea Lemieux, for her patience through all of the triumphs and trials in the last 3 years as a graduate student at Georgia Tech.

TABLE OF CONTENTS

LIST OF TABLES

LIST OF FIGURES

LIST OF ABBREVIATIONS

AL	Aleutian Low
AO	Arctic Oscillation
CERES	Clouds and the Earth’s Radiant Energy System (project)
CESM	Community Earth System Model
CMAP	CPC Merged Analysis of Precipitation
CPC	Climate Prediction Center
CPW	Central Pacific Warming
EASE	Equal-Area Scalable Earth (grid)
ENSO	El Niño-Southern Oscillation
EP	Eliassen-Palm
EPW	Eastern Pacific Warming
FFT	Fast Fourier Transform
FV	Forced Variability
GPCP	Global Precipitation Climatology Project
HF	High-Frequency
IC	Initial Condition
IPCC	Intergovernmental Panel on Climate Change
IV	Internal Variability
LF	Low-Frequency
LHS	Left-Hand Side
LW	Longwave
MERRA	Modern-Era Retrospective Analysis for Research and Applications
MMC	Mean Meridional Circulation
NAM	Northern Annular Mode
NAO	North Atlantic Oscillation
NASA	National Aeronautics and Space Administration
NCAR	National Center for Atmospheric Research
NH	Northern Hemisphere

NSIDC	National Snow and Ice Data Center
OLR	Outgoing Longwave Radiation
PNA	Pacific-North American (teleconnection pattern)
QBO	Quasi-Biennial Oscillation
QG	Quasi-geostrophic
RHS	Right-Hand Side
SEKE	Synoptic Eddy Kinetic Energy
SF	Subseasonal Frequency
SMMR	Scanning Multichannel Microwave Radiometer
SSM/I	Special Sensor Microwave/Imager
SSMIS	Special Sensor Microwave Imager/Sounder
SST	Sea Surface Temperature
SW	Shortwave
TNH	Tropical Northern Hemisphere
WACCM	Whole Atmosphere Community Climate Model
WP	Western Pacific (teleconnection pattern)

SUMMARY

The Arctic is an important component of the Earth's climate system, and it is a region dynamically coupled to climate phenomena at lower latitudes, through both atmospheric and oceanic paths. The coupling has significant effects on the hydroclimate variability in the Arctic, including effects on sea ice and Arctic precipitation. In this dissertation, we explore the coupling of the lower latitudes and the Arctic hydroclimate through atmospheric mechanisms with dynamical and thermodynamical components, with a focus on the following examples of variability: i) the decadal variability of boreal winter Arctic precipitation, ii) the variability of the strength of the stratospheric polar vortex in boreal winter, and iii) the initial melt of Arctic sea ice in late boreal spring. The goal of the research is to understand what drives the Arctic hydroclimate variability in each of these examples through improved knowledge of the mechanisms linking them to the tropics and Northern Hemisphere midlatitudes.

In the first part of the analysis, we explore the mechanisms responsible for the decadal variability of boreal winter Arctic precipitation. We find that the decadal variability of cool-season Arctic precipitation is at least partly connected to decadal modulation of tropical central Pacific sea surface temperatures related to the El Niño-Southern Oscillation (ENSO). The modulation can be described as the oscillation between periods favoring central and eastern Pacific warming events [CPW and EPW, respectively], which are two common types of ENSO variability. By analyzing a collection of CPW and EPW events in reanalysis data, we establish the following connecting mechanism. First, the increase of central Pacific SSTs drive a Rossby wave train that destructively interferes with the zonal wavenumber 1 component of the background extratropical planetary wave in the subpolar

region. Next, as a result of this interference, the magnitude of the vertical Rossby wave propagation from the troposphere to the stratosphere decreases and the stratospheric polar vortex strengthens. Finally, the strengthening of the vortex translates into a tendency towards a positive Arctic Oscillation (AO) in the troposphere and a poleward shift of the Northern Hemisphere midlatitude storm tracks, increasing moisture transport from lower latitudes and increasing total Arctic precipitation.

In a further investigation of a crucial component of the above mechanism, the initial response of the stratospheric polar vortex to the influence of CPW and EPW is investigated. A 20-member ensemble run of an idealized model experiment in the NCAR Whole Atmosphere Community Climate Model (WACCM) is conducted with prescribed CPW and EPW pattern SST anomalies. Both CPW and EPW events weaken the polar vortex in the ensemble mean. The weakening is mainly tied to changes in the eddy-driven mean meridional circulation, with some contribution from eddy momentum flux convergence. There is a significant spread between ensemble members with identical CPW and EPW forcing, where a few of the ensemble members exhibit a weak strengthening response. The initial conditions of the extratropical atmosphere and subsequent internal variability after the introduction of the CPW and EPW forcing help drive the spread in response between individual members.

In the last part of the analysis, using MERRA reanalysis data, the means by which atmospheric eddies affect the trend and variability of the initial melt of Arctic sea ice are explored. We focus specifically on the effects of lower troposphere (i.e. 1000-500 mb average) meridional heat transport by atmospheric eddies, a dynamical component of the atmospheric eddy mechanism, and eddy-generated surface downwelling shortwave and longwave radiation anomalies, a thermodynamical component. Although in a climatological sense, atmospheric eddies in all major frequency bands transport heat poleward into the Arctic, we find that the lower-troposphere eddy meridional heat transport does not contribute to the trend of an earlier initial melt date. However, eddy heat transport still plays an important role in the initialization of individual episodes of initial melt with large areal coverage. In the investigation of two specific episodes, the meridional heat transport term that represents the interaction between the eddy wind and mean temperature fields (i.e. the product of the meridional eddy wind and the mean temperature fields) is most associated with the initial melt in both episodes. Additionally, melt in one of the episodes is also associated with surface downwelling longwave and shortwave radiation anomalies, a result of eddy-generated cloud cover anomalies. Therefore, in individual melt events, the combination of direct eddy meridional heat transport and surface longwave and eddy-driven shortwave radiation anomalies may significantly contribute to the initial melt of Arctic sea ice. This combination may be especially important in episodes where significant initial melt occurs over a large area and over a period of a few days.

CHAPTER 1

INTRODUCTION

1.1 The Arctic climate system

The Arctic is the region encompassing the North Pole and the highest northern latitudes (Figure 1.1). There are many definitions of the southern boundary of the Arctic region that depend on geography, biology, and the characteristics of the cryosphere (e.g. Huntington et al. 2005). The Arctic, for the purposes of this dissertation, is defined as all areas north of 70 degrees North latitude. In the following subsections, the important components of the Arctic climate system during the warm and cool season are described, including the characteristics that are important in describing hydrodynamic variability in the Arctic region.

Figure 1.1. Map of the Arctic region with boundary used for the definition of the Arctic region in this dissertation highlighted in red. (Source: UT Perry-Castaneda Library)

1.1.1 Cool Season (October-April)

In the cool season, the Arctic climate system is dominated by the presence and growth of the cryosphere, particularly sea ice, and the low incoming solar radiation flux. Both phenomena have crucial effects on the surface water and energy budgets. Sea ice cover rapidly increases in areal coverage in the months of October, November, and December, and reaches peak coverage in early March (Figure 1.2 and 1.3a). The presence of sea ice limits the exchange of heat and moisture between the surface ocean and the atmosphere. Local heat and water vapor surface fluxes from the ocean are confined to small-scale fissures in the ice, called leads, that are the result of the local divergence of the ice due to local differential wind stress on the ice (e.g. Andreas et al. 1979). Also the presence of sea ice cover greatly increases the surface albedo over the ocean, increasing the amount of incoming solar radiation reflected and reducing the amount of solar radiation absorbed at the surface. Sea ice has a much higher albedo than the ocean surface (approximately 0.75 for dry snow-covered ice versus 0.1 for open water, Agarwal et al. 2011). Because of the low values of incoming solar radiation, the direct effect of the high albedo on the surface energy budget is small. However, the high albedo is important in the consideration of the net surface radiative impact of clouds. Due to the presence of sea ice and snow cover, the cloud radiative forcing is positive during the cool season over the areas of the Arctic covered by ice and snow (e.g. Intrieri et al. 2002), since the reflection of incoming solar radiation by clouds is not much greater than the reflection by the ice surface. Thus, in combination with the low incoming solar radiation flux and high surface albedo, clouds have little overall effect in the shortwave surface radiation budget, and their effects are primary found in the longwave radiation budget.

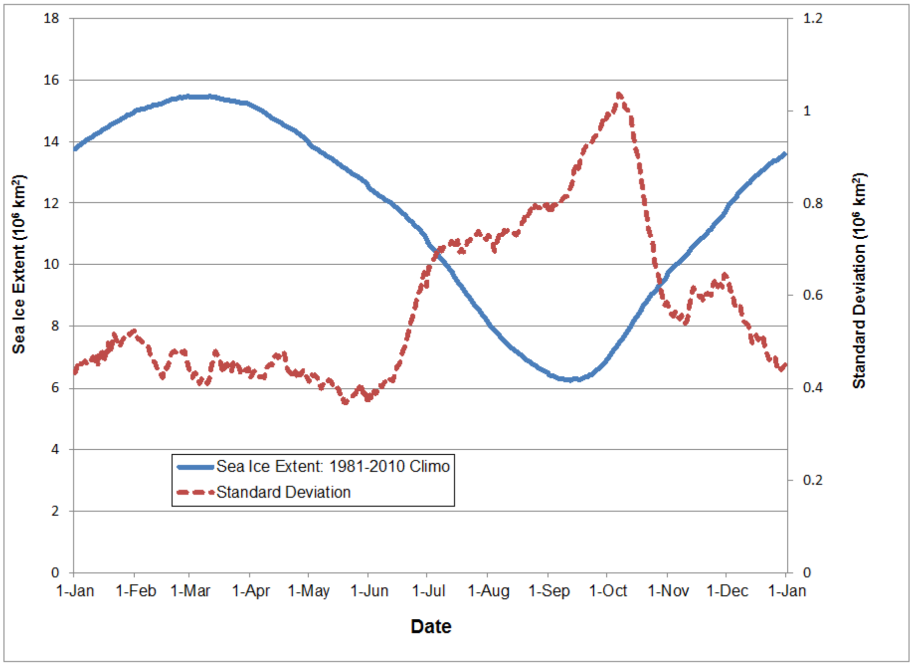

Figure 1.2. 1981-2010 climatology of Arctic sea ice extent (units: 10^6 km^2, solid blue line) and the interannual standard deviation for each date (red dashed line). Sea ice extent data and standard deviation values derived from Arctic Sea Ice Index dataset from the National Snow and Ice Data Center (NSIDC).

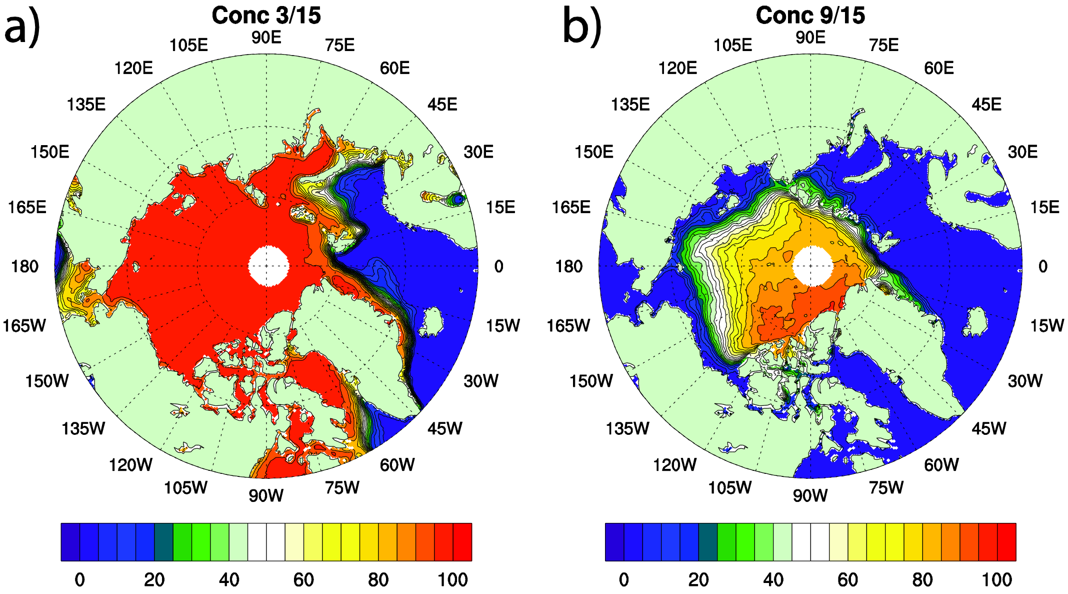

Figure 1.3. 1979-2012 mean sea ice concentration on a) March 15 and b) September 15, which are dates near the sea ice extent maximum and minimum, respectively. Concentration data is derived from the SMMR SSM/I-SSMIS passive microwave satellite data (Cavalieri et al. 1996).

Because of the limited heat and moisture exchanges between the surface ocean and the atmosphere under the cover of sea ice, influences remote to the Arctic play a crucial role in the cool season surface energy and water budget. In particular, the transport of heat and moisture from lower latitudes by atmospheric eddies is an important term in the Arctic surface energy budget (Peixoto and Oort 1992). By definition, atmospheric eddies are disturbances on the time-mean flow. Heat and moisture is transported through the interaction of the eddy wind and heat/moisture fields. Several examples of eddy influence on the surface energy and water budget exist across the Arctic. In the Atlantic sector of the Arctic (60°W-30°E longitude), high-frequency eddy (i.e. cyclone) meridional heat and moisture transport is a crucial source of heat and moisture in the region. The increased meridional moisture transport into the Arctic in the Atlantic sector corresponds to the northeastern flank of the Atlantic storm track, an area of climatologically increased cyclone activity (Simmonds et al. 2008). In the Arctic Ocean north of Alaska, atmospheric blocking patterns, a manifestation of low-frequency atmospheric transient eddies, have been shown to be associated with intrusions of moisture from lower latitudes (Woods et al. 2013).

Another important dynamical component of the Arctic climate dynamics in the cool season is low-frequency modes, which are defined anomalous patterns that exist in the geopotential height or in other fields and that explain part of the observed climate variability. Of particular importance to the Arctic is the Northern Annular Mode (NAM) (Thompson and Wallace 1998, 2000). The NAM is manifested as the Arctic Oscillation in the troposphere and the stratospheric polar vortex in the stratosphere. By definition, the Arctic Oscillation loading pattern is the leading mode of variability in the monthly mean

1000mb height (CPC definition), with a negative center over the Arctic Ocean and positive centers over the subpolar and midlatitudes in the North Atlantic and North Pacific. AO variability has been linked to cool season sea ice variability (Rigor et al. 2002), and is positively correlated with North Atlantic cyclone activity (Serreze et al. 1997; Simmonds et al. 2008). The stratospheric polar vortex is a cyclonic vortex found in the polar stratosphere during the cool season and is characterized by strong westerly winds maximized around 65°N longitude and above 250 mb (e.g. Andrews et al. 1987; Black 2002). The strength of the vortex is variable, constantly perturbed by breaking stationary Rossby wave activity propagating from the troposphere, imparting easterly momentum on the vortex (Waugh and Polvani 2010). These Rossby waves are the primary source of intraseasonal variability of the strength of the polar vortex, and in the extreme, can force complete breakdown of the vortex and a sudden stratospheric warming (e.g. Matsuno 1970). These Rossby waves originate in the tropics and midlatitudes and are forced by either orographic or thermal forcing at these latitudes, such as from anomalous tropical convection. The exact connecting mechanism that extends the Rossby wave influence from the Tropics to the Arctic will be discussed in section 1.3.

1.1.2 Warm Season (May-September)

In the warm season, the characteristics of the important features of the Arctic climate are much different relative to their state in the cool season. Changes include i) increased downwelling shortwave radiation at the surface and ii) reduction of area of the ocean surface covered by sea ice (Figure 1.3). Increased downwelling shortwave radiation at the surface results in the cloud radiative forcing becoming less positive (e.g. Intrieri et al. 2011) as clouds reflect more incoming solar radiation and their cooling effect in the shortwave component of the surface energy budget increase. Additionally, the increased solar input raises surface temperatures such that the surface ice and snow begins to melt. During the early part of the warm season, mean temperatures across the Arctic increase rapidly and plateau to near freezing (Figure 1.4). As a result of the increased surface temperatures, melt begins to occur over the ice and snow surfaces. Subsequently, the mean surface albedo in the Arctic decreases, increasing the absorption of incoming solar radiation at the surface (Agarwal et al. 2011). Melting and the appearance of open ocean waters significantly reduces the surface albedo, from 0.85 for snow covered ice to 0.3 for meltwater and 0.1 for open ocean (Perovich and Polashenski 2012; Figure 1.5). The melting leads to more absorption of incoming solar radiation at the surface and more melt, leading to the ice-albedo positive feedback. Later in the melt season, after the ice-albedo feedback has initiated, large areas of open ocean appear across the Arctic basin. As a result, the area where the ocean and atmosphere can more fully interact increases, increasing the transfer of heat and especially moisture from the ocean surface to the atmosphere.

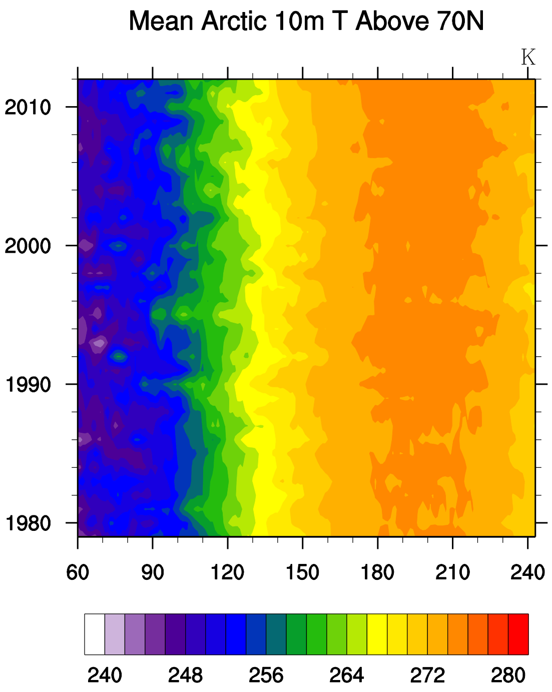

Figure 1.4. Daily mean 10-meter surface temperatures north of 70°N latitude for the years 1979-2012. Day values on the horizontal axis correspond to the number of days after January 1. Day 60 corresponds to March 1.

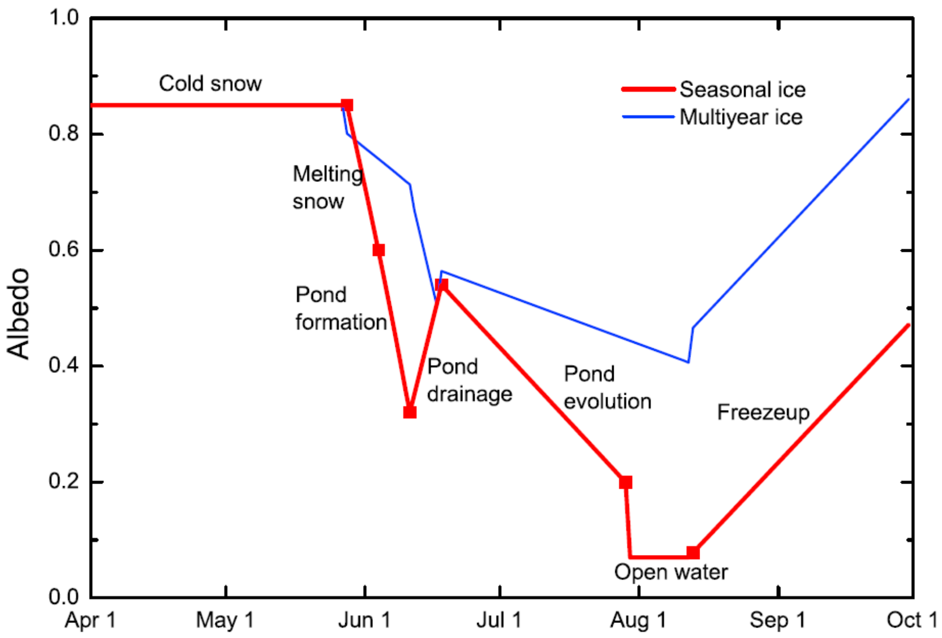

Figure 1.5. A model time evolution of albedo for first year and multiyear sea ice, corresponding to sea ice with a melt onset of May 29 and freeze up on August 13. (Figure 3 from Perovich and Polashenski 2012).

As a result of the combination of the increases in shortwave radiation and loss of sea ice cover, the importance of local dynamic and thermodynamic processes in the Arctic increase. In the cool season, with mean temperatures well below freezing across most of the Arctic Ocean outside of the Atlantic sector, positive temperature anomalies do not result in appreciable melting. Thus, the surface albedo is not sensitive to temperature anomalies driven by atmospheric dynamical processes or local surface radiative anomalies. In contrast in the warm season, with mean surface temperatures near the melting point of snow and ice, temperature anomalies or anomalous inputs of heat from the atmosphere can initiate or increase the rate of melting, significantly reducing the surface albedo. Additionally, with a more interactive ocean, new sources of heat and especially moisture exist within the Arctic, which represent a local contribution to the heat and moisture budget in the Arctic that does not exist over a large spatial scale in most of the Arctic basin during the cool season.

Supporting the shift to the increased importance of local dynamic and thermodynamic processes are the changes to the dominant large-scale climate features and the distribution of cyclone activity in the Arctic. In the warm season, the stratospheric and tropospheric components of the Northern Annular Mode are much weaker than in the cool season. The stratospheric polar vortex breaks down at the end of the cool season and is replaced with weaker easterly winds (e.g. Andrews et al. 1987). The signature of the AO pattern still exists in the warm season in the troposphere, but the index describing it does not reach the extremes that are seen in the cool season. Thus the influence of the AO on Arctic climate is weaker. Additionally, cyclone count decreases approximately 10-15%

relative to the number of cool season cyclones (Simmonds et al. 2008). The areal distribution of the cyclone activity is not concentrated preferentially in the Atlantic sector, near the northeastern flank of the Atlantic storm track, as in the cool season, but is more evenly distributed across the Arctic Ocean (Simmonds et al. 2008). Also cyclones local to the Arctic form across eastern Siberia and Alaska (Serreze et al. 2001). Summer Arctic cyclones have a slightly longer lifespan (Zhang et al. 2004) and still contribute significantly to the transport of heat and moisture from lower latitudes into the Arctic (Peixoto and Oort 1990).

The key differences between the Arctic cool and warm season climate conditions are summarized in Table 1.1.

Table 1.1. Summary of the important differences in the state of the Arctic climate in the warm season (May-September) relative to the cool season (October-April).

Warm Season Conditions Relative to Cool Season	*Consequences*
Increased Downwelling Shortwave Radiation	- *Increased surface temperatures* - *Cloud radiative forcing becomes less positive (i.e. clouds warm the surface less than the cool season)*
Increased Sensitivity of Surface Albedo to Temperature during Melt	- *Temperature anomalies have greater effects on surface energy budget, especially in the initial melt season (late boreal spring)* - *Shortwave feedback mechanism prevalent (decreased albedo->more SW absorption->more warming and melt->decreased albedo)*
Increased Area of Open Ocean	- *Atmosphere and surface ocean are more coupled, with greater exchange of heat and moisture at the surface*
Weaker AO and Disappearance of Stratospheric Polar Vortex	- *Less influence of cool season Rossby wave train dynamical mechanism, crucial to climate variability in the cool season*
More Uniform Distribution of Cyclone Activity	- *Cyclones, and their associated heat and moisture transport from lower latitudes, affect the entire Arctic basin*

1.2 Trend Characteristics of Sea Ice and Temperatures across the Arctic

Much of the focus on recent changes in the Arctic climate has been on the trends in sea ice cover, particularly the trend of the September minimum extent, and the surface temperatures across the Arctic in both the warm and cool seasons. Since 1979, a declining trend in sea ice cover has been observed in all months, but the magnitude of the trend is greatest in the warm season, in the months of June, July and August (Parkinson and

Cavalieri 2008). In the cool season, the greatest negative trend has been observed across the Atlantic sector of the Arctic (i.e. the Greenland, Norwegian, Barents, and Kara Seas, Figure 1.6a). The trend is near zero across the central Arctic Ocean and marginal seas north of eastern Siberia and North America, which remains completely ice-covered in the cool season (Parkinson and Cavalieri 2008). Conversely, in the warm season, the trend is greatest across the central Arctic Ocean, and the margins of the Arctic north of eastern Siberia and northwestern North America (Figure 1.6b). In both seasons, the greatest declining trend in sea ice concentration is located on the margins of the sea ice, where the sea ice edge meets an area of open water.

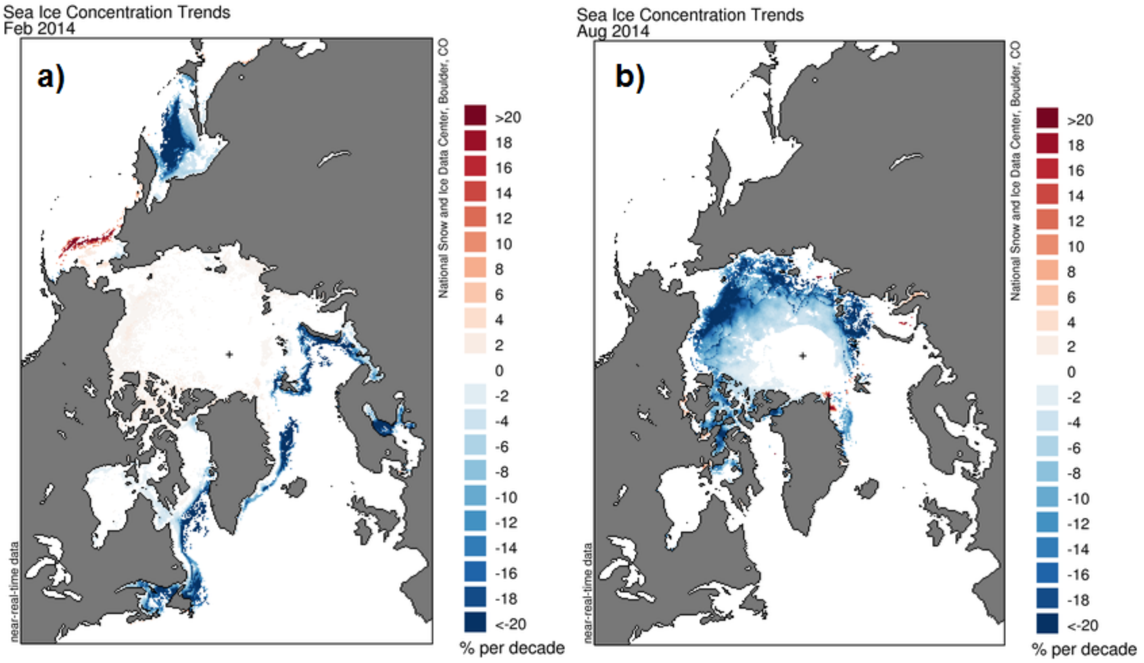

Figure 1.6. Trend in sea ice concentration in the 1979-2014 period for the month of a) February and b) August (units % per decade). A positive (negative) trend is shaded in red (blue). Source: NSIDC.

The decreased sea ice cover is a visible manifestation of the temperature trends across the Arctic. Relative to annual mean surface temperature increases in other regions in the world, the Arctic exhibits a positive trend approximately double the magnitude of the other regions in both observations (e.g. Serrreze and Barry 2011) and IPCC models (e.g. Winton 2006). This phenomenon in the recent trend in mean surface temperature is known as Arctic amplification. Contributions to Arctic amplification include sea ice loss and the extra absorption of incoming solar radiation during the summer by the ocean mixed layer and subsequent release during the cool season (Serreze and Barry 2011), surface albedo feedbacks (e.g. Perovich et al. 2007), increased horizontal atmospheric and oceanic heat flux convergence (e.g. Chylek et al. 2009; Yang et al. 2010), and cloud cover and water vapor feedbacks (e.g. Graversen and Wang 2009).

1.3 Remote Atmospheric Influences on Arctic Climate Variability

Arctic hydroclimate variability is initiated by phenomena originating locally within the Arctic and outside of the Arctic region. For climate phenomena outside of the Arctic region to influence Arctic hydroclimate variability, a connecting physical mechanism is required to facilitate the communication between regions. Primary mechanisms that facilitate the communication between the lower latitudes and the Arctic include midlatitude cyclones, described in section 1.1, and Rossby wave trains, a set of stationary waves that extend from the Tropics to the middle and high latitudes in both hemispheres. In the Earth's climate system as a whole, the connections between the lower latitudes and the Arctic directly and indirectly support Arctic amplification, defined the increased warming trend of the Arctic relative to other regions of the Earth's climate system (e.g. Manabe and Wetherald 1975).

1.3.1 The Rossby Wave Train

Rossby waves are a type of atmospheric wave important for large-scale mechanisms that link the lower latitudes to the Arctic, especially in winter season. The interaction between the mean atmospheric flow and both thermal and orographic forcing results in an atmospheric Rossby wave response. In the tropics, anomalous upper tropospheric heating due to persistent anomalous tropical convection, such as associated with ENSO, is a primary source of Rossby waves (e.g. Hoskins and Karoly 1981). The characteristics of the response in terms of propagation and magnitude is highly dependent on the vertical profile of the forcing, the location and strength of westerlies in the subtropics and midlatitudes, the wavelength of the forced Rossby wave, and the location of the anomalous convection (e.g. Sardeshmukh and Hoskins 1988). Persistent convection anomalies in the tropics result in a relatively stationary pattern of crests and troughs, which is defined as a Rossby wave train (Figure 1.7). Rossby wave trains with a long wavelength tend to have a significant poleward propagation component when originating from the tropics, while shorter wavelength Rossby wave trains remain trapped within the midlatitudes (Hoskins and Karoly 1981).

Because of the poleward propagation of the longwave Rossby wave trains, these Rossby wave trains are an important mechanism or pathway by which the tropics can communicate with the midlatitudes and polar regions, in a large-scale dynamical sense. Directly, the geopotential height anomalies can propagate into the Arctic and change the large-scale atmospheric flow, affecting the amount and distribution of heat and moisture transport into the Arctic. A projection of this direct propagation appears in the indices of important low-frequency modes in the Northern Hemisphere cool season. For example, ENSO generates a Rossby wave train that projects onto the positive phase of the Pacific North American (PNA) pattern (Horel and Wallace 1981). Indirectly, the Rossby wave train affects the strength of the stratospheric polar vortex, which indirectly affects the Arctic climate. This occurs though the projection of the Rossby wave train on the climatological wave pattern of waves that preferentially propagate into the stratosphere. The projection and subsequent interference changes the amount of wave propagation into the Arctic stratosphere, the amount of wave breaking perturbation of the vortex, and ultimately the strength of the stratospheric polar vortex (e.g. Garfinkel and Hartmann 2008). In the troposphere, the change in the strength of the vortex projects onto the AO pattern and thus affects tropospheric heat and moisture transport into the Arctic.

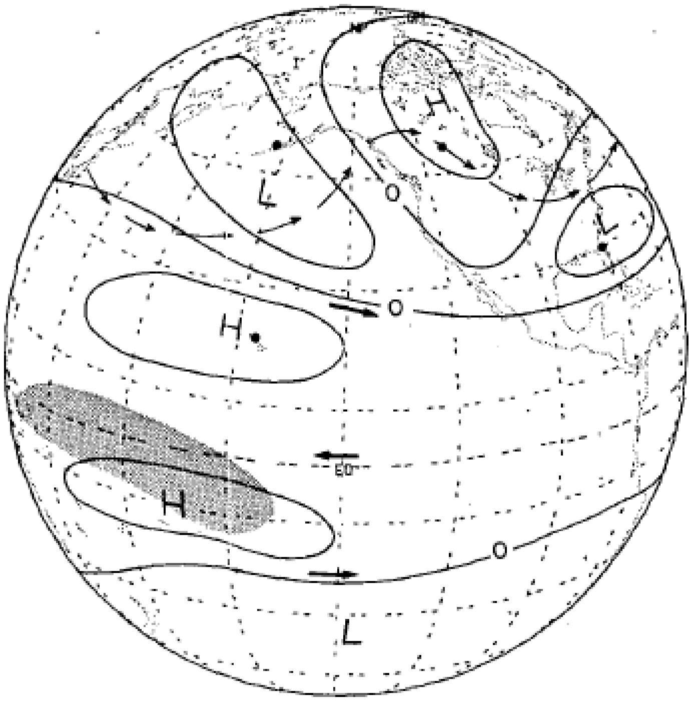

Figure 1.7. Schematic of global Rossby wave train pattern forced by warm sea surface temperatures in the equatorial Pacific in Northern Hemisphere winter. (Figure 11 from Horel and Wallace 1981).

The Rossby wave trains that affect the Arctic climate are most prevalent in the cool season. The jet streams in the Northern Hemisphere weaken and shift northward in the warm season, reducing the ability for forced Rossby waves to propagate poleward and weakening the projection onto low-frequency modes (Ding et al. 2011). Additionally, ENSO and the cool season persistent anomalous convective patterns are weaker in the warm season relative to the cool season. Thus, the influence of Rossby wave trains on Arctic climate generated from the Tropics is decreased in the warm season, relative to the cool season.

1.3.2 Polar Warming Amplification

On longer timescales, the connecting mechanisms that link lower latitudes to variability in Arctic hydroclimate variability have been implicated as driving mechanisms in polar warming amplification. Both heat transport from lower latitudes into the Arctic and the distribution of cloud cover across the Arctic can be directly or indirectly modified by Rossby wave trains and atmospheric eddy activity. Heat transport and the radiative effects of cloud cover have been implicated as components leading to polar warming amplification. Increased heat transport from lower latitudes to the Arctic has been shown to be an important contributor to polar warming amplification. For example, Cai (2005) attributed approximately 25% of high-latitude warming to enhanced atmospheric heat transport in an idealized climate model experiment. Cloud feedbacks have also been shown to contribute to the polar warming amplification, particularly through downwelling infrared radiation (e.g. Taylor et al. 2013). Additionally, a mechanism has been suggested where the direct propagation of Rossby waves propagating from the Tropics directly results in Arctic warming through adiabatic processes, with the warming enhanced by subsequent increasing in downwelling LW radiation from enhanced warming and cloud cover (i.e. the TEAM mechanism, Lee 2011; Lee 2012). Rossby wave trains generated by tropical convection are a crucial component of this proposed mechanism.

1.4 Summary of Research Objectives

In this dissertation, we explore the coupling of the Arctic hydroclimate and the Tropics and midlatitudes through atmospheric dynamical mechanisms. The coupling is explored in both the cool and warm seasons, with a focus on the following important examples of Arctic hydroclimate variability: i) the decadal variability of boreal winter Arctic precipitation, ii) the variability of the strength of the stratospheric polar vortex in boreal winter, and iii) the initial melt of Arctic sea ice in late boreal spring. The goal of the research presented here is to increase our understanding of what drives each example of Arctic variability through better understanding of the mechanisms linking them to variability in lower latitudes. The following list highlights the science questions that will be explored within the manuscript, and the steps that will be taken to answer the science questions.

- Describe the relationship between the decadal modulation of ENSO and the decadal variability of Arctic precipitation. How does decadal SST variability directly and indirectly contribute to the decadal variability of Arctic precipitation? What atmospheric processes are involved in the connection? (Chapter 2)
- Quantify the response of the stratospheric polar vortex to CPW and EPW warming. What are the differences in the initial response of the stratospheric polar vortex to

the SST anomalies associated with central and eastern Pacific warming (CPW and EPW, respectively)? (Chapter 3)

- Determine the importance of initial conditions of the extratropical and polar atmosphere in the sign and magnitude of the change in the strength of the polar stratospheric vortex in response to CPW and EPW warming. How is the response of the vortex to CPW and EPW dependent on the initial state of the extratropical circulation? (Chapter 3)
- Investigate episodes of large areal initial sea ice melt in the late boreal spring across the Arctic. Through which processes do atmospheric eddies contribute to the initial melt of Arctic sea ice? Is the dynamical component of the atmospheric eddy mechanism, through the transport of heat from lower latitudes, or the thermodynamic component of the atmospheric eddy mechanism, through changes in downwelling longwave and shortwave radiation via eddy-driven anomalies in cloud cover, more important to the initial melt? (Chapter 4)

CHAPTER 2

DYNAMICAL INFLUENCE OF TROPICAL PACIFIC SEA SURFACE TEMPERATURES ON THE DECADAL-SCALE VARIABILITY OF COOL-SEASON ARCTIC PRECIPITATION

2.1 Motivation and Background

The accumulation of snow and growth of ice cover in the Arctic during the Northern Hemisphere (NH) winter are important to the Earth's climate and depend significantly on the amount of precipitation that falls within the Arctic. As noted in the introduction, the Arctic cool season is characterized by low temperatures and broad sea-ice cover that limit local evaporation, thus moisture influx from lower latitudes provides the most important source of moisture for Arctic precipitation. The meridional transport of moisture into the Arctic is known to be primarily associated with synoptic-scale eddies (Peixoto and Oort, 1992; McBean et al., 2005) that tend to organize themselves into distinct storm tracks in winter (Blackmon 1976). Significant correlations are found between the activity of midlatitude cyclones (i.e., surface signatures of synoptic eddies) and the total moisture transport into the Arctic and by extension, total Arctic precipitation (e.g. Sorteberg and Walsh 2008). It is also well established that synoptic eddy activity within major storm tracks, such as the ones over the North Pacific and North Atlantic, is dynamically coupled to various atmospheric low-frequency modes, including the North Atlantic Oscillation (NAO) and the Arctic Oscillation (AO) (e.g. Thompson and Wallace 1998). Both the NAO and AO variability prove to be crucial in modulating winter cyclone activity north of 60°N (Serreze et al. 1997) and determining the variability in sea-ice cover and sea-ice motion across the Arctic Ocean (Deser et al. 2000; Dickson et al. 2000; Rigor et al. 2002).

Variability in the AO/NAO has been directly and indirectly linked by previous studies to SST variability in the tropical Pacific (i.e. ENSO), with the Rossby wave train as a dynamical intermediate. The seasonality of the AO and decadal-scale changes in the NAO have been linked to SST variability in the western tropical Pacific (between 140°E-170°W) (Jia et al. 2009; King and Kucharski 2006; Kucharski et al. 2006). Jia et al. 2009 and Kucharski et al. 2006 establish the link through the *direct* propagation of anomalous Rossby waves from the tropical Pacific to the AO/NAO action center in the North Atlantic and Arctic Oceans and projection onto the AO/NAO patterns. The indirect link, where the anomalous Rossby wave propagation does not directly propagate and project onto the AO/NAO, can be distilled from studies that linked El Niño/Southern Oscillation (ENSO) variability to the increased occurrence of sudden stratospheric warmings (SSWs) in the NH polar region during boreal winter (e.g. Taguchi 2010; Taguchi and Hartmann 2006). These studies suggest that SST anomalies in the tropical Pacific due to El Niño result in an increased upward propagation of wave energy associated with the wavenumber-1 component of the extratropical planetary wave. The enhanced wave forcing in the stratosphere leads to the breakdown of the NH stratospheric polar vortex and an increase in the occurrence of SSWs. Although the index of the AO is typically defined from loading patterns in the sea level pressure (SLP) and tropospheric geopotential height field, the variability of the AO has been shown to reflect the changes in the NH stratospheric polar vortex (Baldwin and Dunkerton 1999; Thompson and Wallace 1998).

However, not all warm ENSO events lead to a weakened polar vortex, adding complexity to the indirect connection between ENSO and the AO/NAO. The response depends on the phase of the Quasi-biennial Oscillation (QBO) and ultimately the specific type of extratropical teleconnection patterns excited by the tropical Pacific SST anomalies. Garfinkel and Hartmann 2008 showed that the weakening effect of El Niño on the polar vortex is maximized when the stationary Rossby wave forced by the SST anomalies project onto the Pacific-North America (PNA) pattern (Wallace and Gutzler 1981). The deepening of the Aleutian Low (AL), characteristic of the positive PNA phase, significantly enhances the climatological wavenumber-1 component of the planetary wave and the subsequent upward propagation of planetary wave energy into the stratosphere. The projection of the atmospheric response to the SST anomaly onto other extratropical teleconnection patterns, including the Western Pacific (WP) and tropical Northern Hemisphere (TNH) pattern, does not have the same weakening effect on the polar vortex due to the lack of a significant AL signal that constructively interferes with the climatological wavenumber-1 pattern.

Given the direct and indirect mechanisms by which Rossby wave trains forced by tropical SST anomalies can affect cool season Arctic precipitation and the complexity of the indirect mechanism, it remains unclear how the tropical-extratropical connections discussed above manifest themselves in cool season Arctic precipitation variability and which mechanism facilitates the connection. As an initial investigation, this study focuses on precipitation and aims to quantify the temporal and spatial characteristics of decadal-scale variations in the NH cool-season Arctic precipitation, and to identify tropical forcing factors behind such variations. The direct and indirect effects of tropical SST variability on the Arctic climate, as discussed above, are explored further and inter-compared. Following the introduction, Section 2 describes the data and methods used in the analysis. Major results are reported in Section 3 where the significance of the exact character of the warm ENSO events is emphasized. Section 4 gives the concluding remarks.

2.2 Data and Methods

Monthly precipitation data from both the Climate Prediction Center Merged Analysis of Precipitation (CMAP) (Xie and Arkin 1997) and the Global Precipitation Climatology Project (GPCP) Version 2.1 datasets (Adler et al. 2003) are used to calculate the total Arctic precipitation during each cool season from 1979/1980 to 2008/2009. A total precipitation index is computed as the area-weighted average over all the grid points in each dataset north of the Arctic Circle (66.5°N). To isolate the decadal-scale signals, a 7-year moving-average is applied to the Arctic precipitation index as well as other standard atmospheric fields being analyzed, all of which come from the NASA Modern Era Retrospective-Analysis for Research and Applications (MERRA) reanalysis dataset on a 0.5° latitude × 0.67° longitude grid (Bosilovich et al. 2008; Rienecker et al. 2011). The 7-year moving-average has been used in previous studies that address decadal-scale variability (e.g., King and Kucharski 2006) and the results obtained in our analysis are qualitatively similar despite small changes in the definition of the filter, e.g., 5-year versus 7-year moving-average.

The application of the 7-year moving-average reddens the time series under consideration and reduces the effective number of degrees of freedom (e.g. Garfinkel et al. 2010; Naoe and Shibata 2010). A Monte Carlo approach is adopted to derive statistical significance for all the correlation and regression results that utilize smoothed data (Woollings et al. 2010). Using the correlation calculation as an example, for each of the two smoothed time series of observation, we create a hypothetical time series of equal sample size with its elements drawn randomly and independently from a Gaussian distribution characterized by the same mean and standard deviation of the original, unsmoothed time series of observation. The two hypothetical time series are then smoothed by the same 7-year moving-average filter and the correlation coefficient between these two time series is calculated. This drawing and smoothing process is repeated 5000 times to obtain an empirical probability distribution function (PDF) of the correlation coefficients. The p-value of the correlation coefficient calculated from the original, smoothed time series of observation is finally obtained based upon the percentiles of this empirical distribution.

To quantify the effect of storm track activity and eddy moisture transport on Arctic precipitation, the meridional moisture transport associated with synoptic eddies, $\left\{\overline{v'q'}\right\}$, and the synoptic eddy kinetic energy (SEKE), $\frac{1}{2}\overline{\left(u'^2 + v'^2\right)}$, are both derived from the daily MERRA data, where u, v, q are the zonal wind, meridional wind and specific humidity, respectively. The overbar indicates averaging over the cool season and the prime corresponds to synoptic-scale fluctuations obtained through a 2-6 day Butterworth band-pass filter. $\{\ \}$ indicates mass-weighted vertical averaging between 1000 mb and 600 mb.

To identify the remote (tropical) forcing factors of the Arctic precipitation change, we examined the 7-year smoothed SST field from the Hadley Center Sea Ice and Sea Surface Temperature (HadISST) dataset (Rayner et al. 2003) and the outgoing longwave radiation (OLR) field from the NOAA Interpolated OLR dataset (Liebmann and Smith 1996). The two-dimensional wave activity flux

$$F_s = 0.5 * (p/1000) * < F_{\mathrm{x}}, F_{\mathrm{y}} >$$
$$F_{\mathrm{x}} = \left(\frac{\partial \psi'}{\partial x}\right)^2 - \psi' \frac{\partial^2 \psi'}{\partial x^2}, \quad F_{\mathrm{y}} = \left(\frac{\partial \psi'}{\partial x}\right)\left(\frac{\partial \psi'}{\partial y}\right) - \psi' \frac{\partial^2 \psi'}{\partial x \partial y} \qquad (2.1)$$

(Plumb 1985; Takaya and Nakamura 2001), calculated at 250 mb with MERRA winds, is adopted to reveal the horizontal propagation of stationary Rossby waves from the Tropics as excited by the SST and associated diabatic heating anomalies. p and ψ are the pressure in mb and the streamfunction, respectively. The primes in this equation represent the deviation from the zonal mean. Based upon monthly MERRA winds and temperature, the vertical propagation of planetary wave energy is diagnosed through the quasi-geostrophic form of the Eliassen-Palm (EP) flux that includes spherical geometry considerations,

$$F = < F_{\phi}, F_{\mathrm{p}} >, \quad F_{\phi} = -r_0 \cos(\phi)\overline{v'u'}, \quad \mathrm{F}_{\mathrm{p}} = f r_0 \cos(\phi)\overline{v'\theta'}/\overline{\theta}_p \qquad (2.2)$$

(Equations 3.1a and 3.1b of Edmon et al. 1980). The primes represent the deviation from the zonal mean and the overbars represent the zonal mean. f is the Coriolis parameter, and φ, r_0, and θ are the latitude, the mean radius of Earth, and the potential temperature, respectively. The subscript “p” is the vertical derivative with respect to pressure. A Fast Fourier Transform (FFT) is applied to the 500-mb geopotential height field at each latitude to quantify the changes in the planetary wave power spectrum across different zonal wavenumbers. Similarly calculated are the contributions from the individual wavenumber components to the total anomalies of vertical wave propagation.

2.3 Decadal-scale variability in cool-season Arctic precipitation

Figure 2.1a shows the cool-season Arctic precipitation anomalies (bars) for the period 1979/80 to 2008/09 in GPCP, CMAP and MERRA datasets. The 30-season mean values removed from the three datasets are substantially different; the mean cool-season total Arctic precipitation in GPCP (188.9756 mm) is about 1.93 (1.2) times larger than the corresponding CMAP (MERRA) mean. Despite the differences in the magnitude of the climatology, distinct decadal-scale variations (smoothed solid curves) exist in all three datasets with above normal precipitation found during 1990-1994 and below normal precipitation occurring in 1997-2001. The correlation coefficients among the smoothed curves are in the range of 0.70-0.78 and are all significant at the 90% level, demonstrating the robustness of the decadal-scale signal in the Arctic precipitation. In addition, the correlation coefficients between the unsmoothed Arctic precipitation values of the three datasets range from 0.73 to 0.78 and are all significant at the 99% level, demonstrating the similarity of the representation of interannual variations of the Arctic precipitation in all three datasets, despite the differences in the magnitude of their respective climatology. All three precipitation time series are positively correlated with the smoothed AO index (r=0.5345 for GPCP, r= 0.6356 for CMAP, r=0.4744 for MERRA), with the correlation coefficients for GPCP, CMAP and MERRA significant at the 85%, 90% and 80% level, respectively. Though the length of the observational record severely limits the level of statistical significance derived here, it is fairly evident that increasing Arctic precipitation is typically accompanied by a tendency toward the positive phase of the AO on decadal timescales. In the remaining part of this paper, only results based on the GPCP are presented since the choice of the precipitation data does not affect the conclusions qualitatively.

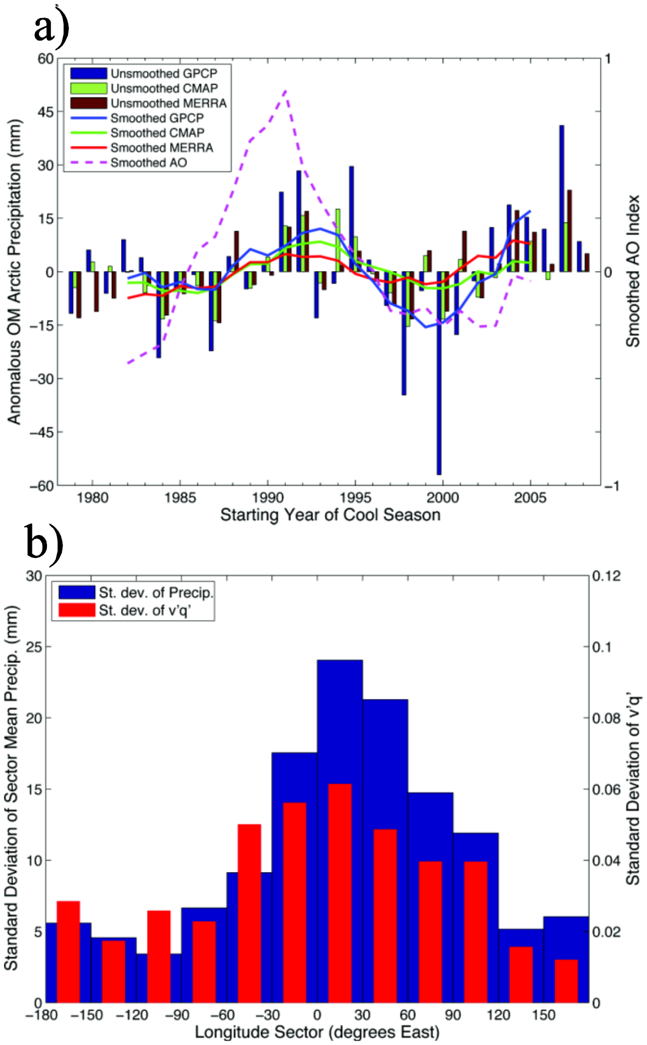

Figure 2.1. a) Annual anomalies of the total cool-season (October-March) Arctic precipitation in GPCP (blue), CMAP (green), and MERRA (red) (in mm). The bars represent the unsmoothed precipitation anomalies, and the solid curves represent precipitation anomalies smoothed by a 7-year running mean filter. Also plotted is the AO index (purple dashed), smoothed by a 7-year running mean filter. b) Distribution of the inter-decadal standard deviation of the GPCP Arctic precipitation in mm (blue) and meridional eddy moisture flux in (m/s)*(g/kg) (red) across different longitude sectors.

The breakdown of the signal in the total Arctic precipitation into different longitudinal sectors (Figure 2.1b) reveals that amplitudes of the decadal-scale variations in precipitation and in the meridional moisture flux associated with synoptic eddies at the Arctic Circle are both greatest in the Atlantic sector of the Arctic (i.e., the Greenland, Norwegian, and Barents Sea). By absolute value the largest standard deviation of the 7-year smoothed precipitation occurs in the sector 0°-30°E, corresponding to the Norwegian Sea. By percentage of the sector mean precipitation, the largest standard deviation is found in the sector 30°-60°E, corresponding to the Barents Sea. The collocation of the maximum inter-decadal standard deviations of precipitation and the synoptic eddy moisture transport demonstrates the importance of synoptic eddies, as part of the North Atlantic storm track, in modulating the decadal-scale variability in Arctic precipitation. Figure 2.2a and 2.2b show respectively the regression of the 850-mb SEKE and lower tropospheric synoptic eddy moisture transport onto the Arctic precipitation index. Associated with high values of Arctic precipitation are an elevated level of synoptic eddy activity north of the Arctic Circle and an increase of poleward eddy moisture transport in the Atlantic sector of the Arctic. Thus the variability of cool-season Arctic precipitation is directly tied to the storm track variability on decadal timescales and the former's connection to the AO, as shown in Figure 2.1a, is established through the coupling between AO variability and storm tracks. The northward shift of the zonal wind jets that accompanies the positive phase of the AO tends to steer more cyclones into the Arctic and leads to a poleward shift of the storm tracks.

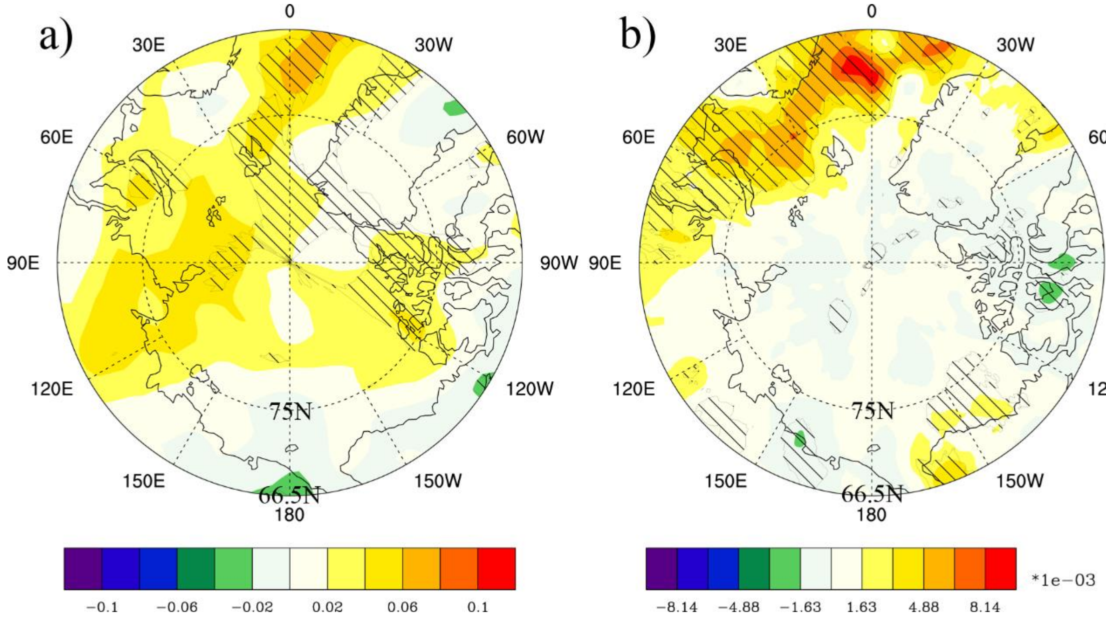

Figure 2.2. a) 850 mb synoptic eddy kinetic energy (SEKE, in J/kg) and b) lower troposphere moisture transport by synoptic eddies (in (m/s)*(g/kg)) regressed onto the Arctic precipitation index. The moisture transport is vertically averaged over 1000-600 mb. Areas with values significant at the 90% level are hatched.

The fact that the decadal-scale variability in Arctic precipitation and the associated synoptic eddy moisture transport is more pronounced in the Atlantic sector of the Arctic compared to the Pacific sector is largely due to the differences in the mean latitudinal position and intensity of the Pacific and Atlantic storm track. The Pacific storm track is primarily zonally oriented with an exit region in the Gulf of Alaska south of the Arctic Circle. On the other hand, the Atlantic storm track has a distinct southwest-northeast tilt with an exit region extending northward across the Arctic Circle. In addition, the climatological Pacific storm track is weaker than the Atlantic storm track in boreal winter (e.g. Chang et al. 2002; Deng and Mak 2005, 2006). When, for example, a zonally symmetric mode, such as AO, shifts toward a positive phase, it is coupled to poleward movement of both the Atlantic and Pacific storm tracks. However, more (intense) cyclones and lower-latitude moisture can reach the interior Arctic in the Atlantic sector due to a stronger and more-poleward-positioned Atlantic storm track. As a result, the strongest coupling among the Arctic precipitation, synoptic eddy moisture transport and storm track occurs in the Atlantic sector rather than in the Pacific sector.

2.4 Connections between the decadal-scale variability in Arctic precipitation and in tropical Pacific SSTs

Figure 2.3a shows the coefficients of regression between the tropical SST and the 7-year-smoothed Arctic precipitation index. Statistically significant positive values are found across the tropical central Pacific (east of 165°E), centered on the equator and extending northeastward into the coast of Baja California. A nearly identical pattern is found when the tropical SST is regressed onto the smoothed October-March-mean AO index. This SST regression pattern across the tropical Pacific bears some similarity to the SST anomaly pattern typical of an El Niño Modoki event (e.g. Figure 5b of Ashok et al. 2007b; Figure 3b of Weng et al. 2009). The extension of positive SST anomalies towards Baja California closely matches the SST anomaly pattern associated with the Central Pacific-type of warming discussed in Yu and Kao 2007 and Kao and Yu 2009. Sun and Yu 2009 reported a decadal-scale modulation of ENSO variability that is characterized by a SST pattern also similar to that in Figure 2.3a. Under this modulation, weak (strong) ENSO periods correspond to a situation where central (eastern) Pacific warming events are favored and the ascending branch of the Walker circulation shifts toward the central (eastern) Pacific. The western and central Pacific dipole in the OLR regression field (Figure 2.3b) is also consistent with this shift of the Walker circulation.

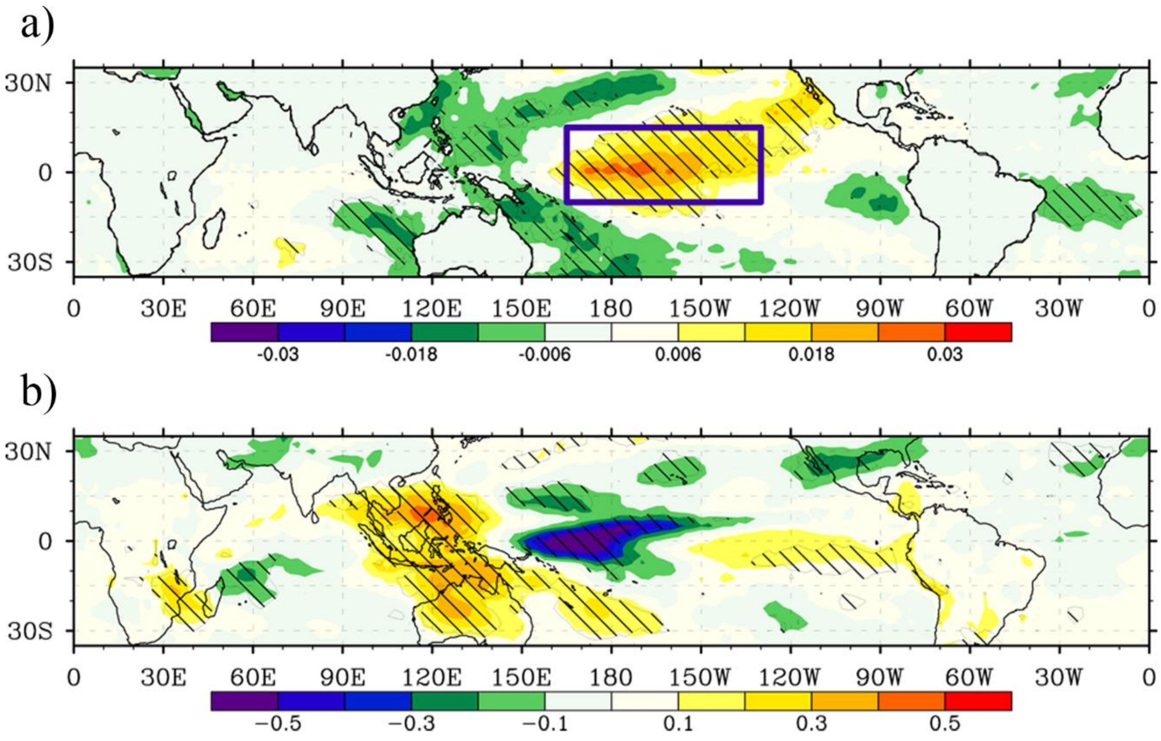

Figure 2.3. a) Sea surface temperature (SST, in K) and b) outgoing longwave radiation (OLR, in W/m^2) regressed onto the Arctic precipitation index. The purple box in a) corresponds to the region over which the central Pacific warming (CPW) index is defined. Areas with values significant at the 90% level are hatched.

The SST and OLR regression results suggest a connection between the cool-season Arctic precipitation and the modulation of the El Niño/Southern Oscillation (ENSO) variability on decadal timescales, with the AO likely acting as a dynamical medium. Specifically, an increase (decrease) of the cool-season Arctic precipitation on decadal timescales is associated with more frequent central (eastern) Pacific warming events and weak (strong) ENSO intensity periods according to the ENSO modulation discussed in Sun and Yu 2009. For example, the early 1990s is characterized by above-normal Arctic precipitation, and central Pacific warming events were much more common in this period. According to Yu and Kim 2010, every year during the period 1990-1995 can be identified as a Central Pacific (CP) El Niño. Conversely, during the late 1990s, the Arctic precipitation was below-normal and strong eastern Pacific warming events, such as the 1997/98 El Niño, occurred. The connection between the Arctic precipitation and the central Pacific SSTs is further confirmed by the co-occurrences of the peak values of Arctic precipitation and low values of an index describing the ENSO modulation (Figure 1c of Sun and Yu 2009). In the next step, we examine in detail the potential dynamical mechanisms through which the central Pacific SST anomalies project onto the variability of the AO, which is in turn coupled to the variability in storm track activity and synoptic eddy moisture transport into the Arctic. It is also important to recognize that regression results presented here do not exclude the possibility of cold phase ENSO (i.e., La Niña) contributing to the observed Arctic precipitation variability, however results of the composite analysis shown in section 2.3.4 indicate that La Niña does not play a critical role here.

2.4.1 Direct projection of the tropical central Pacific SST forcing onto AO variability

To illustrate the dynamical implications of central Pacific warming for the extratropical circulation, we define a central Pacific warming (CPW) index as the SSTs averaged over the purple box (10°S-15°N, 165°E-130°W) in Figure 2.3a. The correlation between the smoothed CPW index and the Arctic precipitation index (October-March-mean AO index) is 0.78 (0.61) and significant at the 95% (85%) level. In other words, warm SSTs over the tropical central Pacific are associated with increased total Arctic precipitation and a positive tendency of the AO.

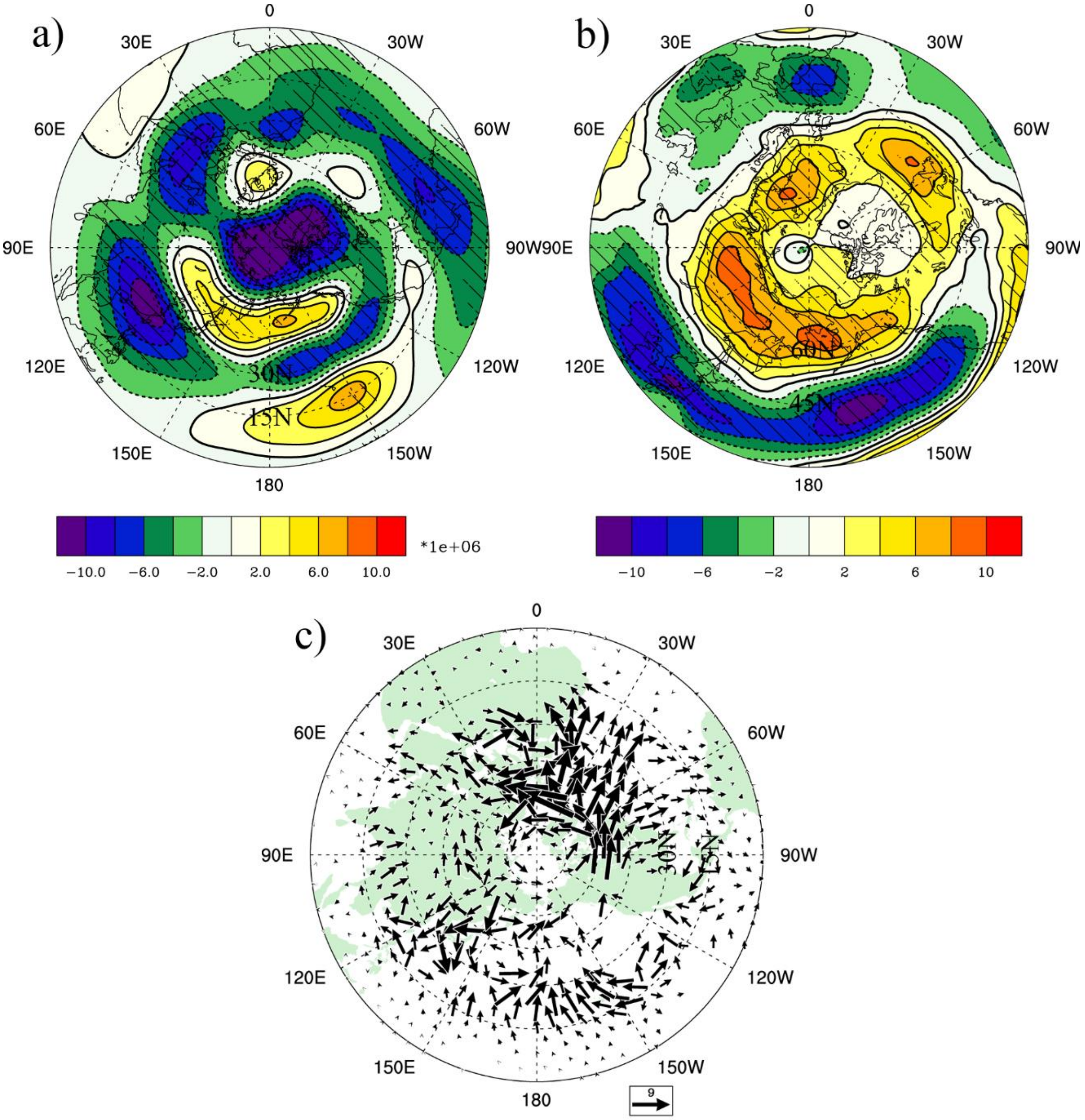

Figure 2.4. a) 250 mb streamfunction (in m^2/s), b) 250 mb zonal wind (in m/s), and c) 250 mb wave activity flux (in m^2/s^2) values regressed onto the CPW index. Areas of values significant at the 90% level are hatched in a) and b) and vectors with either component significant at the 90% level are shown in c).

The coefficients of regression between the 7-year-smoothed 250-mb streamfunction and the CPW index are displayed in Figure 2.4a. A stationary Rossby wave train emanating from the tropical central Pacific is the primary feature of Figure 2.4a. The origin of the wave train is located between 180° and 150°W, consistent with the longitudes where the maximum SST signals are identified (Figure 2.3a). The wave train appears to propagate into the Arctic and project onto a positive AO pattern, i.e., negative streamfunction anomalies over the Arctic. Consistent with the streamfunction anomalies is a poleward shift of the upper tropospheric zonal jets as shown in Figure 2.4b. The regression of the stationary wave activity flux onto the CPW index (Figure 2.4c), however, indicates a horizontal pathway of wave propagation originating from the tropical central Pacific and diminishing around the Aleutian Islands, without reaching the interior region of the Arctic. This suggests that the direct stationary Rossby wave response in the North Pacific is not necessarily the most important mechanism responsible for projecting the tropical Pacific SST forcing onto the AO variability.

2.4.2 Indirect projection of the tropical central Pacific SST forcing onto AO variability

Following the discussion in Section 2.1, the positive AO phase can also be a tropospheric response to a strengthened NH stratospheric polar vortex (e.g. Baldwin and Dunkerton 1999; Black 2002). As a prominent feature of the high latitude atmospheric circulation in boreal winter, the stratospheric polar vortex is characterized by an area of strong zonal-mean westerly winds and low zonal-mean temperatures in the polar stratosphere. Fluctuations in the strength of this vortex appear as anomalies in the zonal mean zonal winds and zonal mean temperature. When regressed onto the CPW index defined in the previous section, the zonal-mean zonal wind field shows positive values, i.e., strengthened westerly winds throughout the stratosphere and troposphere north of 50°N (Figure 2.5a). The increase in zonal wind speed is collocated with the climatological position of the NH winter stratospheric polar vortex, thus representing a strengthening of the vortex. The regression of the zonal-mean temperature onto the CPW index (Figure 2.5b) indicates negative anomalies below the mid-stratosphere north of 60°N, consistent with a poleward shift of the large meridional temperature gradient and the strengthening of zonal-mean zonal winds.

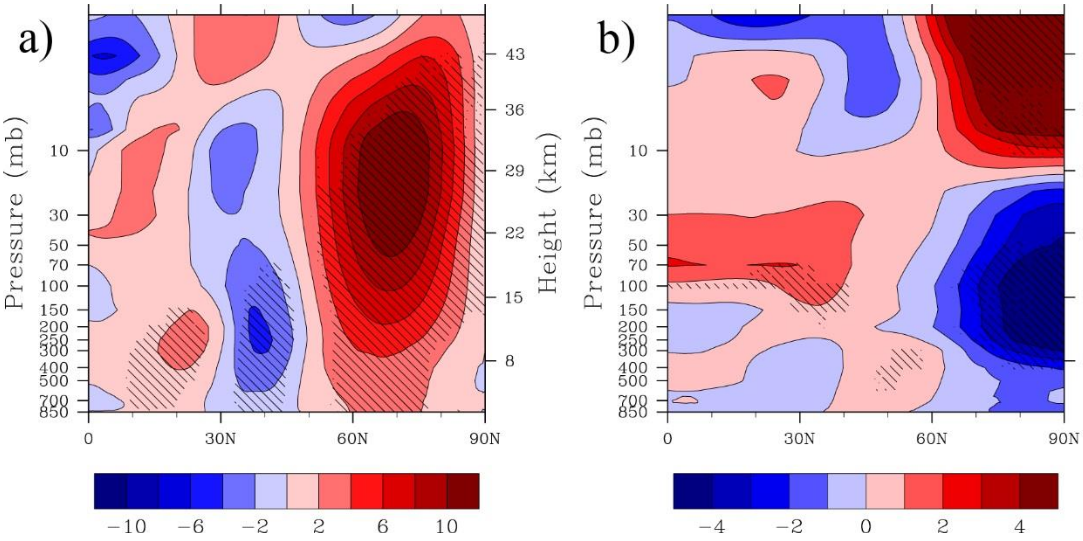

Figure 2.5. a) October-March-averaged zonal-mean zonal wind (in m/s) regressed onto the OM CPW index. b) OM average zonal mean temperature (in K) regressed with the OM CPW index. Areas of values significant at the 90% level are hatched in both figures.

Since an important source of variability in the stratospheric polar vortex is the vertical propagation of Rossby wave energy into the stratosphere (e.g. Polvani and Waugh 2004) we next examine the impact of the tropical central Pacific warming on the upward propagation of tropospheric planetary waves. The vertical propagation of waves is quantified in terms of the EP flux vector described in Section 2. Here we compare the composite EP flux for a 5-year period (1990-1994) of relatively high values of the smoothed CPW index to that of a 5-year period (1997-2001) with relatively low values of the smoothed CPW index. The selection of the compositing periods is independent of the specific smoothed index used (i.e., CPW or Arctic precipitation) due to the high correlation between the two. Figure 2.6a shows the differences in the EP flux vector between the two periods (i.e., 1990-1994 minus 1997-2001), and the vectors have been scaled by a factor of 5 above the 100-mb level following the plotting convention of Garfinkel and Hartmann 2008. Pronounced downward-pointing vectors exist in the lower and middle stratosphere between 50°N and 75°N. Since this region is occupied by upward-pointing EP flux vectors in the cool-season climatology (not shown), the downward-pointing vectors in Figure 2.6a indicates suppressed propagation of tropospheric planetary waves into the stratosphere at the NH high latitudes during periods of elevated tropical central Pacific SSTs (i.e., increased occurrence frequency of central Pacific warming).

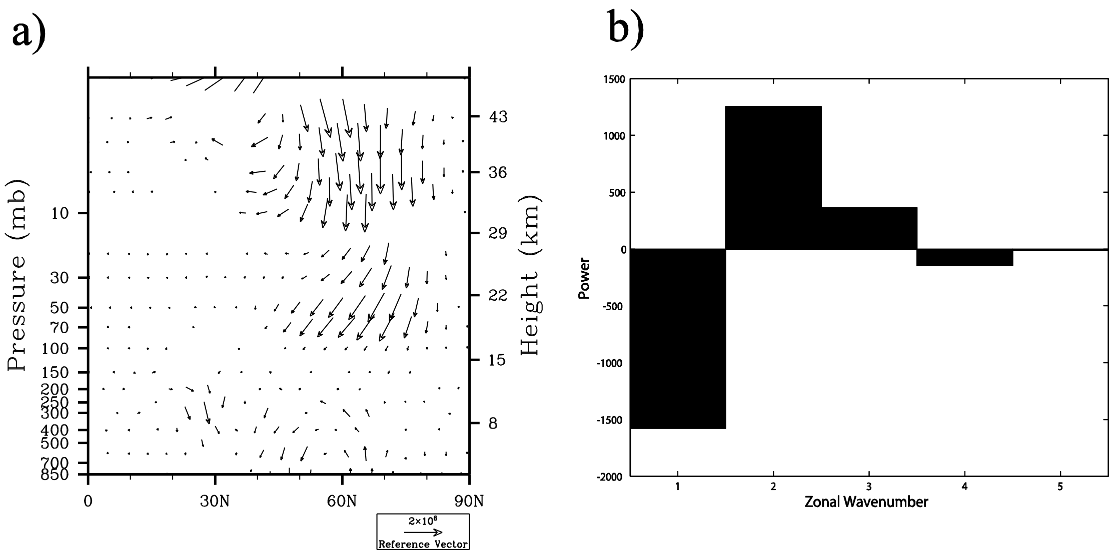

Figure 2.6. a) Difference of the composite EP flux vectors (y-component in (m^2/s^2)*m, z-component in (m^2/s^2)*Pa) between a 5-year period (1990-1994) of above-normal Arctic precipitation and a 5-year period (1997-2001) of below-normal Arctic precipitation. Only vectors with at least one component significant at the 90% level, based on a Welch's t-test, are plotted. b) The composite difference of the power spectrum of the cool-season 500-mb geopotential height (in m, averaged over 45°N-90°N) between the two 5-year periods defined in a), shown as a function of zonal wavenumber.

Zonal wavenumber is a key factor that determines whether vertical propagation of waves is plausible in a westerly environment characteristic of the upper troposphere and lower stratosphere in the NH cool season (Charney and Drazin 1961). Since waves with the largest zonal wavelength and smallest zonal wavenumber (typically 1 and 2) have the best chance of propagating into the stratosphere, we examine further which component of the planetary wave is responsible for the suppressed propagation given in Figure 2.6a. Figure 2.6b shows the differences of the composite power spectrum of the monthly cool-season 500-mb geopotential height north of 45°N between the period 1990-1994 and 1997-2001. What stand out are a significant reduction of the wavenumber-1 amplitude and a moderate increase of the wavenumber-2 amplitude in association with the tropical central Pacific warming. Extraction of the wavenumber-1 and -2 components from the total composite EP flux anomalies (Figure 2.6a) indeed shows suppressed upward propagation of wavenumber-1 waves (Figure 2.7a) and enhanced upward propagation of wavenumber-2 waves (Figure 2.7b). Since the amplitude of decrease of the former is significantly larger than the amplitude of increase of the latter, the net result (sum of the two, Figure 2.7c) is suppressed upward propagation of tropospheric planetary waves and a strengthened stratospheric polar vortex accompanying the tropical central Pacific warming.

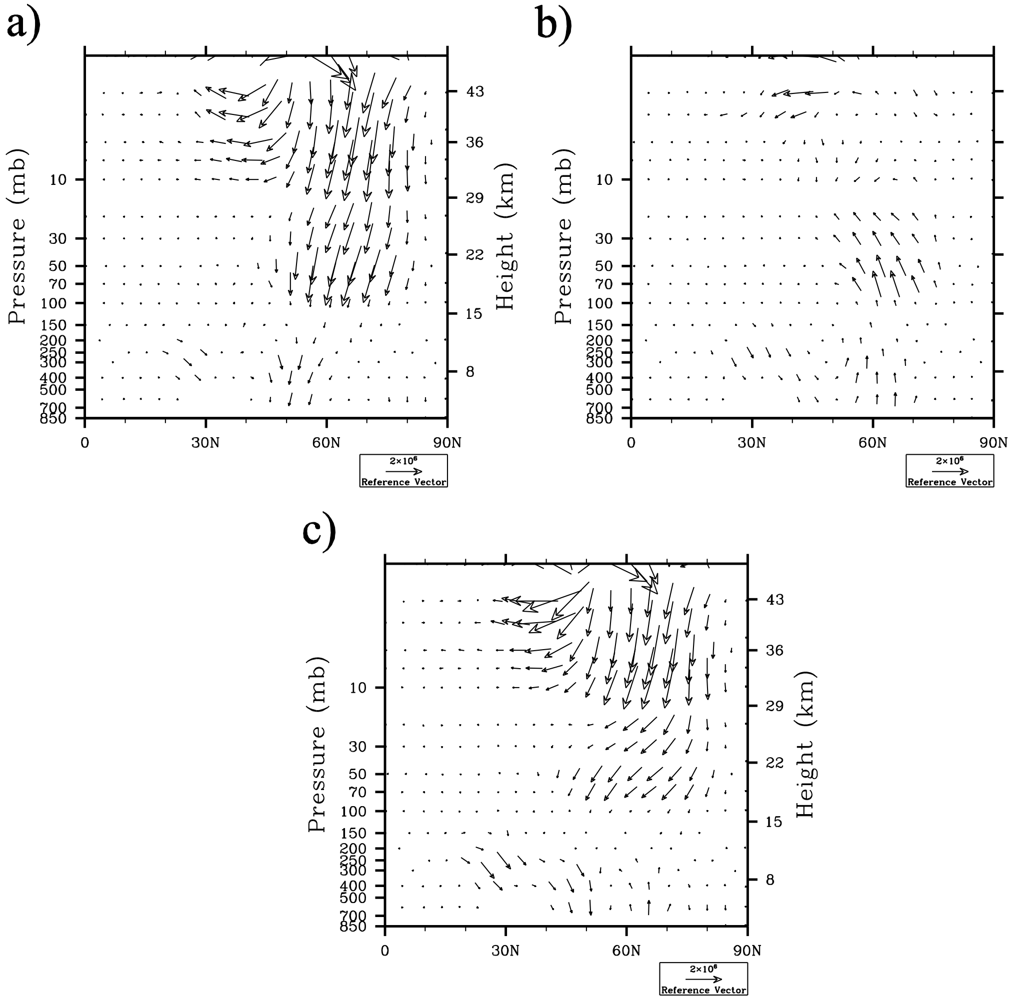

Figure 2.7. Difference of the composite EP flux vectors (same units as in Figure 6a) associated with a) wavenumber-1 and b) wavenumber- 2 component of the planetary wave between the period 1990-1994 and the period 1997-2001. c) is the sum of a) and b). All vectors are plotted.

2.5 Differences in effects of CPW and canonical ENSO warming on the NH stratospheric polar vortex

The effect of CPW on the polar vortex discussed above is the exact opposite of what previous studies (e.g. Taguchi and Hartmann 2006) have suggested for canonical warm ENSO events, where eastern Pacific warming (EPW) results in a weakening of the polar vortex. Given the close link discovered between the Arctic precipitation and the relative occurrence frequency of CPW and EPW events (i.e., the decadal modulation of the ENSO variability), it is necessary to investigate why these two types of warming events leave different dynamical fingerprints in the polar vortex. As noted in Garfinkel and Hartmann 2008, the ability of canonical ENSO to affect the polar vortex ultimately depends on the specific type of extratropical teleconnection excited by the tropical SST anomalies. The deepening of the AL and effective projection onto the PNA pattern proves to be the most effective way of enhancing the wavenumber-1 component of the extratropical planetary wave, increasing its upward propagation into the stratosphere and thus weakening the polar vortex. Here we compare the 500-mb geopotential height anomalies in December-January-February (DJF) associated with classical EPW (Figure 2.8a) and CPW (Figure 2.8b) events. The deepening of the AL is the most pronounced feature in the EPW height composite, while in the CPW composite, a positive anomaly south of Alaska indicates a weakening of the AL.

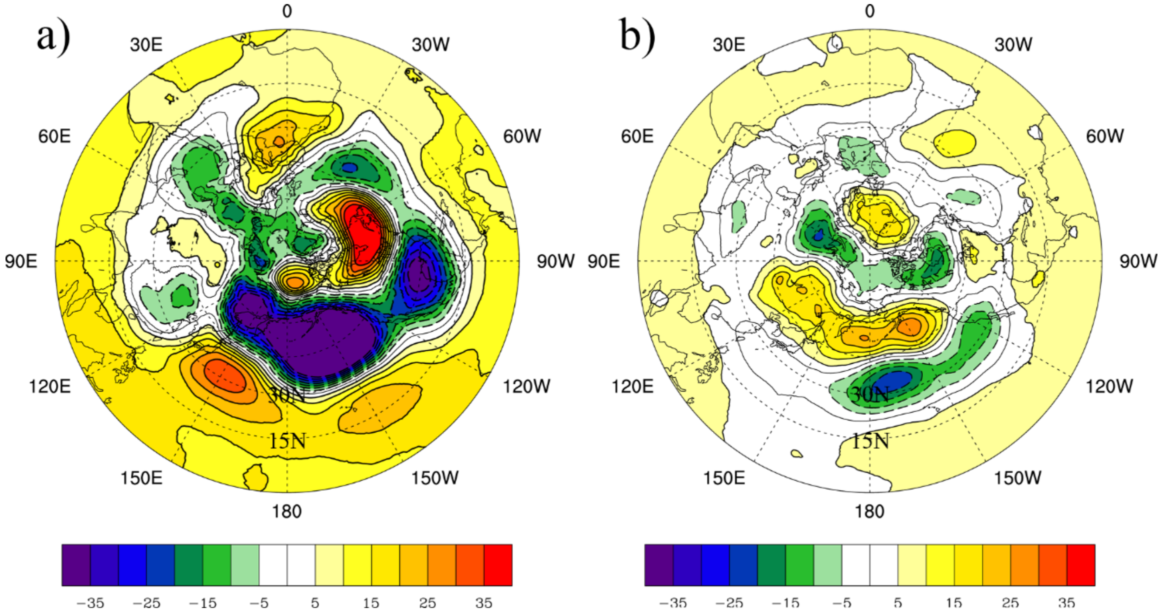

Figure 2.8. Composite anomalies of the DJF 500-mb geopotential height (in m) corresponding to a classic a) eastern Pacific warming (EPW) and b) central Pacific warming (CPW) event. EPW winters used in compositing include 1982/83, 1987/88 and 1997/98. CPW winters include 1990/91, 1994/95, 2002/03 and 2004/05.

The composite anomalies shown in Figure 2.8 are decomposed into their wavenumber-1 and wavenumber-2 components and displayed in Figure 2.9 together with the NH winter climatological planetary waves. It is clear that the deepening of the AL in the EPW case creates wavenumber-1 anomalies (Figure 2.9a) that interfere constructively with the climatological wavenumber-1 pattern (Figure 2.9c) while the CPW generates wavenumber-1 anomalies (Figure 2.9b) that interfere destructively with the climatological wavenumber-1 pattern. This discrepancy is consistent with the opposite effects CPW and EPW exert on the vertical propagation of waves and the resulting changes in the strength of the polar vortex. On the other hand, the wavenumber-2 components of the composite height anomalies (Figure 2.9d and 2.9e) tend to reduce (enhance) the amplitude of the climatological wavenumber-2 waves in the EPW (CPW) case.

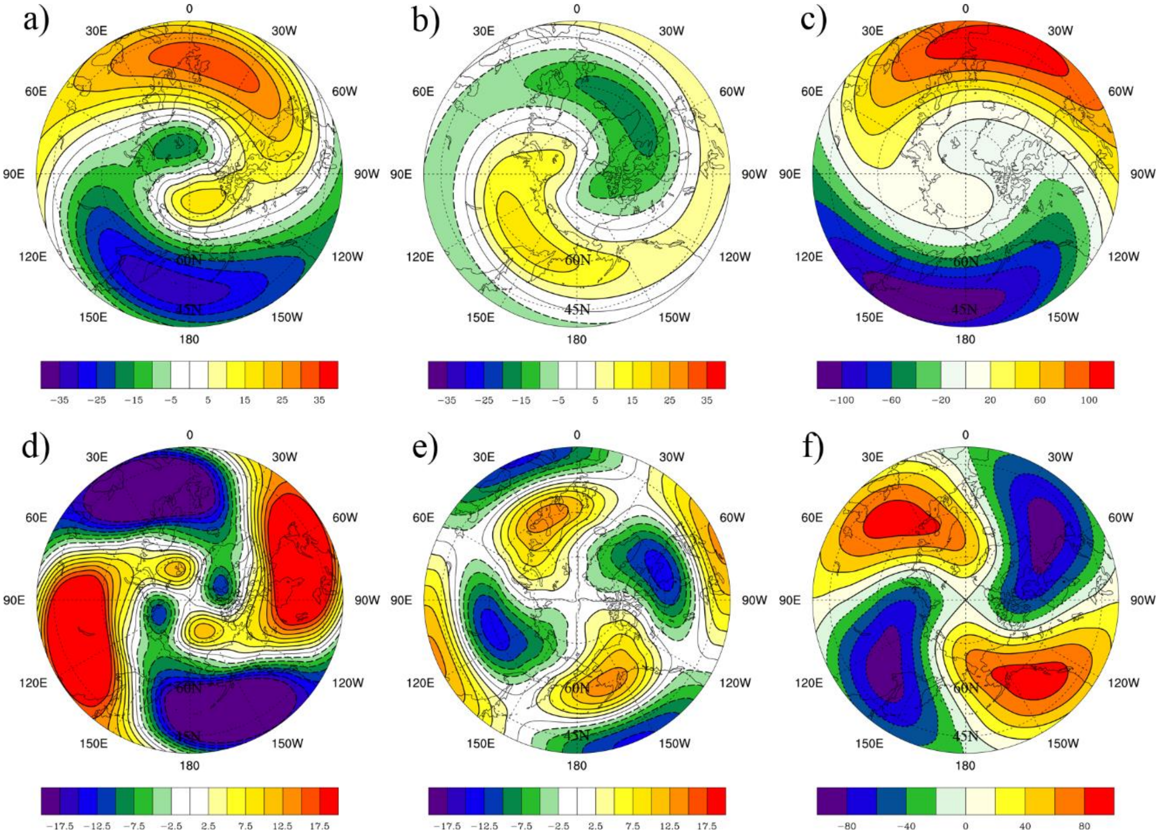

Figure 2.9. Wavenumber-1 (a-c) and wavenumber-2 (d-f) components of the composite anomalies of the DJF 500-mb geopotential height (in m) corresponding to the EPW (a,d) and CPW (b,e) case. The wavenumber-1 and -2 components of the climatological (1979-2009) DJF planetary wave are shown in c) and f), respectively.

Considering a composite of canonical CPW winters, based upon the same set of CPW winters used in deriving the height composite in Figure 2.8b, we display in Figure 2.10 the CPW-winter anomalies with respect to a 30-winter (1979/80-2008/09) climatology in zonal-mean zonal wind, zonal-mean temperature, power spectrum of 500-mb height and EP flux vectors. The results are generally consistent with those in Figures 2.5 and 2.6 and it shows that accompanying the occurrence of a canonical CPW event are increased zonal mean zonal winds north of 50°N (Figure 2.10a), decreased zonal mean temperatures in the stratosphere north of 60°N (Figure 2.10b), an increase (decrease) of wavenumber-1 (2) planetary wave amplitude (Figure 2.10c), and a net decrease in the upward propagation of wave energy into the lower stratosphere (Figure 2.10d). The anomalies shown in Figure 2.10c and 2.10d further confirm the destructive and constructive interference of CPW with the climatological wavenumber-1 and -2 component of the extratropical planetary wave, respectively. The similarity between the canonical CPW winter anomalies and the previously discussed composite differences between two periods indicates that the occurrence of multiple CPWs during the period of 1990-1994 is at least partly responsible for the signals seen in Figures 2.5 and 2.6. The increased occurrence frequency of individual CPW events during one period thus contributes positively to an increase in the Arctic precipitation, through accumulated effects of individual CPWs on the stratospheric polar vortex.

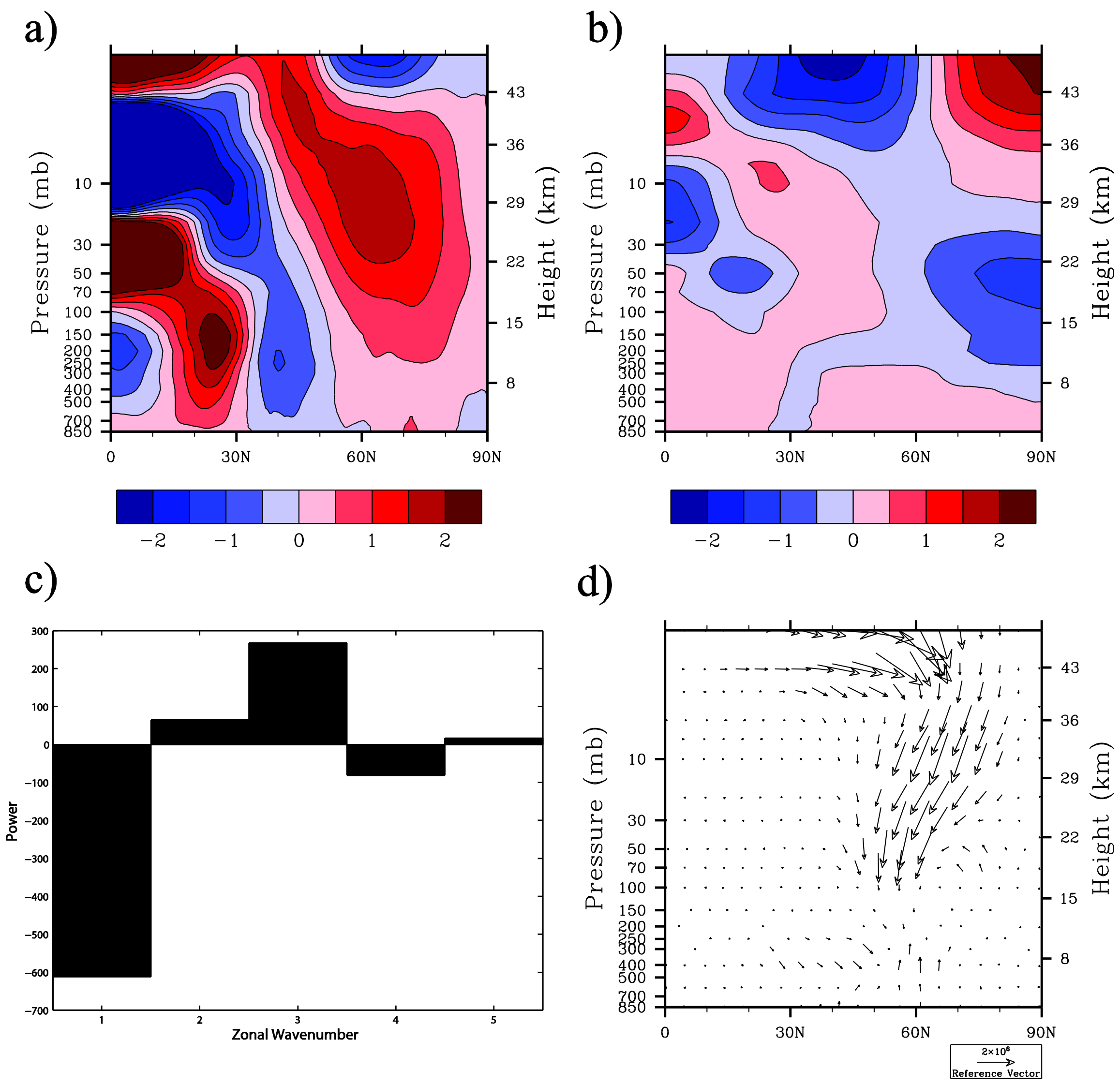

Figure 2.10. Composite anomalies associated with a canonical CPW winter (October-March) in a) zonal-mean zonal winds (in m/s), b) zonal mean temperature (in K), c) the power spectrum of 500-mb geopotential height (in m) and d) the EP flux vector (y-component in (m^2/s^2)*m, z-component in (m^2/s^2)*Pa). The CPW winters used in constructing the composites are the same as those in Figure 8 and 9.

The differences between the impact of the CPW (as discussed in 2.3.4) and EPW (as discussed in previous studies) on the stratospheric polar vortex and AO variability are ultimately a result of the different teleconnection patterns that the CPW and EPW excite in the extratropics. The transition from one period (e.g., 1990-1994), when the CPW events are more common, to another period (e.g., 1997-2001), when the EPW events occur more often, characterizes the decadal-scale modulation of ENSO variability and contributes significantly to the transition from one period of a strengthened polar vortex (positive AO) to another period of a weakened polar vortex (negative AO). With the additional coupling between AO variability and storm track activity, the tropical Pacific SSTs are able to leave distinct dynamical fingerprints in the Arctic precipitation.

2.6 Section Summary and Conclusions

Pronounced decadal-scale variations in the cool-season Arctic precipitation are identified in two observation-based precipitation datasets (GPCP and CMAP) and one high-resolution reanalysis product (MERRA). Despite the discrepancies in the magnitude of their climatological values of Arctic precipitation, all three datasets clearly show above-normal precipitation in the period 1990-1994 and below-normal precipitation in the period 1997-2001. This decadal-scale oscillation, significantly correlated with the decadal-scale variations in the AO, is partly driven by the tropical central Pacific SST changes across decadal timescales. The tropical Pacific SST anomalies tied to the Arctic precipitation variability closely resembles the SST anomalies representative of the decadal modulation of ENSO variability (Sun and Yu 2009), suggesting that the more frequent occurrence of CPW events might have contributed to the increase of Arctic precipitation in the early 1990s and after 2003 (Figure 2.1a).

Dynamically, the diabatic heating induced by the CPW drives a stationary Rossby wave train that extends northward into the North Pacific. The direct projection of the CPW forcing onto the AO variability is limited, given that the wave activity originating from the tropical central Pacific does not reach the interior of the Arctic. However, the SST-forced stationary Rossby wave destructively interferes with the wavenumber-1 component of the extratropical planetary wave, leading to suppressed upward propagation of waves into the polar stratosphere, a strengthened stratospheric polar vortex and a positive tendency in the AO index. The tropical Pacific SSTs thus project indirectly onto the AO variability through modifying the structure of extratropical planetary waves. The effects of CPW and EPW on the polar vortex (AO variability) are exactly opposite, with the wavenumber-1 component of the planetary wave strengthened in an EPW event. The decadal-scale modulation of ENSO variability, characterized by transitions between periods favoring CPW and those favoring EPW, ultimately generates discernable dynamical fingerprints in the decadal-scale AO variability.

The positive AO tendency partly induced by CPW is coupled with a poleward shift of the upper tropospheric zonal wind jets and storm tracks. The elevated synoptic eddy activity north of the Arctic Circle increases the amount of moisture transported into the Arctic by synoptic eddies and contributes directly to the decadal-scale variations in Arctic precipitation. The strongest signal of the storm track response with regard to the Arctic precipitation variability is found over the Atlantic sector of the Arctic, a region characterized by the greatest decadal variations in both precipitation and eddy moisture flux into the Arctic. On decadal timescales, the AO and North Atlantic storm track thus act as a bridge connecting the tropical Pacific SSTs to the strength of the cool-season Arctic hydrological cycle. However, it is recognized by the authors that the direct and indirect (stratospheric) mechanisms discussed here only account for a portion of the decadal-scale variance in the AO and in the Arctic precipitation index, and the length of the observational record, particularly of the precipitation datasets, places a limit on the level of statistical significance we may derive here. Future investigations will focus on 1) testing the hypothesis formulated in this study with controlled general circulation model (GCM) experiments and 2) identifying other dynamical processes contributing to the tropical-Pacific-Arctic connection. Of particular importance for the latter is the need to quantify the synoptic eddy (e.g., vorticity and heat flux) feedback onto the inter-decadal AO variability at the storm track regions. Preliminary analysis of Chemistry-Climate Model Validation Activity (CCMVal, http://www.pa.op.dlr.de/CCMVal/) model output shows that the connection described in this paper is captured in GCM simulations forced with the observed SST field. Details of the model analysis will be reported in the future.

The work presented in this chapter is published in Geophysical Research Letters (Hegyi and Deng 2011).

CHAPTER 3

RESPONSE OF THE WINTER POLAR STRATOSPHERIC VORTEX TO IDEALIZED EQUATORIAL PACIFIC SEA SURFACE TEMPERATURE ANOMALIES IN THE NCAR WACCM

3.1 Motivation and Background

The results in Chapter 2 highlight the difference in response of the polar vortex to CPW and EPW in the cool season, a difference that results in an opposite-signed response in total Arctic precipitation in CPW and EPW years. Because the results are from a representation of observed conditions in previous years in reanalysis, it is difficult to attribute the differences in vortex response purely to CPW and EPW. Other factors not related to CPW and EPW could be driving the difference in vortex response. For example, the subtle differences of the CPW and EPW pattern between individual years may have an important role in the differences in the response of the vortex. Therefore, an idealized model experiment is conducted to isolate and better define the differences in the initial response of the vortex to CPW and EPW. In these model experiments, a fixed pattern of SST anomalies for CPW and EPW is utilized to help remove the variability of vortex responses that are a result of subtle differences in the SST anomaly pattern. Additionally, a suite of model runs with the fixed CPW and EPW patterns are run with varying atmospheric initial conditions (i.e. an ensemble of model runs) to test how the initial response of the vortex is affected by varying the atmospheric initial conditions.

As discussed in the introduction in the description of the cool season Arctic climate, the stratospheric polar vortex is an important element of Arctic and Northern Hemisphere wintertime climate. Changes in the strength of the vortex are driven by the upward propagation and breaking of wave activity from the troposphere, and these changes often project onto tropospheric variability, thus impacting surface climate over high latitudes (Baldwin and Dunkerton 1999; Black 2002) and Europe (Bell et al. 2009; Ineson and Scaife 2009). The El Niño-Southern Oscillation (ENSO) is among several different climate phenomena that affect the strength of the polar vortex through modulating the magnitude of upward wave propagation into the stratosphere. The magnitude of the anomalous upward propagation of wave activity into the stratosphere is especially sensitive to the phase of the forced anomalous Rossby waves in relation to the phase of the climatological planetary wave in the high latitudes of the Northern Hemisphere, i.e. via linear interference (e.g. Fletcher and Kushner 2011; Nishii et al. 2009). When the wave anomaly is *in phase* with the climatological wave (constructive interference), the upward wave propagation from the troposphere to the stratosphere is enhanced. Linear interference has been shown to be an important concept in understanding the interaction among several tropospheric phenomena and the stratosphere, including the interaction between stratospheric variability and blocking highs (Nishii et al. 2011). It also has been shown to be important in describing the link between stratospheric variability and autumnal Eurasian snow cover (Smith et al. 2010). In the case of the interaction between ENSO and the polar stratosphere, the constructive interference of the El-Niño-forced tropospheric geopotential height anomalies (primarily over the North Pacific) with wavenumber 1 and 2 components of the climatological planetary waves leads to a net increase in the upward wave propagation and a weakened polar vortex (Garfinkel and Hartmann 2008; Garfinkel et al. 2010), through the effect of enhanced wave forcing on the stratospheric zonal mean zonal wind.

As a follow-up to the results presented in Chapter 2, we conduct a series of numerical experiments using the National Center for Atmospheric Research (NCAR) WACCM in which idealized SST anomaly patches are superimposed upon a climatological DJF-mean distribution of SSTs. The patches are designed to represent canonical CPW and EPW patterns, respectively, thereby isolating the effects of each type of warming on the polar vortex. The purpose of our model experiments is to document the similarities and differences of the initial transient response (i.e. the response within the first 40 days) of the stratospheric polar vortex to central (CPW) and eastern Pacific warming (EPW) events. We investigate the initial and transient response of the vortex, in contrast to the equilibrium state response that was the main target of previous studies, to facilitating the understanding of the vortex response that in reality also occurs within a short, sub-seasonal time period. Specifically, these idealized experiments allow us to assess the relative significance of the SST forcing patterns versus the initial state of the extratropical circulation in determining the vortex responses across sub-seasonal timescales. Following the introduction, section 3.2 describes the model experiment design and the analysis tools employed. Key results from the model experiments are presented in section 3.3 while concluding remarks are given in section 3.4.

3.2 Data and Methods

3.2.1 Model Experiment Setup

We employ the NCAR Whole Atmosphere Community Climate Model Version 4 (WACCM4) in this study (Garcia et al. 2007). WACCM4 is run as a component set within the NCAR Community Earth System Model Version 1.0.2 (CESM 1.0.2). The WACCM model is specifically designed to investigate the coupling between the stratosphere and the troposphere and is thus appropriate for experiments exploring the effects of tropical SSTs on the stratosphere. Versions of the WACCM model have been used in several previous studies of stratosphere-troposphere interaction (e.g. Calvo and Marsh 2011; Sassi et al. 2004; Taguchi 2010). Importantly, with 66 vertical levels and a model top at approximately 150 km, WACCM4 has a well-resolved stratosphere. It also includes an option to impose a realistic Quasi-Biennial Oscillation (QBO) on each model run. In our set of WACCM runs, perpetual January 1st conditions are selected in order to eliminate the impact of solar forcing and remove the seasonal cycle from each experiment. The imposed QBO was turned off, resulting in weak stratospheric easterly winds in the QBO region.

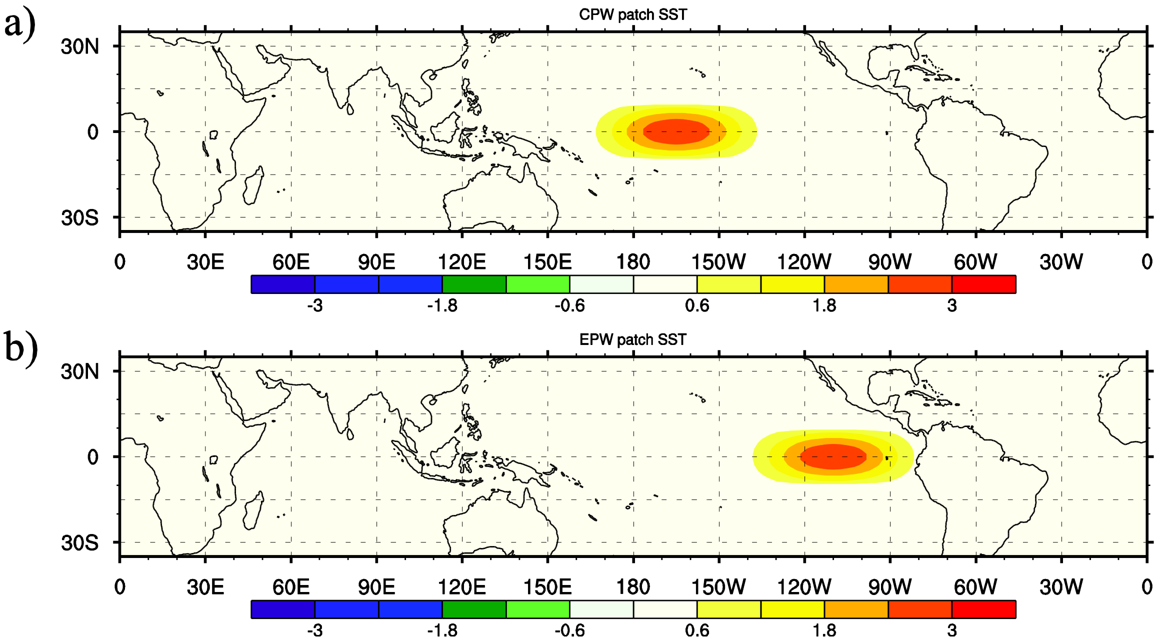

Figure 3.1. Patches of idealized positive SST anomaly used to represent the tropical central Pacific warming (a) and tropical eastern Pacific warming (b). Outside of the patch area, anomalies are identically zero.

A control run with climatological SSTs was performed first. The control run consists of a 1000-day simulation forced by 1870-2009 DJF-average SSTs taken from the Hadley Center Sea Ice and Sea Surface Temperature (HadISST) dataset (Rayner et al. 2003). The control run was used to (i) provide a source of initial conditions and (ii) serve as a basis for comparisons with the two ensembles of CPW and EPW patch runs. In the second step, two 20-member ensembles of 90-day simulations forced by idealized tropical SST anomaly patterns were conducted. To create the prescribed SSTs for each set of forced runs, the idealized SST anomaly "patches" (Figures 3.1a and 3.1b) were added to the DJF-average climatological SSTs used in the control run (thus these ensemble members are referred to as the "patch" runs). In the first ensemble, the patch is applied in the central Pacific mimicking the canonical pattern of CPW. In the second ensemble, the patch is applied in the eastern Pacific to represent EPW events. Each ensemble member is initialized using unique initial conditions drawn from the control run. The initial conditions were chosen to cover a variety of the strength of the stratospheric polar vortex that is typically measured by the zonal mean zonal wind at 10 hPa and 60°N. All the ensemble members have values of this intensity index in the initial conditions ranging between 22.5 and 27.5 m/s, which are average November values of this index in reanalysis data. The effects of the patches are assessed by comparing the patch run results with the corresponding 90-day period in the control run (the first day of this period is identical to the day from which the initial condition of the patch run is drawn). As a consequence, the control state used for comparison is different for each ensemble member with different initial conditions. The same 20 initial conditions were used for the CPW and EPW ensemble, allowing also for direct comparisons across the two ensemble groups. Statistical significance of the ensemble average anomalies relative to the control run was calculated through a two-tailed Student’s t-test.

The SST patches used in the patch ensembles were created using a cosine-squared function identical to the function used in Barsugli and Sardeshmukh (2002) .

$$T_k(\lambda,\varphi) = B\cos^2(\tfrac{\pi}{2}\tfrac{\varphi-\varphi_k}{\varphi_w})\cos^2(\tfrac{\pi}{2}\tfrac{\lambda-\lambda_k}{\lambda_w}) \qquad (3.1)$$

The SST patch equation is a function of latitude (ϕ) and longitude (λ). The subsets *k* and *w* represent the center point of the patch and the width parameter of the patch, respectively. The parameter *B* represents the maximum amplitude of the patch. The CPW (EPW) patch was centered at 165°W and 0°N (110°W and 0°N). Each patch is an ellipse with a minor axis of 20 degrees in length in the north-south direction and a major axis of 60 degrees in length in the east-west direction, and a maximum amplitude of B=3.0 K. The latitude and longitude width parameters were set to 40 degrees and 27 degrees, respectively, for each patch, to create a more gradual decrease of the SST anomaly values when moving away from the center of the patch. Outside of the patch areas, the SST anomalies are equal to the climatological SSTs used in the control run. With these parameters, the average SST anomaly over each patch is 1.383 K. The bounds of the EPW patch are designed to cover most of the Nino 3 and Nino 1+2 regions and to extend eastward to the South American coast. The bounds of the CPW patch are very similar to the central Pacific anomaly box used in the definition of the Modoki index in Ashok et al. (2007) , with the only difference being that the CPW patch is extended 5 degrees eastward to match the size of the EPW patch.

3.2.2 Analysis Method

The basis for our analysis of the model results is the quasi-geostrophic (QG), zonal mean zonal momentum equation (e.g., Holton 2004, Andrews et al. 1987):

$$\frac{\partial \bar{u}}{\partial t} = f_0 \bar{v} - \frac{\partial \overline{(u'v')}}{\partial y} + \bar{X} \qquad (3.2)$$

where overbars represent the zonal average and primes represent the deviation from the zonal average. According to Equation 3.2, the net tendency of the zonal mean zonal wind ($\frac{\partial \bar{u}}{\partial t}$) is equal to the sum of the convergence of the eddy momentum flux ($-\frac{\partial \overline{(u'v')}}{\partial y}$), the Coriolis force exerted on zonal mean meridional wind ($f_0 \bar{v}$), and the drag term ($\bar{X}$). The zonal mean meridional wind ($\bar{v}$) and the vertical velocity ($\bar{w}$) are tied together through the continuity equation. Thus, these terms represent the mean meridional circulation (MMC), and we may call the Coriolis force term in Equation 3.2 the contribution to the zonal mean zonal wind tendency by the eddy-driven mean meridional circulation. In the results section, we thus focus our discussion on the roles of the two components of the eddy forcing - the eddy MMC forcing and eddy momentum forcing, in generating the simulated response of the vortex to the specified CPW and EPW events. Specifically, we investigate the contributions of anomalies in these two eddy forcing terms to the changes in the evolution of the stratospheric polar vortex during the first 40 days after the CPW or EPW heating is switched on.

Additionally, we also make an attempt to compare the relative importance of the initial atmospheric state, internal variability, and the CPW/EPW-forced variability in determining the transient response of the vortex. To do that, we first define the following nomenclature – variable (X) from any model run is labeled as $X_{CTL,\tau}\ or\ X_{PCH,\tau}$, where CTL denotes the control run, PCH denotes the patch run and τ indicates the time after the patch is introduced. The initial condition is thus X_0. Given the design of the model experiment, this value is identical for a control run and the corresponding EPW and CPW patch run. Following these definitions, any variable in the patch run can be written as the following:

$$X_{PCH,\tau} = X_0 + (X_{PCH,\tau} - X_{CTL,\tau}) + (X_{CTL,\tau} - X_0) = IC + FV + IV \tag{3.3a}$$

where X_0 , the initial condition, is denoted as IC; the difference between the patch run and control run (the term inside the first bracket) is referred to as forced variability (FV); and the difference between the variable value at τ and the initial value in the control experiment (the term inside the third bracket) is considered the internal variability (IV) of the system. Similarly, any variable in the control run can be written as the following:

$$X_{CTL,\tau} = X_0 + (X_{CTL,\tau} - X_0) = IC + IV \tag{3.3b}$$

Following Equations 3.3a and 3.3b, we decompose the eddy zonal and meridional wind in the eddy momentum flux term $\overline{(u'v')}$. Taking the difference of this quantity between the patch and the corresponding control run yields:

$$UV = \overline{u'v'}\Big|_{PCH,\tau} - \overline{u'v'}\Big|_{CTL,\tau} = \overline{FV_u FV_v + FV_u(IV_v + IC_v) + FV_v(IV_u + IC_u)} \tag{3.4}$$

The subscripts here represent the variable used to calculate each term, with the primes omitted in the notation (e.g. $FV_u = u'_{PCH,\tau} - u'_{CTL,\tau}$). In our discussion, we consider the first term on the right hand side (RHS) of Equation 3.4 the nonlinear heating component since it is purely a product of forced variability (FV) terms associated with the imposed

CPW or EPW forcing. The second and third term on the RHS of Equation 3.4 are considered linear components as they are both products of forced variability (FV) and internal variability (IV) or initial condition (IC). The relative importance of the nonlinear and linear components in generating the CPW/EPW-forced vortex response will be discussed for the eddy momentum forcing.

Finally, to explicitly diagnose the transient difference of the stratospheric zonal mean zonal wind between the patch run and the control run, we integrate Equation 3.2 from time 0 to time τ, neglect the drag term $\bar{X}$, and take the difference of the integrated equation between the patch and control run to obtain the final diagnostic equation:

$$\int_{\varphi_1}^{\varphi_2} (\bar{u}_{PCH,\tau} - \bar{u}_{CTL,\tau}) d\varphi = f_0 \int_0^{\tau} \int_{\varphi_1}^{\varphi_2} (\bar{v}_{PCH,\tau} - \bar{v}_{CTL,\tau}) d\varphi dt - \left(\frac{1}{a}\right) \int_0^{\tau} (UV\big|_{\varphi_2} - UV\big|_{\varphi_1}) dt \tag{3.5}$$

In Equation 3.5, the left hand side (LFT) corresponds to the difference of the vortex strength between the patch run and the control run at any time τ, where the vortex strength is obtained by averaging the zonal mean zonal wind between two latitudes φ_1 and φ_2 (taken to be 50°N and 80°N in our calculation). Equation 3.5 simply states that the instantaneous difference in the vortex strength between the patch and the control run can be attributed to two components of the eddy forcing: the eddy-driven MMC forcing (the first term on the RHS of Equation 3.5) and the eddy momentum forcing (the last term on the RHS of Equation 3.5), where the eddy momentum forcing can be further decomposed into nonlinear and linear components according to Equation 3.4.

3.3 Ensemble-Averaged Response to CPW and EPW

The ensemble average of the EPW and CPW patch runs shows evidence of a weakened vortex in response to both CPW and EPW forcing (Figure 3.2). What is plotted in Figure 3.2 are the differences of the zonal mean zonal wind between the patch run and the corresponding control run averaged over 50°N-80°N as a function of pressure and time (in terms of the number of days since the CPW/EPW heating is switched on). The 50°N-80°N latitudinal range corresponds to where the winter stratospheric polar vortex resides in the Northern Hemisphere. There are negative anomalies present starting from day 22 in both the CPW and EPW case. The anomalies extend throughout the stratosphere in both cases, but extend lower into the upper troposphere in the CPW case than in the EPW case. The anomalies peak in intensity around day 35 in the CPW case, and day 37 in the EPW case. Despite these minor differences, the vortex weakens with a similar magnitude and timing when CPW or EPW forcing is imposed. The 10 mb zonal mean zonal winds decrease 8.8449 (10.0793) m/s in the CPW (EPW) ensemble average during the peak of the initial response. In addition, the ensemble spread is 10.9558 (12.5669) m/s in the CPW (EPW) ensemble average, as measured by the inter-member standard deviation.

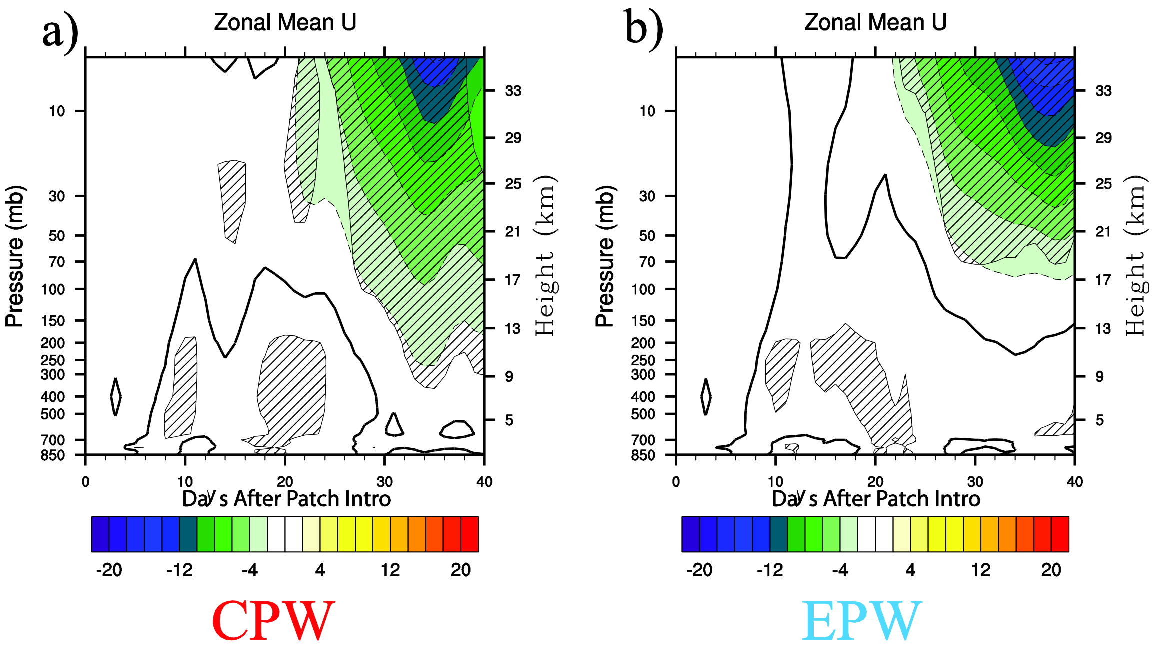

Figure 3.2. Ensemble average of daily 50-80°N average zonal mean zonal wind anomalies in the a) CPW and b) EPW patch runs. Anomalies are calculated relative to the zonal mean zonal wind value in the corresponding control run. Positive (negative) values are denoted by solid (dashed) contours, and the zero contour is bolded. 95% significance of the anomalies in the ensemble average in each panel is hatched.

Figure 3.3 shows the corresponding ensemble averages of the anomalies in the eddy-driven MMC and eddy momentum flux forcing. For the CPW case (upper panels), consistent with the initial vortex weakening starting from day 22, a large negative eddy-driven MMC anomaly emerges in the middle and upper stratosphere (Figure 3.3a). A weaker negative anomaly of the eddy momentum forcing also appears in the stratosphere a couple of days earlier, relative to the negative MMC forcing anomaly (Figure 3.3b). Thus both components of the eddy forcing act to weaken the vortex in the CPW case with the eddy-driven MMC forcing being greater in magnitude when compared to the eddy momentum forcing. In the EPW case, the negative anomaly of the eddy-driven MMC forcing occurs at a much later time (around day 30) (Figure 3.3c). The negative anomaly of the eddy momentum forcing therefore plays a more important role in the initial weakening of the vortex in EPW (Figure 3.3d), while the negative eddy-driven MMC forcing anomaly dominates during the peak of the vortex weakening. The slight timing differences in the occurrences of the eddy forcing anomalies may explain the slight differences in timing of the vortex weakening between the CPW and EPW case. In the ensemble average, although both the eddy momentum and eddy-driven MMC forcing contribute to the initial and transient weakening of the vortex, the eddy-driven MMC forcing has a larger magnitude and clearly dominates the process.

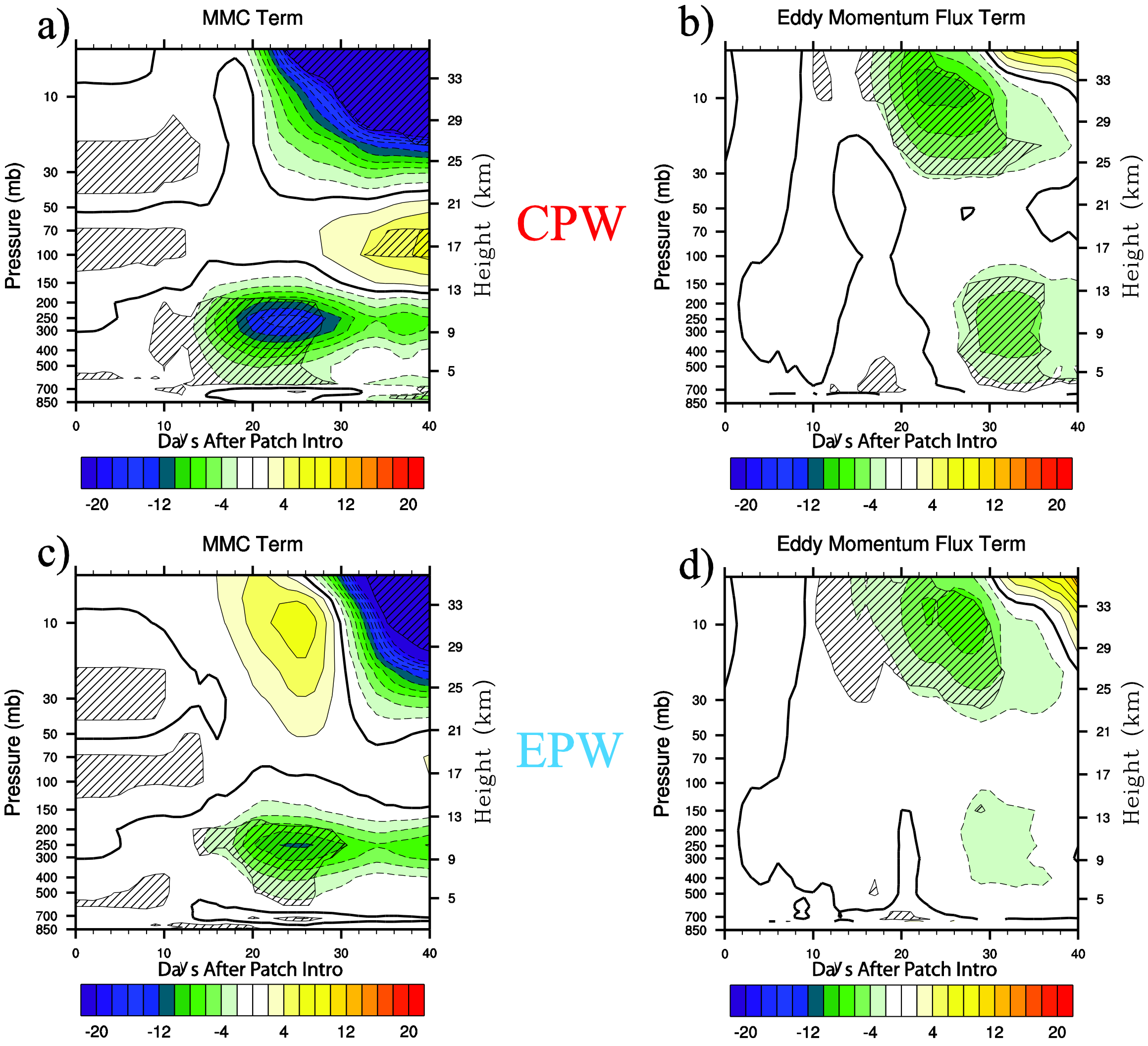

Figure 3.3. Ensemble average of daily 50-80°N average contribution of the eddy-driven mean meridional circulation (MMC) and eddy momentum flux anomalies to anomalies in the zonal mean zonal wind in the CPW [a) and b), respectively] and EPW patch runs [c) and d), respectively]. Positive (negative) values are denoted by solid (dashed) contours, and the zero contour is bolded. 95% significance of the anomalies in the ensemble average in each panel is hatched.

Interestingly, as shown in Figure 3.4, if the eddy momentum forcing is further broken down into the nonlinear and linear parts as defined in Section 3.2.2 following Equation 3.4, the linear part shows a negative contribution to the zonal mean zonal wind tendency. This is consistent with the overall influence of the eddy momentum forcing on the vortex strength (Figures 3.4b and 3.4d). The nonlinear part actually has a positive contribution that tends to strengthen the vortex (Figures 3.4a and 3.4c). The nonlinear part is slightly weaker in magnitude compared to the linear part and this is the main reason why the overall eddy momentum forcing is weakly negative. For both the CPW and EPW cases, it is clear that the linear part of the eddy forcing, which represents the interactions between the CPW/EPW-forced variability and the initial condition/internal variability of the extratropical atmosphere, contributes to a significant weakening of the vortex.

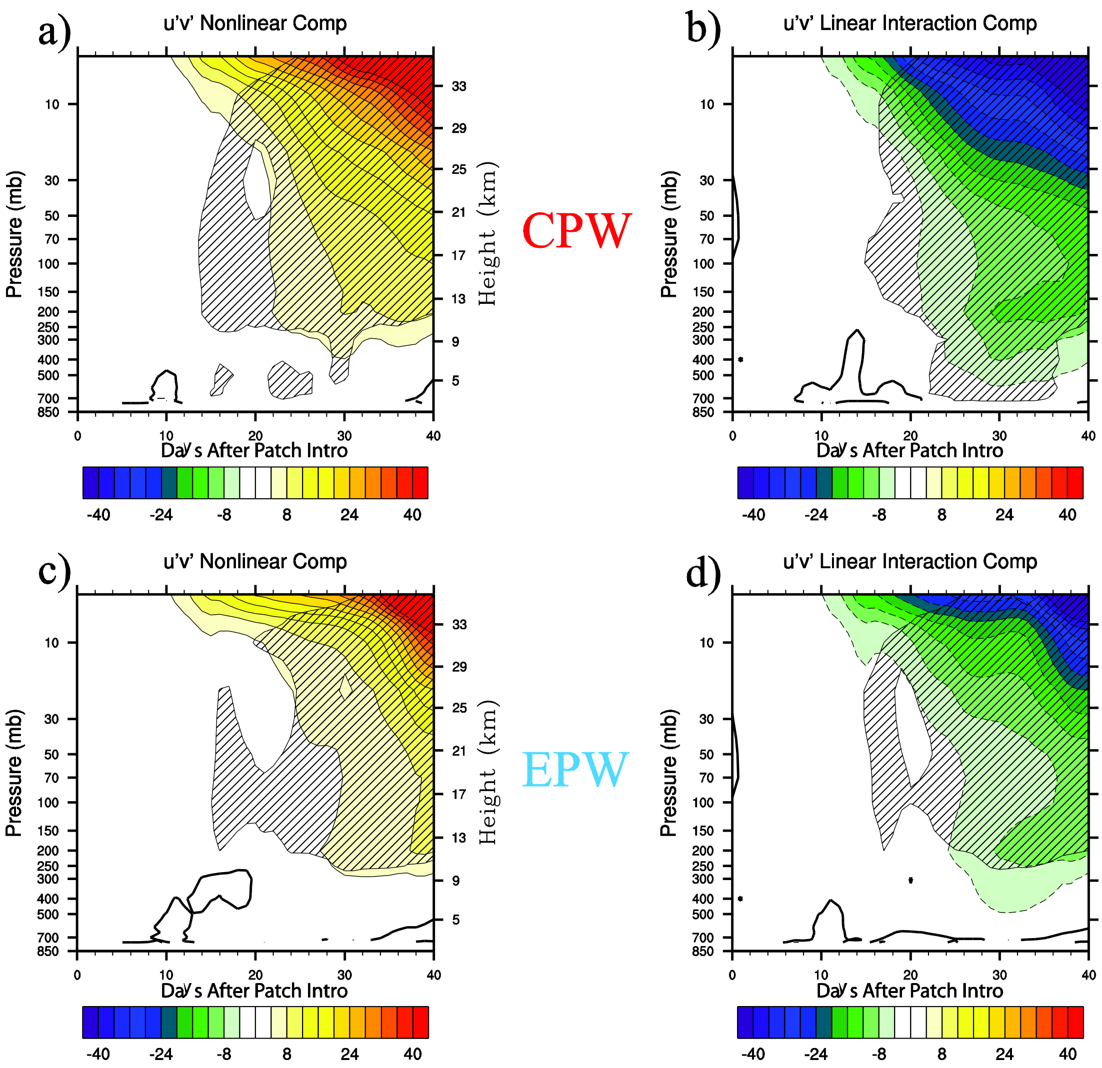

Figure 3.4. Ensemble average of daily 50-80°N average contribution of the nonlinear and linear components of the eddy momentum flux to the total eddy momentum flux anomalies (Figures. 3b and 3d) in the CPW [a) and b), respectively] and EPW patch runs [c) and d), respectively]. Positive (negative) values are denoted by solid (dashed) contours, and the zero contour is bolded. 95% significance of the anomalies in the ensemble average in each panel is hatched.

Figure 3.5 shows the ensemble averaged anomalies of the two components of the linear part of the eddy momentum forcing, namely, FV-IC (interaction between SST-forced variability and the initial atmospheric condition) and FV-IV (interaction between SST-forced variability and the internal variability of the atmosphere). FV-IC results in a positive anomaly in the stratosphere starting from day 14 and extending to day 25 (Figures 3.5a and 3.5c). The positive anomaly is slightly stronger initially in response to CPW than in response to EPW. FV-IV, on the other hand, produces negative anomalies in both the CPW and EPW cases (Figures 3.5b and 3.5d). These anomalies appear at a similar time as the FV-IC anomalies, but have a much larger magnitude and are consistently negative, ultimately making the total linear part of the eddy momentum forcing negative. This result, together with the overall significance of the linear component of the eddy momentum forcing as demonstrated in Figure 3.4, lends support, from a transient response perspective, to the linear interference mechanism proposed by earlier studies in an attempt to explain the connection between the tropical Pacific warm SST events and the weakening of the stratospheric polar vortex. It suggests that the interaction between the extratropical wave response to the tropical Pacific warming and the initial state/internal variability of the extratropical atmosphere largely determines the tendency of the zonal mean zonal winds in the polar stratosphere, and thus the anomalous transient evolution of the stratospheric polar vortex.

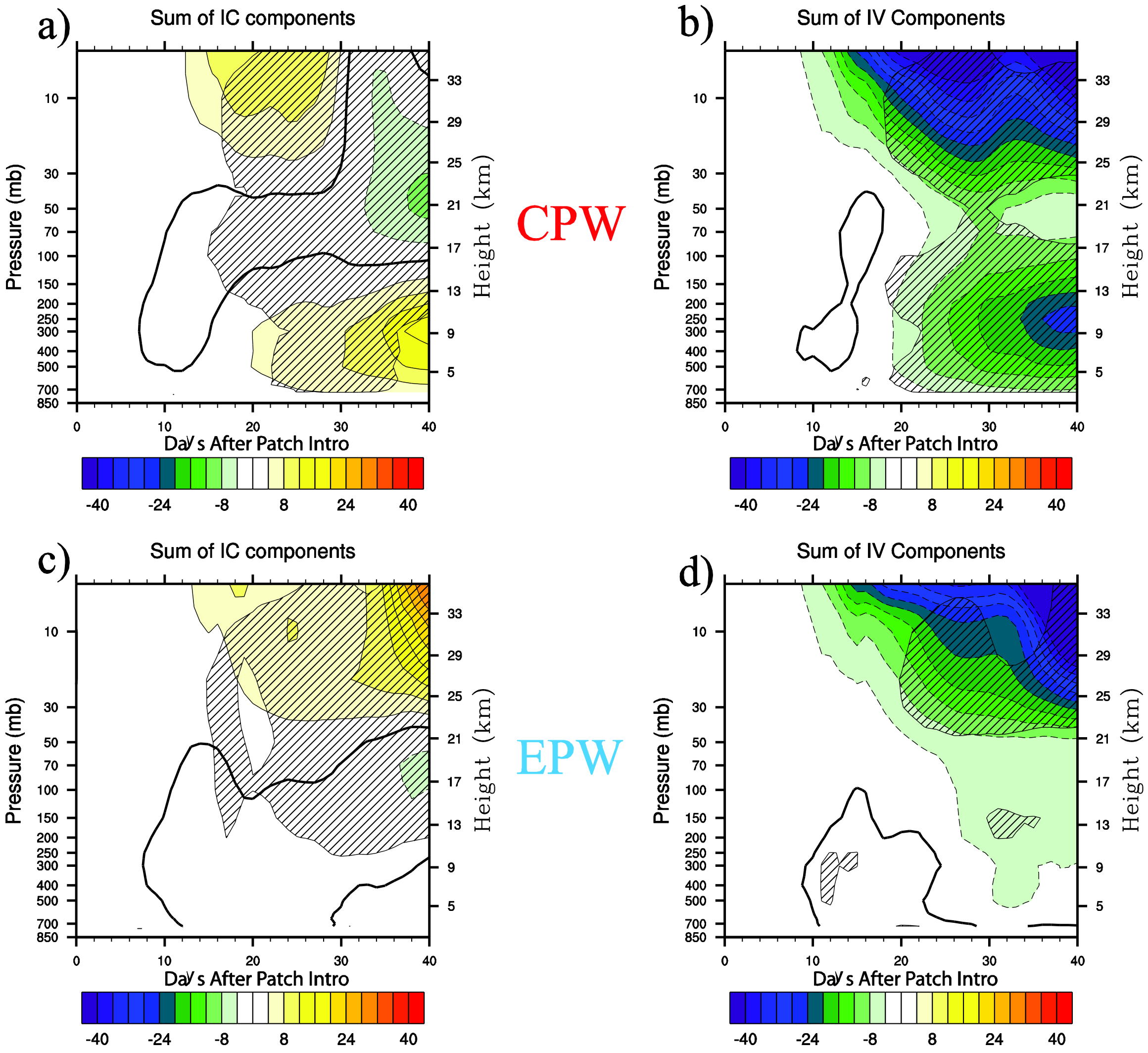

Figure 3.5. Ensemble average of daily 50-80°N average contribution of the initial condition and internal variability parts to the linear component of the eddy momentum flux term (Figures 4b and 4d) in the CPW [a) and b), respectively] and EPW patch runs [c) and d), respectively]. The initial condition (internal variability) part represents the interaction between the forced variability and the initial condition (internal variability). Positive (negative) values are denoted by solid (dashed) contours, and the zero contour is bolded. 95% significance of the anomalies in the ensemble average in each panel is hatched.

3.3.1 Diversity of Vortex Responses to CPW and EPW in Individual Ensemble Members

Despite the consistency in the ensemble average, there is much variability in the initial, transient vortex response to CPW and EPW forcing in the individual ensemble members. This diverse response is a reflection of the importance of the initial atmospheric state and the subsequent internal variation of the extratropical atmosphere in determining the overall response of the vortex to a tropical SST anomaly. For example, although the vortex initially weakens in response to CPW and EPW in most individual ensemble members (marked by blue squares and asterisks in Figure 3.6), the vortex initially strengthens in response to CPW or EPW in a few of the individual ensemble members (marked by red squares and asterisks in Figure 3.6). This is consistent with the distribution of vortex responses in Garfinkel et al. 2012, where a few of the ensemble members show a strengthened vortex in response to CPW and EPW. The vortex initially strengthens in response to both CPW and EPW in case 4, and the vortex initially weakens in response to CPW and strengthens in response to EPW in case 20. We also document the longitudinal position of the zonal wavenumber 1 and 2 wave in Figure 3.6. These planetary waves are most likely to propagate up from the troposphere to the stratosphere and affect the strength of the polar vortex. In these cases, the longitudes where peak values of the initial wavenumber 1 and 2 components of the tropospheric planetary waves are found to deviate significantly from the corresponding ensemble averaged values (denoted by the black asterisk in Figure 3.6). Specifically, the cases where the vortex response is not consistently weakening tend to have a wavenumber 1 wave in the initial state whose peak value is found at a longitude far away from the longitude of approximately 165°E in the ensemble average. Given the importance of the linear part of the eddy momentum forcing in determining the vortex response, it is plausible that the observed diverse vortex response arises from the differences in the way how the CPW/EPW-forced waves interact with the initial and the subsequent internal variation of the extratropical planetary waves. We therefore conduct a more detailed investigation of two anomalous cases, namely case 4 and case 20.

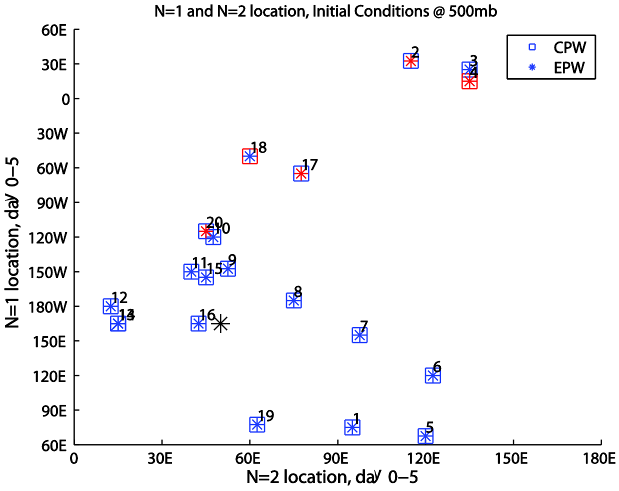

Figure 3.6. Day 0-5 average position of maximum positive value of zonal wavenumber 1 and 2 in the 500 hPa geopotential height field, averaged over the latitude range 50-80°N. The sign of the day 20-30 averaged vortex response, as measured with the 60°N, 10 hPa zonal mean zonal wind is shown with the color shading of each scatter point (red=increased zonal mean zonal winds/strengthened vortex, blue=decreased zonal mean zonal winds/weakened vortex). The CPW (EPW) response is shown by the square (asterisk) at each scatter point, and the average position and magnitude in the 1000-day model climatology is marked by a black asterisk. Each point is numbered for reference within the text.

In case 4, the vortex initially strengthens slightly starting from about day 22 in response to both CPW and EPW (Figures 3.7a and 3.8a). The strengthening is quite brief in the sense that it lasts only approximately 3 to 4 days and weaker in magnitude than the initial strengthening in the ensemble CPW and EPW response. In this case, the initial strengthening response (day 22-26 zonal mean zonal wind anomaly at 10 mb) has a magnitude of 3.6787 m/s and 4.4224 m/s to CPW and EPW, respectively. The magnitude of these strengthening responses is about 40% of the ensemble average response, and within 1.15 standard deviations from the mean, based on the ensemble spread. The strengthening is largely related to a positive anomaly of the eddy-driven MMC forcing in the stratosphere (Figures 3.7b and 3.8b). Following the initial strengthening, the vortex weakens starting from about day 28, as a pronounced negative anomaly of the eddy momentum forcing emerges (Figures 3.7c and 3.8c). In the EPW case, the eddy-driven MMC forcing also switches to a strong negative anomaly around day 34, contributing to the subsequent weakening of the vortex (Figure 3.8b). Just like in the ensemble average, the interactions between the CPW/EPW-forced variability and the initial state and internal variability of the extratropical atmosphere, i.e., the linear part of the forcing (Figures 3.7e and 3.8e) largely contribute to the negative anomaly of the eddy momentum forcing. The nonlinear part of the forcing due to CPW/EPW-forced variability alone tends to be positive and leads to strengthening of the vortex (Figures 3.7d and 3.8d). Thus the main difference between case 4 and the ensemble average is that in case 4 the initial positive anomaly of the eddy-driven MMC forcing lasts much longer, particularly under CPW forcing (Figure 3.7b).

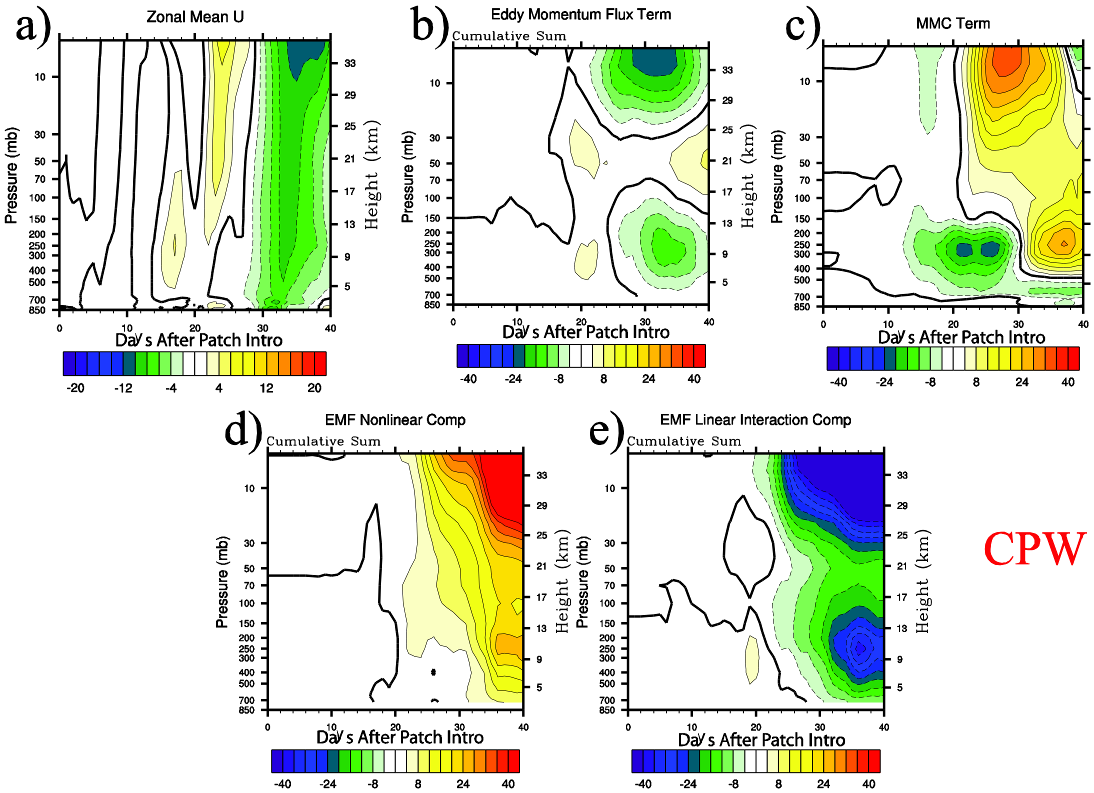

Figure 3.7. a) Daily 50-80°N average zonal mean zonal wind anomalies in the CPW patch run for case 4 in Figure 6. 50-80°N average contributions of the eddy momentum flux and eddy-driven mean meridional circulation (MMC) anomalies to the zonal mean zonal wind anomalies in this case are shown in b) and c), respectively. The 50-80°N average nonlinear and linear parts of the eddy momentum flux are shown in d) and e), respectively. Positive (negative) values are denoted by solid (dashed) contours, and the zero contour is bolded. 95% significance of the anomalies in the ensemble average in each panel is hatched.

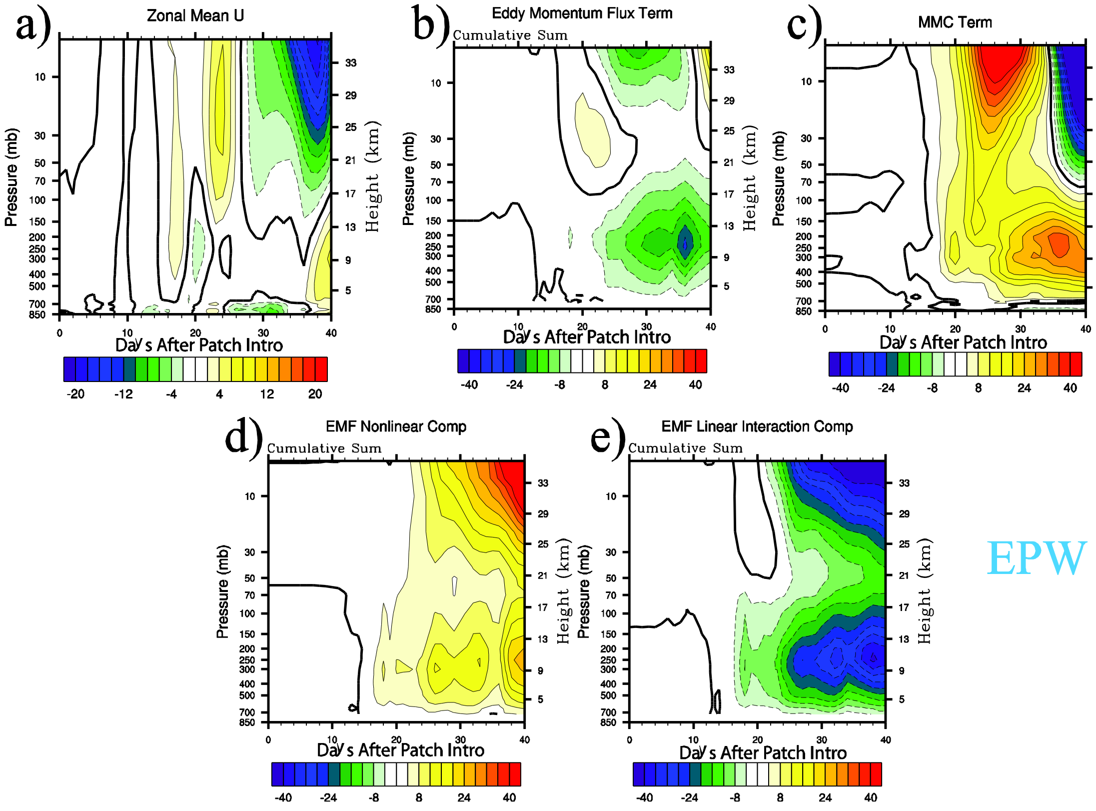

Figure 3.8. Same as Figure 3.7, except for the EPW patch run in case 4.

In case 20, the vortex initially strengthens slightly at about day 20 in response to EPW and CPW (Figures 3.9a and 3.10a). However, the initial strengthening in the CPW case is much weaker than that in the EPW case. The initial strengthening response (day 18-24) zonal mean zonal wind anomaly at 10 mb) has a magnitude of 2.7413 m/s and 10.1181 m/s to CPW and EPW, respectively. The magnitude of these strengthening responses is about 30% (100%) of the CPW (EPW) ensemble average response, and within 1.06 (1.61) standard deviations from the CPW (EPW) mean, based on the ensemble spread. Since we define the sign of the transient response in this study using the anomalous 10hPa zonal mean zonal winds averaged over the period day 20 to day 30 (see the caption of Figure 3.5), the transient response of the vortex to CPW in case 20 is denoted as a weakening in

Figure 3.6, due to the weakening that occurred a few days after the initial minor strengthening (Figure 3.9a). Figures 3.9b and 3.10b indicate that positive anomalies of the eddy-driven MMC forcing in the stratosphere are responsible for the strengthening of the vortex in both CPW and EPW cases that start at day 20. The positive anomaly of the eddy-driven MMC forcing is much larger in magnitude in the EPW case (Figure 3.10b) compared to that in the CPW case (Figure 3.9b). This is the primary reason why the eddy-driven MMC forcing can overcome the negative anomaly associated with the eddy momentum forcing (Figure 3.10c) and lead to the overall transient strengthening of the vortex in response to EPW. In the CPW case, the weak positive anomaly of the eddy-driven MMC forcing (Figure 3.9b) is eventually dominated by the negative eddy momentum forcing anomaly (Figure 3.9c), resulting in the vortex weakening following the initial minor strengthening (Figure 3.9a). Consistent with case 4 and the ensemble average, the negative anomaly of the eddy momentum forcing found in case 20 is largely associated with its linear part, and the nonlinear part of the forcing due to CPW/EPW-forced variability produces a positive anomaly (Figures 3.9d,e and 3.10d,e). Additionally, in both case 4 and case 20, the negative anomaly in the linear part of the eddy-momentum forcing is primarily driven by the interaction between SST-forced variability and the internal variability of the extratropical atmosphere (i.e., the FV-IV term), while the interaction between SST-forced variability and the initial condition of the atmosphere (i.e., the FV-IC term) remains largely positive, especially in the lower stratosphere (figures not shown).

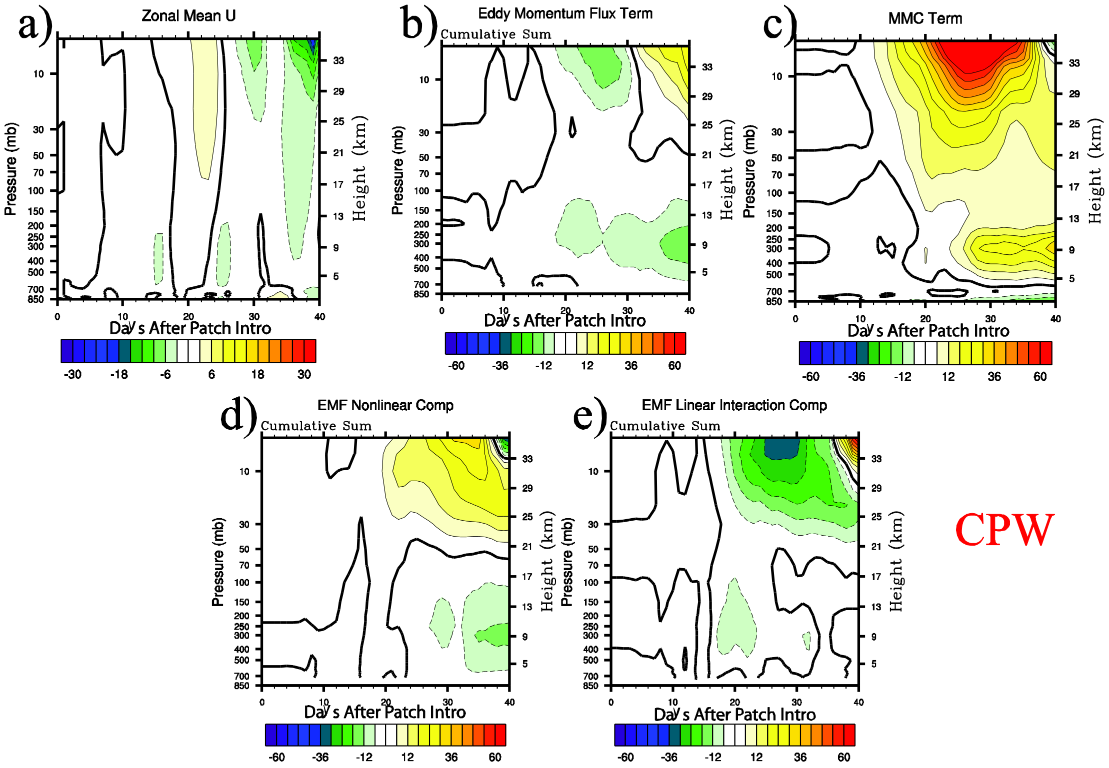

Figure 3.9. Same as Figure 3.7, except for the CPW patch run in case 20.

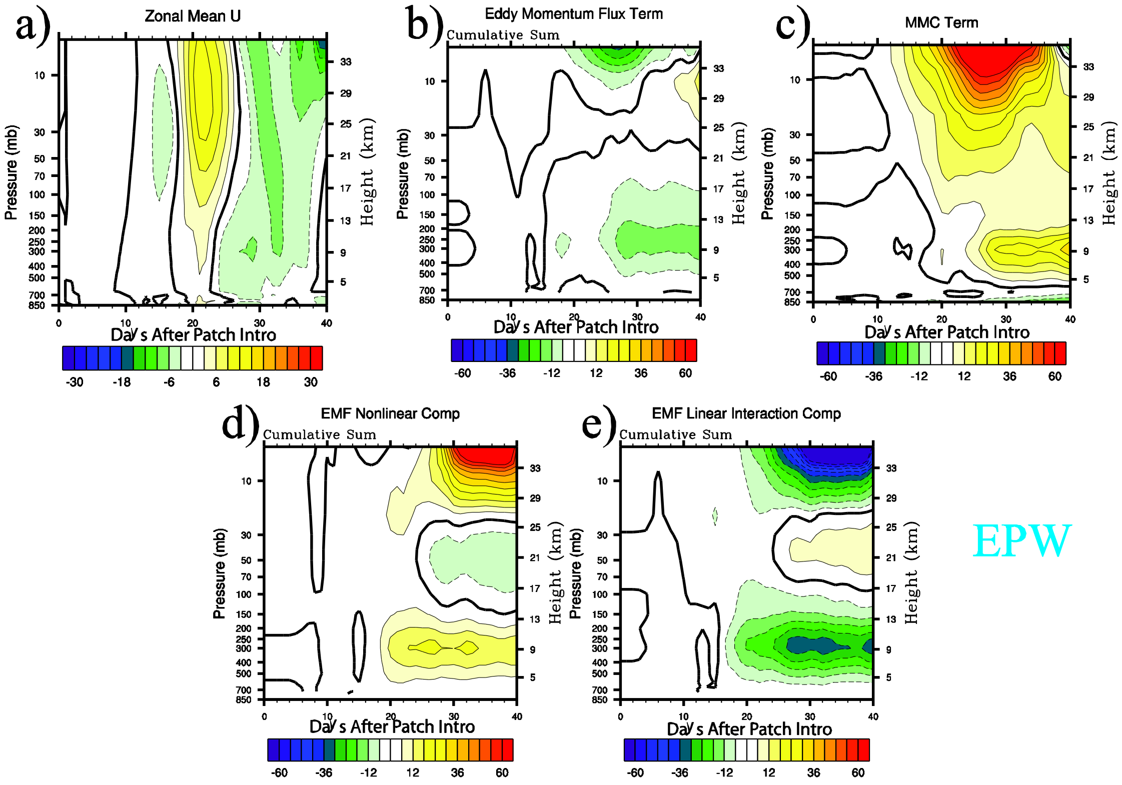

Figure 3.10. Same as Figure 3.7, except for the EPW patch run in case 20.

3.4 Section Summary and Conclusions

The purpose of this study is to identify the similarities and differences in terms of the initial, transient response of the stratospheric polar vortex to the central and eastern Pacific warming events. In our idealized modeling experiments, we introduce an elliptic patch of positive SST anomalies in the tropical Pacific to roughly mimic the mean structure and amplitude of a canonical CPW or EPW event. Two 20-member ensembles of 90-day simulations forced by these idealized tropical SST anomalies are conducted. The transient responses of the stratospheric polar vortex (defined in terms of the 10ha zonal mean zonal winds averaged over 50°N-80°N for the period day 20 to day 30) in the patch-runs where

SST anomalies have been applied are compared against those in the control run where climatological SSTs have been used. The differences in the transient response between the patch and the control runs are interpreted in a framework based on the quasi-geostrophic zonal mean zonal momentum equation on a beta plane.

Two important results arise from this analysis. First, we find that in the ensemble average, both the CPW and EPW forcing result in a transient weakening of the vortex. This response is the same sign as what has been shown in studies investigating the equilibrium response to CPW and EPW (e.g. Garfinkel et al. 2012). Both the eddy momentum forcing and the eddy-driven MMC forcing contribute to this weakening. Despite a few minor differences between the CPW and EPW ensemble average, the weakening occurs at a similar time (starting approximately 22 days after the SST anomaly is imposed) and location (throughout the stratosphere and the upper troposphere) under both types of warming events. Thus in an ensemble average sense, the transient response of the vortex to the CPW and EPW is very similar. Negative anomalies in the eddy momentum and eddy-driven MMC forcing jointly contribute to the initial weakening of the vortex. The eddy-driven MMC forcing is higher in magnitude thus plays a more significant role. Separating the eddy momentum forcing into a linear and a nonlinear component reveals that in the ensemble average, the nonlinear part, which involves only the extratropical wave response to the CPW/EPW forcing, contributes positively to the zonal mean zonal wind tendency. The linear part, which quantifies the interaction between the extratropical wave response to the CPW/EPW forcing and the initial state/internal variation of the extratropical atmosphere, is responsible for producing negative anomalies in the eddy momentum forcing. This contrast is consistent under both CPW and EPW forcing and the presence of two terms of similar magnitude but opposite signs leads to the total eddy momentum forcing being weakly negative. It is further shown that the negative anomaly associated with the linear part is primarily a result of the interaction between the SST-forced variability and the internal variability of the vortex. These facts lend further support (from the perspective of the initial transient response) to the linear interference mechanism that has been proposed to explain the connection between the stratospheric polar vortex variability and the tropical Pacific warming.

Second, although consistent initial weakening of the vortex is identified in the ensemble average of the CPW and EPW cases, not all of the individual ensemble members show this weakening. There are a few cases where the vortex initially strengthens in response to both the CPW and EPW forcing. The magnitude of this strengthening is equal to or less than the ensemble average (e.g. 20-30 average anomaly in 10 mb zonal mean zonal winds is 2.7413 m/s (10.1181) m/s in the CPW (EPW) case 20, compared to 8.8449 (10.0793) m/s in the CPW (EPW) ensemble average during the peak initial decrease), and approximately 1-1.6 standard deviations from the ensemble mean. The time scale of these strengthening events, 6-8 days, is shorter than the initial weakening in the ensemble average, which is more than 15 days. In case 4 and 20 where the vortex initially strengthens slightly, a positive anomaly in the eddy-driven MMC forcing plays a critical role in driving this strengthening, in contrast to the largely negative anomaly found in the ensemble average. Since the only differences between different individual ensemble members is the initial state of the atmospheric flow, the diverse response exhibited by individual members suggests that when initial transient response is considered (compared to the equilibrium response), the initial atmospheric state when the SST anomalies start emerging and the subsequent intrinsic evolution (internal variability) of the atmospheric flow also plays a non-trivial role in determining the time-dependent response of the vortex. In some cases, e.g., case 4, the importance of the initial state could outweigh the effect of a tropical Pacific SST anomaly.

In addition to the initial state affecting the wave forcing in the troposphere, which we highlighted in this manuscript, the initial state also affects the vertical propagation of tropospheric wave activity into the stratosphere. The distribution of potential vorticity in the basic flow, an important term in the squared wave refractive index (Andrews et al. 1987; Matsuno 1970) is crucial in determining the pathways of the vertical propagation of Rossby waves and the wave (eddy) forcing of the zonal mean flow in the stratosphere. Differences in the distribution of potential vorticity in the initial basic flow, and thus the favored pathways for vertical propagation of Rossby waves, between ensemble members could also explain the different vortex responses.

An immediate implication of this result is that in any individual year, knowledge about the tropical Pacific SST alone is not enough to make a skillful seasonal forecast for the state of the polar stratosphere. The initial state of the extratropical atmosphere must also be considered in order to understand the sub-seasonal evolution of the polar stratosphere. Therefore medium-range forecasts of the stratospheric response to tropical SST anomalies are likely to be sensitive to the initial atmospheric state in the model, along with other factors such as the QBO phase (Garfinkel and Hartmann 2007). The response is much more complicated than a simple consistent weakening effect across all CPW and EPW events. This may partly explain the contradictory results in the literature for the effects of CPW and EPW (e.g. Graf and Zanchettin 2012; Hegyi and Deng 2011; Xie et al.

2012), especially in reanalysis studies where only a limited sample size of CPW and EPW events are available. The initial state of the extratropical flow and wave structure in a given cool season when CPW or EPW occurs differs from year to year, and this difference likely translates into differences in how CPW or EPW modulates the strength of the stratospheric polar vortex in an individual season. Only when a large number of seasons are considered or long-term model integrations are used we may be able to identify an averaged weakening effect of CPW and EPW on the vortex strength, as shown in the ensemble average here.

Finally, we emphasize that the analysis conducted here only serves as a first step to understand how the polar atmosphere responds to the emerging tropical SST anomalies. There are a variety of related questions that cannot be addressed without a substantial amount of additional modeling and diagnosis work. These include questions related to the method that we used to isolate the effects of CPW and EPW, such as the sensitivity of the results to the slight changes in the magnitude/structure of the prescribed SST anomalies, the impact of Pacific cold events on the polar atmosphere, the sensitivity of the choice of the date from which the perpetual conditions of the model experiments are taken, and the potential complications when we incorporate into the analysis additional factors such as EPW events being stronger in amplitude compared to CPW events. There are also still some questions unanswered related to the dynamical mechanism that we propose here to explain the initial, transient vortex response to CPW and EPW. Although we present here the relative importance of the contributions of the eddy-driven MMC and eddy momentum flux to the initial vortex response, along with the contributions of the initial condition (IC), internal variability (IV), and forced variability (FV) components of the eddy momentum flux term, how exactly these components interact to produce the differences in response between ensemble members is subject for further study. Also, the relative importance of the effect of the initial state on the tropospheric wave forcing (e.g. Figure 3.6) and the vertical wave propagation from the troposphere to the stratosphere is another important consideration left to be explored in future work.

The work presented in this chapter is published in the Journal of Climate (Hegyi et al. 2014).

CHAPTER 4

DYNAMIC AND THERMODYNAMIC IMPACTS OF HIGH AND LOW FREQUENCY ATMOSPHERIC EDDIES ON THE INITIAL MELT OF ARCTIC SEA ICE

4.1 Motivation and Background

In chapter 4, the focus of the investigation shifts from the cool season to the beginning of the warm season. We apply the same framework of investigation used in Chapters 2 and 3 to the investigation of the melt of Arctic sea ice by looking at the influence of the tropics and Northern Hemisphere midlatitudes on the variability of the initial melt date of sea ice across the Arctic and in smaller subregions. The initial melt of Arctic sea ice in the boreal spring is the start of the melt season that extends through the warm season until September, when the areal coverage of sea ice is at a minimum (Figure 1.2). Recent years have exhibited record minimum September extents (e.g. 2007, 2012), relative to all other years in the satellite record of sea ice extent, and an accelerated trend of decline in the minimum September extent (Comiso et al. 2008). Additionally, it has been noted that the melt season leading up to the September minimum has become longer, with a trend towards both an earlier initial date of melt and later date of autumn freeze-up (Belchansky et al. 2004; Markus et al. 2009; Stroeve et al. 2014). A consequence of the longer melt season is an increased amount of incoming solar radiation absorbed at the surface during the length of the melt season (Perovich et al. 2007). Thus the earlier onset of melt has been proposed to explain the trend in the September minimum sea ice extent, since the extension of the melt season increases the cumulative amount of solar radiation absorbed at the surface and the energy available to melt Arctic sea ice (e.g. Stroeve et al. 2014).

To help explain the decrease in the September minimum, many studies have focused on physical processes that may explain the observed sea ice variability, the decreasing sea ice extent, or that help trigger extreme minimum years in the September minimum extent**.** Proposed important physical processes occurring during the melt season include direct ocean influences (e.g. Shimada et al. 2006) and thermodynamic and dynamical atmospheric influences on the Arctic sea ice. Important atmospheric thermodynamic processes include anomalies in components of the surface energy budget, such as positive near-surface downwelling shortwave (Kay and Gettelman 2009) and longwave (Dong et al. 2014) radiation anomalies. Important atmospheric dynamical processes include anomalous poleward energy transport into the Arctic (Graversen et al. 2011), anomalous transport of sea ice out of the Arctic basin by persistent anomalous winds (Ogi et al. 2008, Zhang et al. 2008, Ogi and Wallace 2012), anomalous regional atmospheric circulation patterns (Wang et al. 2009), abnormal summer storm activity (Screen et al. 2011), and the influence of important low-frequency modes and teleconnection patterns (e.g. the Pacific-North American pattern [PNA], L'Heureux et al. 2008). A complicating factor to incorporating these atmospheric processes into a physical mechanism that explains sea ice variability is that the thermodynamic and dynamic processes do not act independently. For example, cloud cover is a crucial source of downwelling shortwave and longwave radiation anomalies that are associated with sea ice anomalies, and the effects are dependent on the type of cloud cover present (Eastman et al. 2010). The distribution of cloud cover over the region is affected by the large-scale dynamics, and thus the thermodynamic and dynamic processes that help force sea ice anomalies can be coupled through the presence of clouds.

Given the potential importance of the lengthening of the melt season, particularly the trend toward an earlier mean melt, we investigate the role of atmospheric eddies in triggering the initial melt. The purpose of this chapter is to explore how these eddies contribute to the interannual variability and trend in initial melt of Arctic sea ice in late boreal spring, through both the eddy influence on meridional heat transport from lower latitudes (a dynamical atmospheric mechanism component) and through changes in the downwelling longwave and shortwave radiation at the surface (a thermodynamic atmospheric mechanism component). By looking at both the dynamic and thermodynamic components to the physical mechanism involving atmospheric eddies, we take an integrative view of the mechanism that is responsible for the variability and trend. We focus on the influence of high, low, and seasonal frequency eddies (HF LF, and SF eddies, periods of 2-7, 10-30 days, and 30-90 days, respectively) and associate the influence of these eddies with specific episodes of initial melt. The eddies may originate both inside and outside of the Arctic. The eddies originating outside of the Arctic represent a mechanism by which lower latitudes may influence Arctic sea ice variability and the declining September minimum sea ice extent. Thus eddies originating outside of the Arctic can be considered as a “bridge” influence and physical mechanism linking climate variability in lower latitudes to Arctic sea ice variability. Following the introduction, we outline the data and methods in section 4.2, and we present the major results in section 4.3 and 4.4. A summary of the results and concluding remarks are presented in section 4.5.

4.2 Data and Methods

The initial melt date data is taken from a dataset archived at the National Snow and Ice Data Center (NSIDC) and the data was created using a technique described in Drobot and Anderson (2001). The dataset contains melt dates that are derived from microwave brightness temperatures from the Scanning Multichannel Microwave Radiometer (SMMR) and the Special Sensor Microwave/Imager-Special Sensor Microwave Imager/Sounder (SSM/I-SSMIS) satellites, and covers the period 1979-2012. The data exist on an Equal-Area Scalable Earth (EASE) grid with a spatial resolution of 25 km. This dataset contains an area of missing data around the pole north of 84.5°N latitude for the period 1979-1987 and north of 87.2°N for the period after 1987. For consistency, when calculating the trend in initial melt date over the 1979-2012 period, we consider only the initial melt date data south of 84.5°N for all years. The temporal resolution of the data is daily after 1987 and 2 days prior to 1987. When quantifying the total melt on a given day in a particular region, we count the total number of grid boxes that exhibit melt on that date in the dataset. For dates before 1987, the daily count is calculated as half of the total count in the raw data if data exists on that date, and as half of the count recorded on the previous day if it does not. The mean melt date at any location is simply the mean of the time series of melt dates at that location. The mean melt date over a defined area is mean of the collection of mean melt dates over the defined area.

Two datasets are used for the calculation of atmospheric quantities. For heat transport, temperature and wind quantities, we use the NASA Modern Era Retrospective Analysis for Research and Applications (MERRA) reanalysis dataset on a 0.5° latitude by 0.67° longitude grid (Rienecker et al. 2011). The MERRA reanalysis dataset represents the state of the atmosphere over the Arctic very well, and it has been shown to be among the reanalysis datasets that best matches independent observations of atmospheric conditions in the Arctic (Lindsay et al. 2014). For longwave and shortwave radiative flux data, we use datasets from the NASA Clouds and the Earth's Radiant Energy System (CERES) project (Wielicki et al. 1996) that contain all-sky longwave and shortwave surface fluxes. This daily data exists on 1° latitude by 1° longitude grid and covers the period 2000-2014. The data is derived from observations by the Terra and Aqua satellites, part of the NASA Earth Observing System (EOS).

From the MERRA reanalysis data, we calculate the lower troposphere meridional heat transport, defined here as the mass-weighted vertical average of meridional heat transport (i.e. the product of V and T) from 1000 to 500mb. A 203-weight Lanczos bandpass filter over daily data from 1979-2012 is used to isolate the high-frequency (HF) eddy component of the heat transport. The filtering is applied to wind and temperature components of the heat transport first, before the vertical and spatial averaging is performed. Three separate bandpass filters are applied to isolate the high-frequency, low-frequency, and subseasonal frequency eddies (HF, LF, and SF, respectively). HF eddies in this study are defined as eddies with the period of 2-10 days, LF eddies are defined as eddies with the period 10-30 days, and SF eddies are defined as eddies with period 30-90 days.

When calculating spatial averages, we define the Arctic polar cap as all points north of 70°N latitude. This latitude boundary is also the boundary over which we calculate the meridional heat transport. The Arctic cap mean melt date is the average melt occurs across this polar cap. When looking at individual sectors across the latitude circle, we longitudinally average over 5-degree sectors before plotting the data. The melt date mean (i.e. the mean melt date over the sector) and melt count (i.e. the number of grid boxes that exhibit melt for that date) are done over these 5-degree longitude sectors and bounded by 70°N and 90°N, except in the time-longitude plots for individual years. For the melt date mean, we focus on the boreal spring melt. Subsequently, melt dates before day 90 (i.e. before March 31) are discarded before calculating the mean.

4.3 Trend in mean melt date and eddy heat transport climatology

There is a strong association between the mean melt date over the entire Arctic polar cap and the September minimum sea ice extent. Figure 4.1 shows the scatter plot between the September minimum sea ice extent and the mean melt date across the polar cap north of 70°N. A strong positive correlation (R=0.7420, significant at the 99% level) exists between the mean melt date and the September minimum for the entire 1979-2012 period, such that lower September minimum sea ice extent values are associated with earlier polar cap mean melt dates. The correlation is mainly driven by the decreasing trend in both the September minimum and the mean melt date. This is consistent with the hypothesis put forth by previous studies about the relationship between the early melt season and the September minimum extent (e.g. Stroeve et al. 2014). Additionally, when we divide the 34-year period of the data into two halves, the earliest melt dates and smallest September extent values are found in the second half of the period (marked by blue diamonds in Figure 3.1). Thus, both the Arctic polar cap mean melt date and the September minimum extent show similar declines in recent years, and their correlation is mainly driven by the trend in both time series.

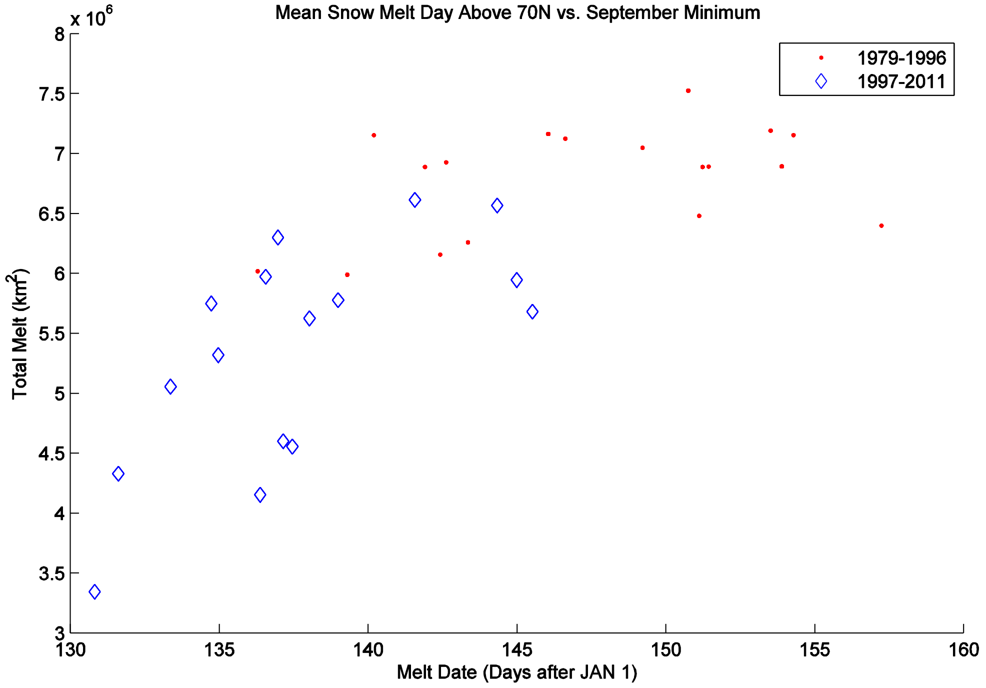

Figure 4.1. Scatter plot of Arctic polar cap mean melt date (x-axis, in days after January 1) and the September minimum sea ice extent (y-axis, in km^2) for each year from 1979-2012. Polar cap is defined as area above 70 degrees North latitude. Values for 1979-1996 (1997-2012) are denoted by red dot (blue diamond) markers.

A closer look at the longitudinal distribution of the mean initial melt date reveals that the trend in the mean initial melt date is not evenly distributed across all longitudes. In Figure 4.2a, the values shown are the mean values in a 5-degree longitude sector, bounded by 70°N and 90°N latitudes. Two interesting features exist in this figure. First, there is a clear decreasing trend in the melt date from 90°E to 130°W, which corresponds to an area that extends eastward from the central Siberian coast to the Beaufort Sea. Throughout this manuscript, we will refer to this sector as the Siberian sector. Interestingly, the trend in this sector is not consistent across the entire time period Rather, the decrease is most pronounced around and after 1990. Second, there is large interannual variability, with years that show consistently early or late initial melt across large longitude sectors (e.g. 1990, 2000, 2009), relative to surrounding years. These two characteristics also appear when plotting the mode (Figure 4.2b). The mode is calculated in each of the same 5-degree sectors as in the mean and for each year. Since there is one initial melt date at each grid point in the sector, the mode represents the most common initial melt date in each 5-degree longitude sector for a particular year. A close inspection of Figure 4.2b reveals that there are many bands of similar or identical mode dates oriented horizontally across the plot. Nearly identical and adjacent mode dates in the bands can be interpreted as the signature of a large melt event, which is sufficiently large in spatial extent to appear as the maximum in several sectors for that particular year. Such large melt events are possibly initiated by a common large-scale atmospheric or oceanic feature. Additionally, there is a decreasing trend in the mode of the melt date across the Siberian sector, meaning that the most common date of the initial melt signature has also been occurring earlier in recent years, similar to what is observed for the mean melt date.

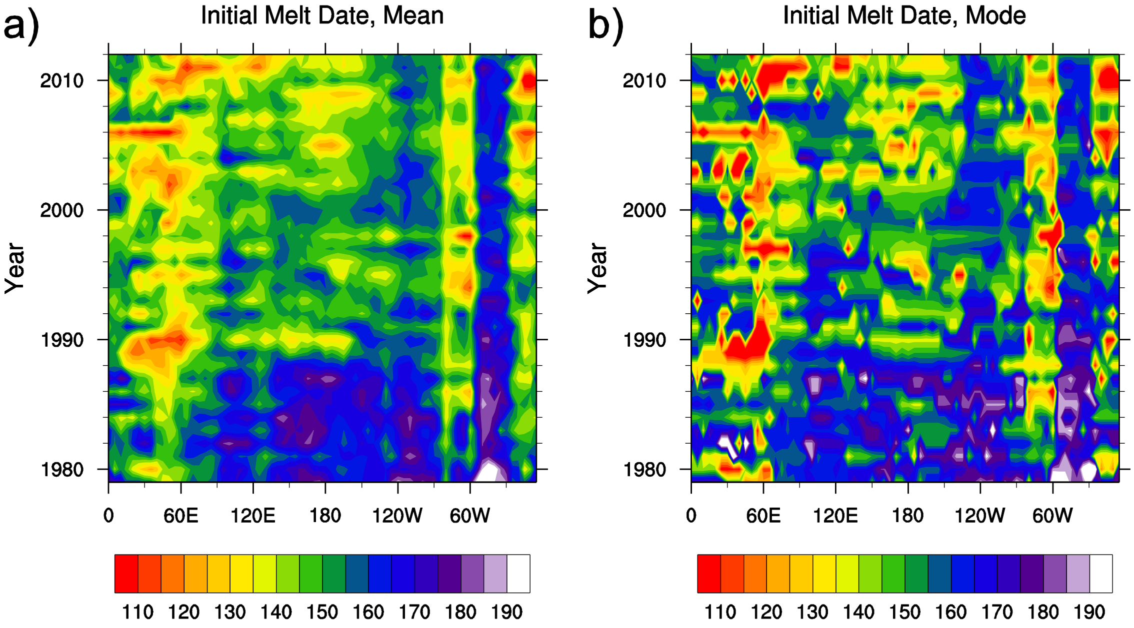

Figure 4.2. a) Mean melt date across the polar cap (north of 70°N) for each year in the 1979-2012 period. Each value plotted is the average across a 5 degree longitude sector, starting from 180 degrees West (i.e. the value plotted at 100 degrees East longitude is the average in the box bounded by 100 degrees East and 105 degrees East in the east-west direction and 70 degrees North and 90 degrees North longitude in the north-south direction). b) Same as a), but the mode of the melt date in each 5 degree longitude sector.

Climatologically, at the time of the initial melt, the magnitude of the direct eddy heat transport by the different frequency eddies is similar and positive. Figure 4.3a shows the climatological meridional heat transport directly by high, low, and subseasonal frequency eddies. Heat transport in each frequency band is of similar magnitude and almost exclusively positive, peaking around 340°E (20°W). In the Siberian sector (90°E to 230°E in Figure 4.3), the HF and LF heat transport is similar magnitude and larger than the subseasonal frequency transport in the western part of the Siberian sector. In the eastern part of the sector, all three components are of similar magnitude. The climatological magnitude of the cross terms, which represent the interaction of eddies in the three defined frequency band with each other and the seasonal-mean (i.e. the 30-day average centered on that date) wind and temperature fields, is presented in Figure 4.3b. The greatest magnitude cross term is the product of the subseasonal-frequency wind and mean temperature near 0°E, denoted here as VS*Tbar. Within the Siberian sector, this quantity peaks around 180°E longitude. The product of the high frequency wind and seasonal mean temperature (i.e. the VH*Tbar term) is also climatologically positive in some parts of the Siberian sector. As we will later show, these two terms are important and associated with the initialization of significant initial melt episodes that we explore in section 3.3, even though the high frequency cross term is lower magnitude in the climatology than the other terms. The product of the low frequency wind and seasonal mean temperature (i.e. the VL*Tbar term) is climatologically positive in some parts of the Siberian sector, and is the second largest cross term in the climatology in terms of magnitude. However, we will show later that is plays a more minor role in the initialization of significant initial melt episodes. The remaining cross terms have very small magnitudes (magnitudes of less than 1 K*m/s) relative to the terms presented in Figure 4.3b, and thus are not shown in the figure.

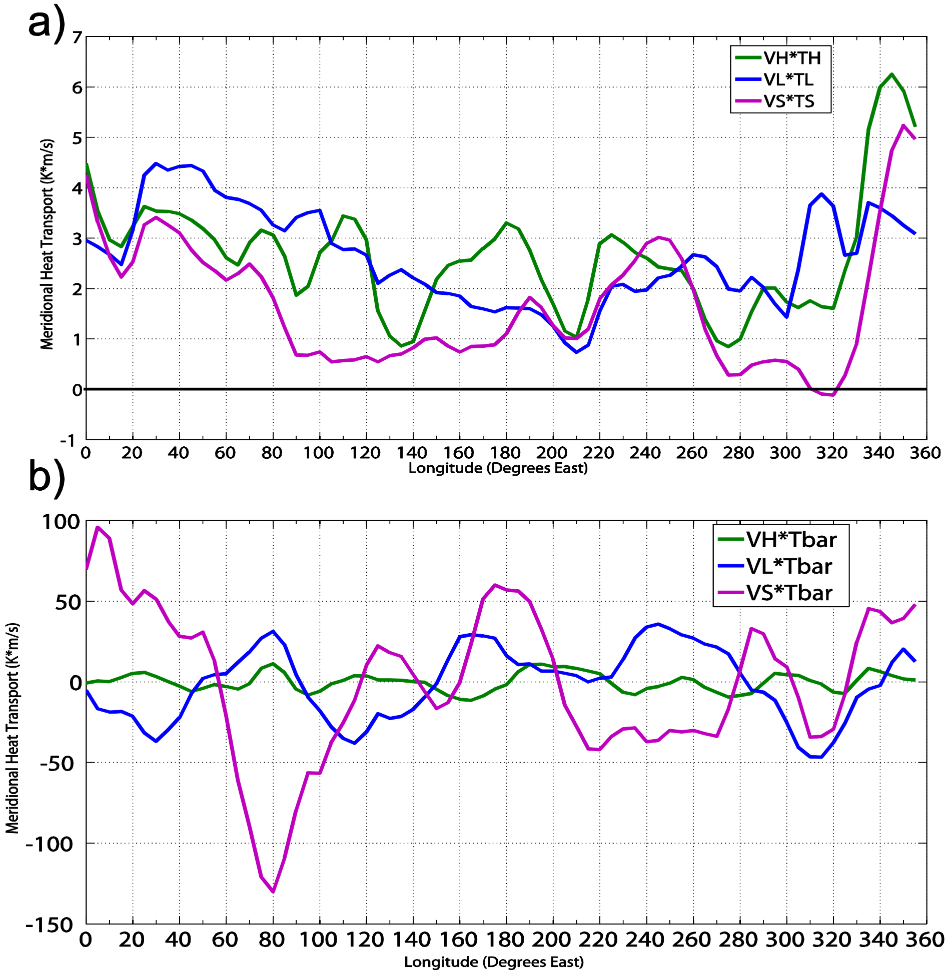

Figure 4.3. a) Climatology of lower troposphere meridional heat transport across 70°N by high, low, and subseasonal frequency eddies (H, L, and S, respectively), averaged from day 110 to 140, corresponding to date range April 20th to May 20th. Heat transport values are mass-weighted and vertically averaged from 1000 to 500 mb, and the data are binned similarly as in Figure 4.2. b) Climatology of significant cross terms of the lower troposphere meridional heat transport across 70°N. Date range and binning is identical as in a). The bar term in each cross term represents the seasonal mean (i.e. 30-day) average temperature.

4.3.1 Connection between eddy heat transport and mean melt date trend

To investigate the relationship between the trend in the initial melt and the temperature and lower troposphere heat transport quantities, we explore the time evolution of each quantity in more detail. In the time evolution of the date of the initial melt each year in the Siberian sector (Figure 4.4a), there is a steady trend towards an earlier melt date, in both the mean and in the extreme early and late dates in the initial melt season. The mean melt date decreases from day 167 (June 16th) to day 138 (May 18th) from 1979 to 2012, a decline of 29 days over 34 years. After 1987, both the earliest and latest initial melt decline at a similar rate to the mean, so that the length of the period over which the initial melt is occurring in this sector is nearly constant. The initial melt occurs over a period when the mean surface temperature in the Siberian sector is increasing steadily and plateauing to near and slightly above freezing by the end of the initial melt period (comparing Figures 4.4a and 4.4b).

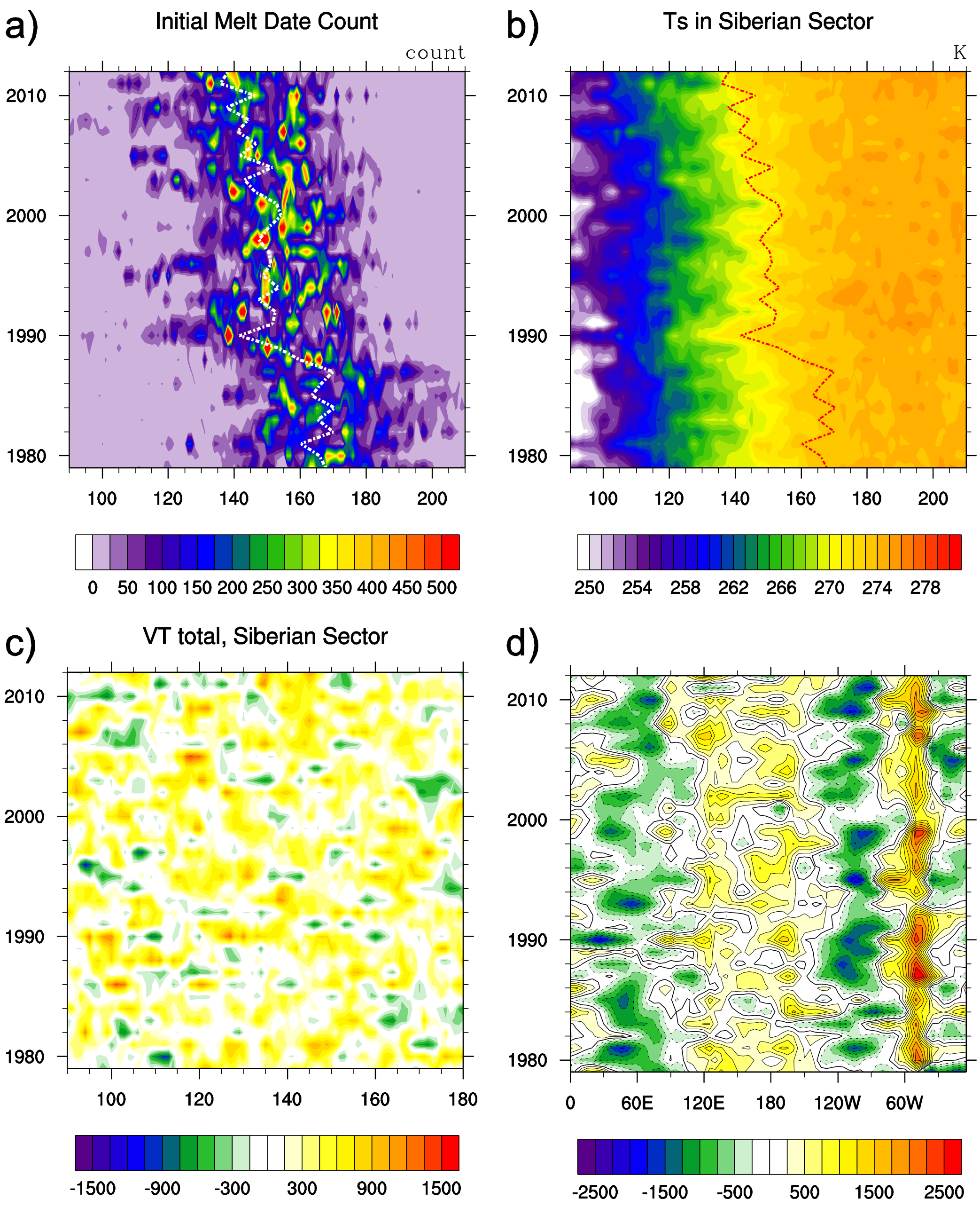

Figure 4.4. a) Total count of number of 25km*25km grid boxes exhibiting the melt signal for each day and year in the sector of interest (90°E-130°W). b) Average surface (10-meter) temperature in the sector of interest (units: K), averaged over 70°N-90°N. Dashed lines in both figures represent the mean melt date over the same sector for each year in the 1979-2012 period. This line is identical to the white line in a). c) Total daily lower-troposphere meridional heat transport (units K*m/s) into the sector of interest across 70°N for each year in the 1979-2012 period. d) Total lower troposphere meridional heat transport across 70°N in each longitude sector, summed over day 110-140, which corresponds to the start of the initial melt in this sector. The date range is identical to the date range used in Figure 4.3b.

Unlike the trend in the mean melt date in Figure 4.4a, the trend in the surface temperature (Figure 4.4b) and meridional heat transport (Figure 4.4c and 4.4d) over the 34-year period is less apparent. Although the heat transport is positive in the Siberian sector longitudes, there is no increasing trend in heat transport at any longitude. Despite the lack of trend, there are definite qualitative links between individual melt events in a given year and the heat transport. Several individual melt events where a large area undergoes initial melt exist in Figure 4.4a (e.g. day 138 in 1990, day 133 in 2011, and day 140 in 1993). These events dominate the melt in certain years and some are associated with large positive values of heat transport either on the date of the event or immediately preceding it. The melt on day 138 (133) in 1990 (2011) occurred over an area equal to 12.41% (7.73%) of the total area in the Siberian sector and 6.70% (4.38%) of the total area that experiences melt over the Arctic polar cap, the largest melt event in area in both spatial domains for that year. In the next section, we will investigate in detail how heat transport and other factors help trigger the initial melt events.

4.4 Initial Melt Events in Individual Years

We first examine the melt event on day 138 in the year 1990 (see Figure 4.4a) to determine which meridional heat transport term is most associated with the melt event. In Figure 4.5a, we plot the daily evolution of the initial melt count at each longitude. The melt event is clearly found centered at day 138 and extending from 150°E to 150°W longitude. The event is also by far the greatest melt event in magnitude in any sector in the early melt season of 1990. Figure 4.5b shows the time series of total heat transport and other important components with day zero indicating the peak of the melt. Immediately preceding the peak of the melt event, there is a period of large-magnitude positive total heat transport, starting from 4 days before the melt event. A major component of the total heat transport in this period is the cross term containing the product of the HF wind and the climatological mean temperature, with a nearly equal contribution from the product of the SF wind and the climatological mean temperature. The low frequency cross term is only a minor contributor to the peak in heat transport around day zero. The change in the total heat transport closely matches the change of the HF cross term with time. The heat transport from the SF cross term and climatology are both positive, and thus the total heat transport remains above zero for most of the period highlighted. Additionally, these two terms were identified in Figure 4.3b as significant components of the climatological meridional heat transport in this sector. The magnitude of the heat transport directly resulting from the LF and HF eddies (dashed lines in Figure 4.5) is much less than the two cross terms (solid lines in Figure 4.5), thus the meridional heat transport that results from the interaction of the eddies with the background temperature field may be more crucial to the initial melt in this event than the meridional heat transport generated purely by the eddy temperature and meridional wind fields.

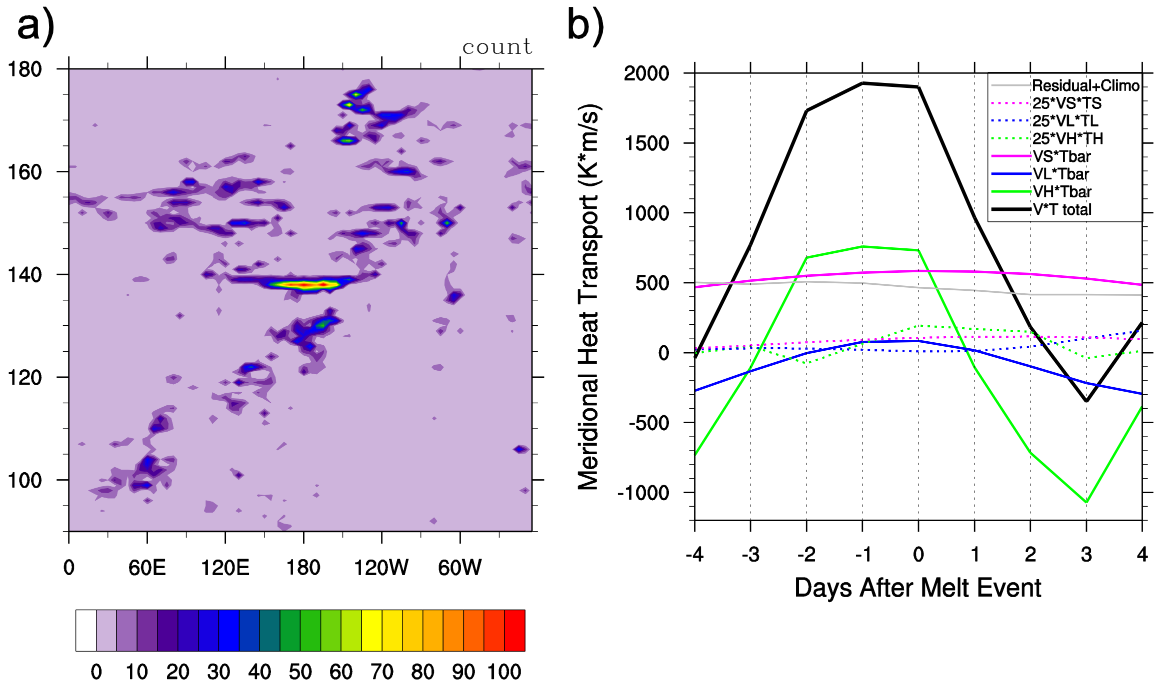

Figure 4.5. a) The daily count of the total number of 25km*25km grid boxes exhibiting an initial melt signature in the year 1990. b) The total meridional heat transport across 70°N latitude for the melt event identified in Figure 4.5a (extending from 150 degrees East to 150 degrees West longitude). Day 0 is the date of peak melt area (day 138). For visibility, the HF and LF components are multiplied by 25.

The area of melt at day 0 is associated with a broad area of meridional heat transport from 150°E to 150°W longitude (Figure 4.6a). In the sea level pressure fields (not shown), the increased meridional heat transport is associated with an area between a trough of low pressure centered around 150°E and an area of high pressure further east. In between these two features, there is broad southeasterly flow that accounts for the positive meridional heat transport. These features also appear in the 500 mb geopotential height field (not shown).Interestingly, when plotting the time-longitude evolution of total heat transport, the large positive value associated with the melt episode is at the eastern end of a diagonal feature on the plot. The diagonal feature begins around day 133 at 90°E longitude (Figure

4.6b) and propagates eastward. These diagonal features suggest a persistent meridional heat transport as a result of one feature propagating eastward with time. In this case, the propagating feature is the southerly winds between the high and low couplet. Several of these diagonal features appear in Figure 4.6b, suggesting that propagating large-scale features regularly affect the meridional heat transport across this latitude for this particular year.

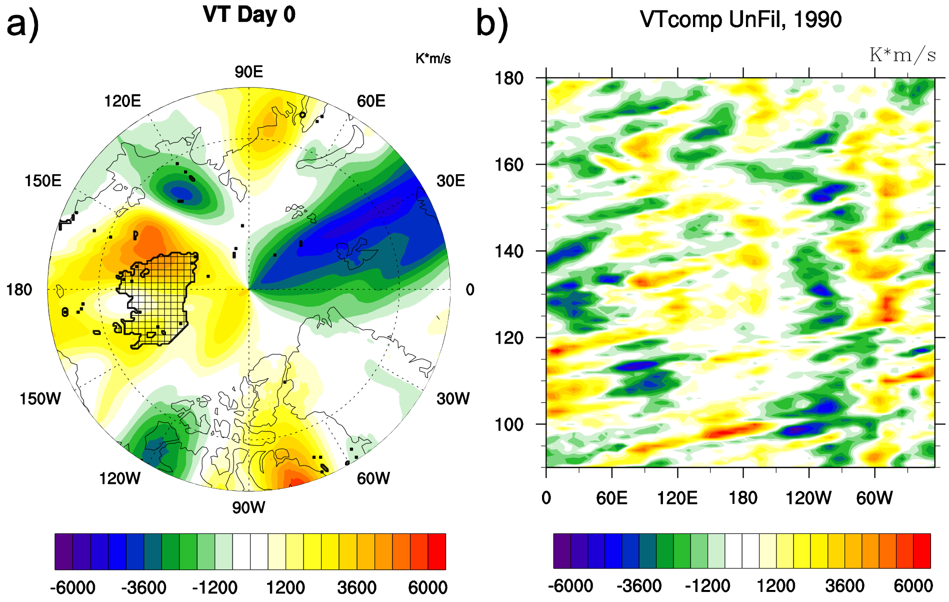

Figure 4.6. a) The meridional heat transport (units K*m/s) at day 0 of the melt event identified in Figure 4.5 for the year 1990. The area that exhibits the initial melt signature on this date is hatched. b) The daily meridional heat transport (units K*m/s) across 70°N at each longitude.

Another significant melt event in 2011 on day 133 is highlighted in Figure 4.7a. In this event, total meridional transport in the sector of the melt is highly positive beginning 2 days before the melt event (Figure 4.7b). Similar to the 1990 case, the product of the high- and subseasonal-frequency wind with the seasonal mean temperature field are the largest components of the highly positive heat transport. Also like the previous case, the direct eddy heat transport does not significantly contribute to the peak heat transport, indicating that the increase of total heat transport is mainly driven by the cross terms representing the interaction of the HF and SF eddies with the mean temperature. Further, the melt is collocated with an area of positive heat transport extending northward from just east of the dateline (Figure 4.8a). Unlike in the 1990 case, the increase in heat transport associated with the melt event is not associated with a long-lived heat transport anomaly (Figure 4.8b). The diagonal banding of heat transport is still present in this year, but a band of increased heat transport is not directly associated with the melt event. However, similar to the 1990 event, the melt is found in a region of southerly flow between a high and low couplet, with the trough of low pressure in the SLP field centered around 180°E and the high found further east (not shown).

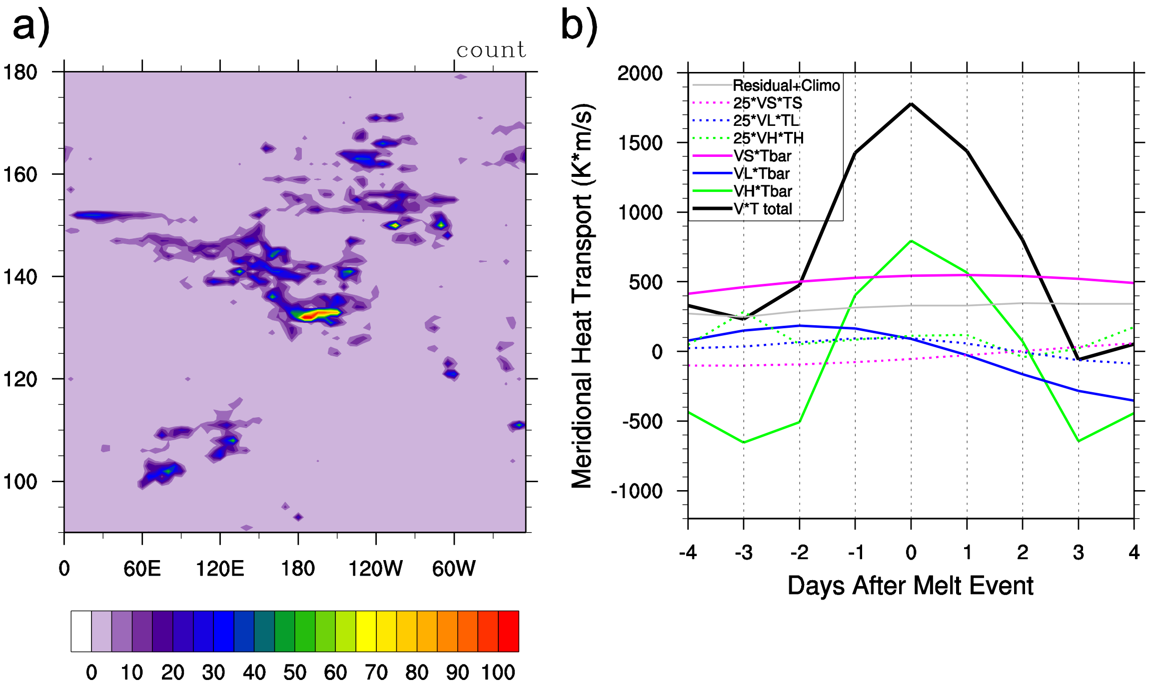

Figure 4.7. Same as Figure 4.5, but for 2011. b) is centered on the event at day 133 and averaged from 180-150°W longitude.

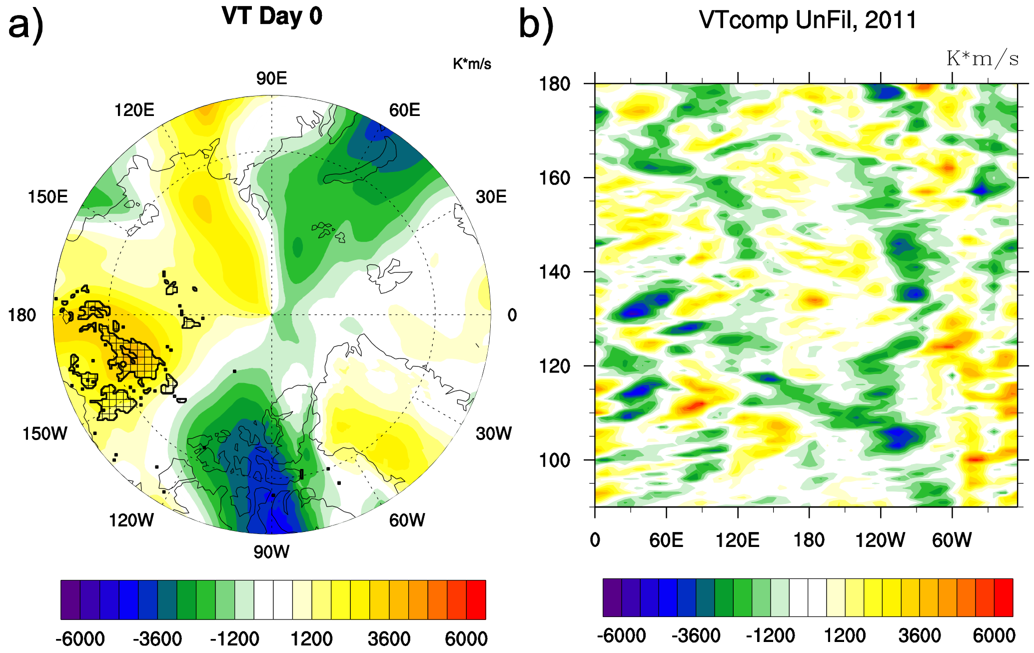

Figure 4.8. Same as Figure 4.6, but for the melt event in 2011.

In the previous analysis, the focus has been on the effects of eddy meridional heat transport, a dynamical component of atmospheric eddies directly driven by the interaction of the eddy-generated wind field and climatological temperature field. Another way by which atmospheric eddies may affect the initial melt is through effects on the surface energy budget, specifically through anomalies in downwelling shortwave and longwave radiation. The presence of water vapor in the atmospheric column as well as cloud cover anomalies associated with the eddies both contribute to anomalous downwelling longwave and shortwave radiation at the surface. High levels of water vapor in the atmospheric column increase the amount of downwelling LW radiation at the surface since water vapor is an effective greenhouse gas. Clouds both increase the downwelling longwave radiation through absorption and emission of energy towards the surface and decrease shortwave radiation through reflection of incoming solar radiation. In the cool season, the longwave cloud radiative forcing dominates due to the lack of incoming solar radiation during the polar winter. In the warm season, the shortwave cloud radiative forcing is a nonzero contributor to the total cloud radiative forcing, as incoming solar radiation increases. In the early warm season, however, the net shortwave cloud radiative effect is tempered over areas with ice cover. Over high albedo surfaces, such as ice-covered surfaces, clouds do not significantly increase the total amount of shortwave radiation reflected, thus the net shortwave cloud radiative effect is small. Atmospheric eddies modify both the water vapor in the atmospheric column and the distribution of clouds, and thus can have significant effects on the surface radiation and energy budget.

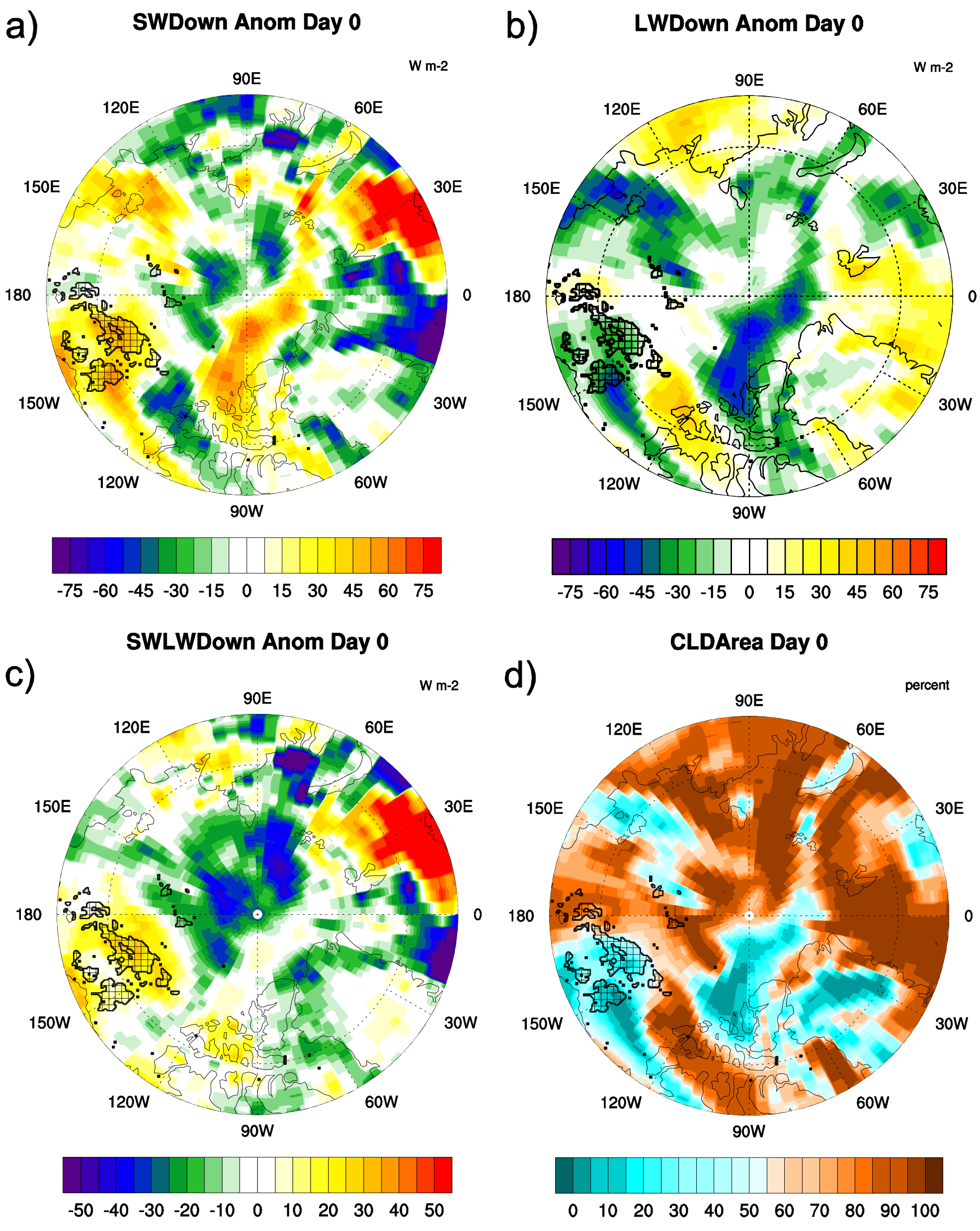

Figure 4.9. Surface downwelling a) shortwave, b) longwave, and c) longwave plus shortwave anomalies (units W/m^2) at day 0 for the 2011 melt event. Anomalies are calculated relative to a 2000-2013 climatology. d) The total cloud area, in terms of percent sky coverage, at day 0 for the 2011 melt event. The area that exhibits the initial melt signature on this date is hatched.

We explore the downwelling radiation anomalies associated with the melt in the 2011 event by examining the anomalies in the downwelling shortwave (SW) and longwave (LW) at the surface in the CERES data (Figure 4.9), which are calculated relative to a 2000-2012 climatology. We exclude the event in 1990 from the analysis of the surface SW and LW anomalies, as the event occurs outside of the time period covered by the CERES data. Qualitatively, there is a negative correspondence between the shortwave and longwave anomalies across the region (Figure 4.9a and 4.9b). Negative (positive) anomalies in surface downwelling LW are generally collocated with positive (negative) anomalies in surface downwelling SW. This is consistent with the effects of cloud cover on downwelling radiation at the surface. A high percentage of total cloud cover exists in areas where there are positive LW anomalies and negative SW anomalies, and areas of little cloud cover exhibit negative LW anomalies and positive SW anomalies (Figure 4.9d). In the region of initial ice melt (i.e. the main hatched area in Figure 4.9), positive downwelling SW anomalies exist, associated with an area of decreased cloud cover (Figure 4.9a and 9d). In addition, negative LW anomalies exist over the initial melt area (Figure 4.9b). The sum of these two anomalies results in a total increase in downwelling SW and LW radiation of 10-30 W/m^2 at the surface (Figure 4.9c). The increased downwelling radiation supports warming at the surface and is consistent with the existence of area of initial melt. The positive SW downwelling radiation anomaly is associated with an area of clear skies, which allows for increased incoming solar radiation. In the sea level pressure field on this date (not shown), the area of melt and lack of cloud cover is found on the western flank of a high pressure system with southwesterly flow from lower latitudes.

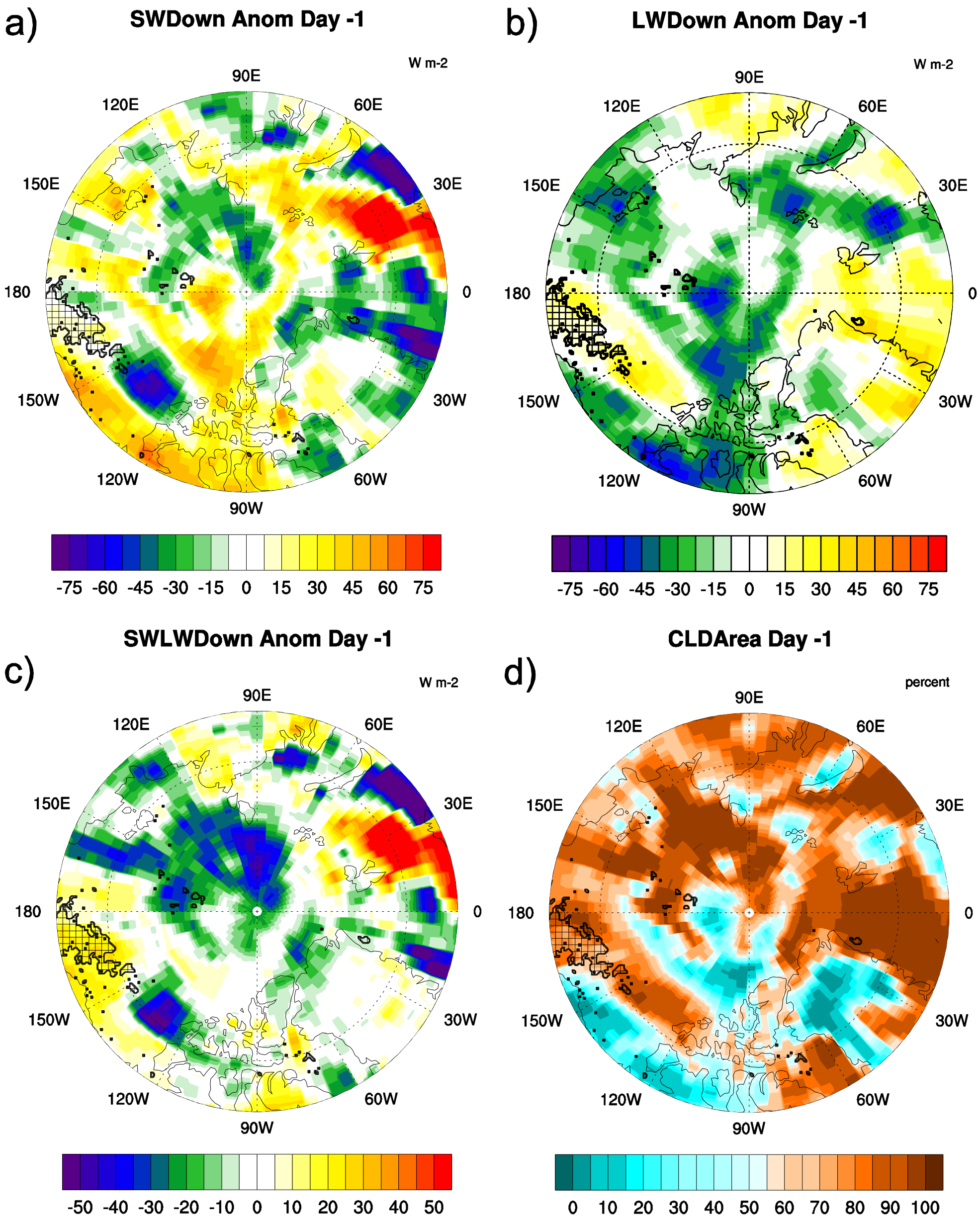

Figure 4.10. Same as Figure 4.9, but for the day before the peak melt date.

Thus, the combination of the surface radiative flux anomalies and the anomalous meridional heat transport help initialize the melt in the 2011 melt event. Atmospheric eddies help force both anomaly fields through their effects on heat transport and cloud cover. In the example shown for this particular melt event, SW anomalies are supportive of the melt on the date of maximum melt. However, this is not case on the previous day, where positive LW anomalies precede the initial melt (Figure 4.10b). Increased cloud cover accompanies the positive LW anomalies and the initial melt area. Thus, the melt event in 2011 is a prime example of how anomalies in both downwelling LW and SW radiation at the surface can complement the anomalous heat transport by atmospheric eddies and contribute to the initial melt of Arctic sea ice.

4.5 Summary and Conclusions

The purpose of this paper was to explain the decline in the mean initial melt date across the Arctic polar cap (i.e. all areas north of 70°N latitude) and show the importance of atmospheric transient eddies in helping trigger the initial melt of Arctic sea ice. We calculated the lower tropospheric meridional heat transport across the boundary of the polar cap using the NASA MERRA reanalysis dataset, bandpass filtering this quantity to isolate the high-frequency (HF), low-frequency (LF) and subseasonal-frequency (SF) eddy components. In addition, we briefly analyzed NASA CERES downwelling longwave and shortwave surface flux data to quantify the surface radiative flux anomalies associated with one case of initial melt over large areas of the Arctic.

In the first part of the results, we identify the regions in the Arctic in which trends in initial melt exist and show the climatological characteristics of the total and eddy meridional heat transport in the sector where the trend is most pronounced. We also show that the decline in the September minimum sea ice extent is coincident with an earlier occurrence of the initial melt of sea ice across the Arctic polar cap (Figure 4.1). In a plot of the mean melt date in each 5-degree longitude sector, the trend of earlier melt is primarily confined to the sector extending from 90°E to 130°W longitude, which corresponds to the seas north of northeast Siberia and Alaska (Figure 4.2). In this region, a decline in the mean melt date of 29 days from 1979-2012 exists, with both the start and the conclusion of the initial melt period occurring earlier. Both direct meridional heat transport by eddies in all three frequency bands across 70°N is positive and greatest for SF eddies (Figure 4.3). The cross terms that represent the interaction of the subseasonal and low-frequency eddy winds with the climatological mean temperature field are the largest component of the total heat transport, a larger component than the direct product of the eddy wind and temperature fields.

In the second part of the results, we focus on the mechanisms that help explain the recent declining trend and interannual variability in the initial melt date. The trend in earlier melt cannot be explained by a trend in the total meridional heat transport through the whole Arctic polar cap or any individual longitude sector (Figure 4.4c and 4.4d). However, individual melt events over which the initial melt occurs over a large area dominate the melt in some years, and these events are associated with meridional eddy heat transport anomalies. For example, when looking at two melt events in 1990 and 2011 which affected a large area across the Siberian sector, the melt event was immediately preceded by a large magnitude positive total meridional heat transport. The cross terms VS*Tbar and VH*Tbar, which represent the interaction between the seasonal and high frequency eddies and the seasonal mean temperature field, were the largest magnitude heat transport terms at the time of the melt event in the decomposition of the total meridional heat transport (Figure 4.5 and 4.7). In both melt events, the melt was located in a broad area of positive heat transport across the western Arctic Ocean (Figure 4.6 and 4.8). Additionally, anomalies in the downwelling shortwave and longwave radiation at the surface also accompany the 2011 melt event. A positive surface SW anomaly and negative surface LW anomaly is collocated with the melt on the melt date (Figure 4.9). On the previous day, LW anomalies associated with an area of clouds is located over the area of melt (Figure 4.10). However, on both days, there is a positive anomaly in the *sum* of downwelling SW and LW at the surface is collocated with the melt.

There are several important implications of these results. A primary finding was that the trend in earlier initial sea ice melt is not directly related to a trend in lower troposphere eddy meridional heat transport. However, there is some evidence presented here of the influence of individual eddies on the initial melt of Arctic sea ice. This may mean that the trend is a result of a mechanism that is not related to lower troposphere atmospheric heat transport, but instead is related to other processes that contribute to polar warming amplification such as surface albedo feedback or net cloud feedback (Taylor et al. 2013), or an accumulation of local mechanisms that contribute to the trend. Nonetheless, these results show that the initial melt of Arctic sea ice is a process that is episodic, where distinct melt events drive the initial melt in a given year. The eddy influence on the initial Arctic sea ice melt represents another possible mechanism by which lower latitudes may influence the climate of the Arctic. Atmospheric eddies affect both the local surface energy budget through positive meridional heat transport, associated LW and SW anomalies related to cloud cover, and through the effects on the albedo of the ice surface during the initial melt. Additionally, the early melt initialized by the eddies can persist and affect the later melt season through the cumulative effects on downwelling SW flux absorbed at the surface by the ice and sea surface. If this mechanism is an important contributor to the variability of sea ice in a given melt season, then it is crucial to properly simulate the atmospheric eddy influence from lower latitudes when modeling the melt of Arctic sea ice.

In summary, the results highlighted in this study show how both meridional heat transport and surface LW and SW anomalies are associated with specific initial melt events, and thus are an initial investigation on how the interaction between the dynamics (the atmospheric eddies) and thermodynamics (the LW and SW anomalies) play a role in initializing the melt. However, a remaining question is whether this dynamic/thermodynamic interaction is important in initial melt events throughout the Arctic outside of the Siberian sector. In this study, we also only explore a few specific cases where there is a relatively large melt event and do not consider in detail the duration of the melt after the melt is initialized by eddy influences. The crucial link between the initial melt and the September minimum extent at the end of the melt season is the cumulative effect of the melt after it is initialized, since the extra absorbed incoming shortwave radiation is the energy source for the extra melt of Arctic sea ice in the surface albedo feedback. Thus, the persistence of the melt after it is initialized is crucial to the effects of an early initial melt of Arctic sea ice persisting through the entire melt season.

Part of the work presented in this chapter is in preparation to be submitted to the Journal of Climate (Hegyi and Deng 2015).

CHAPTER 5

CONCLUDING REMARKS

In this dissertation, we explored the role of atmospheric mechanisms with thermodynamic and dynamic components in the coupling of Arctic hydroclimate with tropical and midlatitude climate variability. These linking mechanisms were found to important in explaining part of the decadal variability of boreal winter Arctic precipitation, the variability of the strength of the stratospheric polar vortex in boreal winter, and the initial melt of Arctic sea ice in late boreal spring. The goal of the research presented here was to increase our understanding of what drives each example of Arctic variability through better understanding of the linking mechanisms.

5.1 Dissertation Summary and Implications

In the results presented in Chapter 2, the coupling of the lower latitudes and Arctic hydrodynamics were explored in the cool season, specifically through the effects of CPW and EPW on the strength of the stratospheric vortex (i.e. the magnitude of the zonal mean zonal winds in the subpolar stratosphere) and decadal variability of Arctic precipitation. Pronounced decadal-scale variations in cool-season Arctic precipitation were identified in the GPCP and CMAP precipitation datasets and the MERRA reanalysis dataset. In the regression of a defined index for Arctic precipitation and SSTs, a statistically significant pattern of SSTs in the tropical Pacific that resembled the CPW SST signature appeared in the results (Figure 2.3a). A similar SST pattern appeared with a regression of a 7-year smoothed AO index. This result suggested a link between the decadal variability of Arctic precipitation and CPW, in which the AO acts as a dynamical medium. Through the regression of a CPW index defined in the study, we establish the mechanism that connects the decadal variability of Arctic precipitation and CPW. A Rossby wave train driven by CPW propagates poleward into subpolar region of North Pacific (Figure 2.4c). The wave projects onto the climatological wavenumber 1 pattern in such a way as to decrease wavenumber 1 propagation into the stratosphere (Figure 2.6). This strengthens the vortex (Figure 2.5), which is manifested as tendency toward positive AO. This also increases moisture transport into the Arctic by synoptic eddies and thus increases Arctic precipitation (Figure 2.2). The signature of the mechanism also appears in the EP flux field when considering the difference between a period when the CPW index is high and when the CPW index is low (Figure 2.7).

Beyond identifying the mechanism, Chapter 2 also notes the differences in the mechanism and response of Arctic precipitation to CPW and EPW. Importantly, the location of the Rossby wave train generated by the SST anomaly is different in CPW and EPW (Figure 2.8). As a consequence, the Rossby wave train generated by EPW projects differently onto the climatological wavenumber 1 pattern (Figure 2.9), and the resulting effect on the polar stratospheric vortex and Arctic precipitation is of opposite sign (weakening vs. strengthening for the polar vortex and less vs. more Arctic precipitation for EPW and CPW, respectively). The implications of this difference, in the decadal sense, is that in a multi-year period where EPW is more common, Arctic cool-season precipitation will be less than in a multi-year period where CPW is more common. In the past 30 years, this has been manifested in the years 1996-2002 (EPW more common) and 1990-1995 (CPW more common). Thus, when considering the effects of an ENSO event on Arctic precipitation, the flavor of ENSO is important in determining the sign of the Arctic precipitation response.

Motivated by the results described in Chapter 2, we explored in Chapter 3 this differing effect of CPW and EPW on the polar vortex in an idealized model experiment in NCAR WACCM, focusing on the initial response of the vortex to CPW and EPW. In the model experimental setup, idealized patches of SST anomalies representing CPW and EPW (Figure 3.1) were used to explore the initial effects (i.e. in the first 40 days after the patch was introduced) of the SST anomalies on the strength of the stratospheric polar vortex. Twenty ensemble runs were conducted with different atmospheric initial conditions in each ensemble member and one CPW and EPW run per ensemble member. The effects of the SST patches were determined by comparing the results of the patch runs to a control run with identical initial conditions and DJF climatological SSTs. As a result of the introduction of the SST patches in the model, both CPW and EPW initially weaken the vortex in the ensemble average (Figure 3.2). By calculating each term that contributes to the zonal mean tendency in the QG zonal mean zonal momentum equation, we find that the vortex weakening is primarily driven by the changes in the mean meridional circulation and secondarily driven by the linear component of the eddy momentum flux (Figure 3.3). The linear component of the eddy momentum flux can be subdivided into the sum of terms representing the interaction of the forced variability with the initial condition and the internal variability of the vortex. In terms of the ensemble average, the negative contribution to the zonal mean zonal wind tendency originates with the interaction between forced variability the internal variability of the vortex (Figure 3.5).

In the individual members contained in the ensemble, there is a diverse initial response of the vortex strength to CPW and EPW, where the response in an individual ensemble member is not necessarily the same sign as the ensemble mean vortex response. The reason for the diverse response was the nature of the initial conditions of each ensemble member. In particular, the location of the planetary wavenumber 1 in the midlatitude initial conditions differed in each individual ensemble member (Figure 3.6). The magnitude of wave activity that propagates into the stratosphere and ultimately weakens the vortex is partly determined by how the generated Rossby waves project onto the planetary wavenumber 1 in the extratropics. The location of the wavenumber 1 wave in the initial conditions helps determine if the Rossby wave generated by CPW or EPW enhance or suppress the upward propagation of wave activity. In two ensemble members whose response was oppositely-signed relative to the ensemble mean, the magnitude of the MMC term played a role in determining the sign of the response (Figures 3.7-3.10). The MMC term in the stratosphere is positive in both cases, compared to a negative eddy momentum flux term.

The implications of the results in Chapter 3 are that the initial condition of extratropical flow and extratropical planetary wave pattern is important in determining the initial response to CPW and EPW. Thus, there is some variability in the response to CPW and EPW where the sign of the vortex response may be opposite of the mean initial vortex response to CPW and EPW. This may explain the variability in response of the vortex in CPW and EPW years in observations, where the location of the dominant extratropical wavenumber 1 pattern in each particular year may modify the vortex response to CPW and EPW.

In Chapter 4, we analyze the role of atmospheric eddy meridional heat transport and longwave and shortwave anomalies on the initial melt of Arctic sea ice. The initial sea ice melt data is derived from passive microwave satellite data (Drobot and Anderson 2001) and tracks the initial melt date of the sea ice surface. There has been a trend of earlier mean melt dates across the Arctic polar cap (north of 70°N) in the past 35 years, positively and significantly correlated with the decline in September minimum sea ice extent (Figure 4.1). Interestingly, if we view the mean melt date by 5-degree longitude sector around the pole, there is much interannual variability in the mean melt date by longitude sector (Figure 4.2). The trend towards an earlier melt date occurs mainly in the sectors north of Siberia and northwestern North America (90°E-130°W). There is no trend in meridional heat transport to explain the earlier melt in any sector (Figure 4.4c and 4.4d), but peak meridional transport events seem to be associated with individual melt events. Additionally, there are several adjacent sectors in particular years that show similar most common melt dates (i.e. similar mode values). This result suggests that a common feature might be driving the melt in these sectors, or in other words, this suggests the existence of discrete melt events. Figure 4.4a where there are peak melt events in many years in the 1979-2012 period.

Subsequently, we explore two of these identified melt events. In each case, there is a peak in total meridional heat transport at the event onset. By breaking down this total lower troposphere heat transport derived from MERRA reanalysis data into the direct eddy transport and cross terms, the product of the wind generated by high-frequency eddies and the mean temperature field are the largest component of the heat transport (Figure 4.5 and 4.7). Spatially, the melt area is associated with an area of positive total lower troposphere meridional heat transport (Figure 4.6 and 4.8). Also, in terms of downwelling SW and LW anomalies at the surface, a positive SW anomaly and total downwelling radiation anomaly are associated with the melt. The positive SW anomaly is coincident with a lack of clouds over the melt area. In the day immediately preceding the event, a positive LW anomaly is found over the area of initial melt (Figure 4.9) and associated with abundant cloud cover. On both dates, the anomalous cloud cover resulting in SW and LW anomalies is associated with atmospheric eddies.

The implication of the results in Chapter 4 is that both dynamic heat transport and thermodynamic mechanisms are important when determining the initial melt onset. Atmospheric eddies provide both a pathway for heat to be transported from lower latitudes and for changes in cloud cover and moisture to affect downwelling shortwave and longwave radiation at the surface. The combination of these two mechanisms contributes to the initial melt of Arctic sea ice. Since an early melt allows for more incoming shortwave absorption at the surface over the duration of the warm season in the Arctic, an early melt initialized by atmospheric eddies can have effects on the subsequent melt and minimum sea ice extent several months after the initial melt.

Atmospheric dynamics and thermodynamics play a role in both the warm and cool seasons, but the important dynamic and thermodynamic mechanisms differ. The differences come about because of the differences in the conditions in the Arctic in the warm and cool season and the different nature of the important climate phenomena in the lower latitudes. For example, incoming solar radiation is extremely low or nonexistent in the cool season, so longwave processes dominate in the Arctic during the cool season. Cloud cover is a crucial determinant of downwelling longwave radiative flux at the surface in winter. Conversely, shortwave processes are much more important in the warm season, where the flux of incoming solar radiation is greater and the surface albedo is sensitive to temperature anomalies, as soon as melt is initialized over the sea ice and snow cover. Dynamically, the Rossby wave train connection between the tropics and higher latitudes is important in the cool season, especially in terms of the influence of ENSO, a relatively persistent SST anomaly. High and low frequency eddies in all seasons both directly transport heat poleward from lower latitudes and directly affect the distribution of cloud cover over the Arctic region.

5.2 Future Work

We have explored the details of a few connecting mechanisms, and in future work, the interactions between lower latitudes and the Arctic will continue to be explored to better understand the complexity of Arctic climate variability. The theme presented in this dissertation provides the framework for the present investigation and future work. The goal of future work will be to establish an *integrative* view of what drives the trend and multi-scale variability of Arctic hydroclimate features, such as Arctic sea ice cover. The integrative view will include atmospheric mechanisms that couple the Arctic to other regions, linking Arctic variability to climate variability in those regions. The linking mechanisms may contain dynamical components (e.g. heat transport) or thermodynamic components (e.g. cloud cover changes and accompanying changes in surface downwelling SW and LW radiation) that help facilitate the link. As the results in this dissertation have shown, atmospheric eddies and Rossby wave trains are important mechanisms that facilitate the interaction of the Arctic with lower latitudes. In the case of atmospheric eddies, the eddies are associated with many important dynamical and thermodynamical processes that affect the Arctic hydroclimate and that can serve as part of a physical mechanism linking the Arctic hydroclimate to lower latitude climate variability.

In the most immediate future work, the time period of focus where the framework will be applied will be the initial melt of Arctic sea ice at the onset of the warm season in late boreal spring. Later work will use the framework to investigate another period crucial to the Arctic hydroclimate, the freeze-up of sea ice at the end of the warm season. After establishing the role of dynamics and thermodynamics in the initial melt in observation-based data, the established relationship will be used to evaluate the initial sea ice melt in coupled climate models (e.g. the NCAR CESM) and identify the source of potential model biases.

The work presented here helps improve our understanding of how the lower latitudes interact with the climate variability of the Arctic in both the cool and warm seasons. Because of the visibility of the trend and variability of sea ice cover and the economic interest in an ice-free Arctic Ocean, much interest in recent years has been directed to the study of the trend and variability of Arctic sea ice cover. Additionally, because of the larger increase in temperatures relative to the global mean (i.e. Arctic amplification, e.g. Chylek et al. 2009), the Arctic, as a region, is at the forefront of climate change. Therefore the work presented here is a significant contribution to the understanding of the crucial changes in the Arctic. By extension, the work increases our understanding of the changes and variability in the global climate system, since the Arctic is an integral part of the global climate system.

REFERENCES

Adler, R. F., and Coauthors, 2003: The version-2 global precipitation climatology project (GPCP) monthly precipitation analysis (1979-present). *Journal of Hydrometeorology*, **4,** 1147-1167.

Agarwal, S., W. Moon, and J. S. Wettlaufer, 2011: Decadal to seasonal variability of Arctic sea ice albedo. *Geophys Res Lett*, **38**. L20504.

Andreas, E. L., C. A. Paulson, R. M. Williams, R. W. Lindsay, and J. A. Businger, 1979: Turbluent Heat-Flux from Arctic Leads. *Bound.-Layer Meteor.*, **17,** 57-91.

Andrews, D. G., J. R. Holton, and C. B. Leovy, 1987: *Middle atmosphere dynamics.* Academic Press, xi, 489 p.

Ashok, K., S. K. Behera, S. A. Rao, H. Y. Weng, and T. Yamagata, 2007: El Nino Modoki and its possible teleconnection. *J Geophys Res-Oceans*, **112**. C11007.

Baldwin, M. P., and T. J. Dunkerton, 1999: Propagation of the Arctic Oscillation from the stratosphere to the troposphere. *J Geophys Res-Atmos*, **104,** 30937-30946.

Barsugli, J. J., and P. D. Sardeshmukh, 2002: Global atmospheric sensitivity to tropical SST anomalies throughout the Indo-Pacific basin. *Journal of Climate*, **15,** 3427-3442.

Belchansky, G. I., D. C. Douglas, and N. G. Platonov, 2004: Duration of the Arctic Sea ice melt season: Regional and interannual variability, 1979-2001. *Journal of Climate*, **17,** 67-80.

Bell, C. J., L. J. Gray, A. J. Charlton-Perez, M. M. Joshi, and A. A. Scaife, 2009: Stratospheric Communication of El Nino Teleconnections to European Winter. *Journal of Climate*, **22,** 4083-4096.

Black, R. X., 2002: Stratospheric forcing of surface climate in the Arctic oscillation. *Journal of Climate*, **15,** 268-277.

Blackmon, M. L., 1976: Climatological Spectral Study of 500 mb Geopotential Height of Northern Hemisphere *J Atmos Sci*, **33,** 1607-1623.

Bosilovich, M. G., J. Y. Chen, F. R. Robertson, and R. F. Adler, 2008: Evaluation of global precipitation in reanalyses. *J Appl Meteorol Clim*, **47,** 2279-2299.

Cai, M., 2005: Dynamical amplification of polar warming. *Geophys Res Lett*, **32**. L22710.

Calvo, N., and D. R. Marsh, 2011: The combined effects of ENSO and the 11 year solar cycle on the Northern Hemisphere polar stratosphere. *J Geophys Res-Atmos*, **116**. D23112.

Chang, E. K. M., S. Y. Lee, and K. L. Swanson, 2002: Storm track dynamics. *Journal of Climate*, **15,** 2163-2183.

Charney, J. G., and P. G. Drazin, 1961: Propagation of Planetary-Scale Disturbances from Lower into Upper Atmosphere. *Journal of Geophysical Research*, **66,** 83.

Chylek, P., C. K. Folland, G. Lesins, M. K. Dubey, and M. Y. Wang, 2009: Arctic air temperature change amplification and the Atlantic Multidecadal Oscillation. *Geophys Res Lett*, **36**. L14801.

Comiso, J. C., C. L. Parkinson, R. Gersten, and L. Stock, 2008: Accelerated decline in the Arctic Sea ice cover. *Geophys Res Lett*, **35**. L01703.

Deng, Y., and M. Mak, 2005: An idealized model study relevant to the dynamics of the midwinter minimum of the Pacific storm track. *J Atmos Sci*, **62,** 1209-1225.

Deng, Y., and M. Mak, 2006: Nature of the differences in the intraseasonal variability of the Pacific and Atlantic storm tracks: A diagnostic study. *J Atmos Sci*, **63,** 2602-2615.

Deser, C., J. E. Walsh, and M. S. Timlin, 2000: Arctic sea ice variability in the context of recent atmospheric circulation trends. *Journal of Climate*, **13,** 617-633.

Dickson, R. R., and Coauthors, 2000: The Arctic Ocean response to the North Atlantic oscillation. *Journal of Climate*, **13,** 2671-2696.

Ding, Q. H., B. Wang, J. M. Wallace, and G. Branstator, 2011: Tropical-Extratropical Teleconnections in Boreal Summer: Observed Interannual Variability. *Journal of Climate*, **24,** 1878-1896.

Dong, X. Q., and Coauthors, 2014: Critical mechanisms for the formation of extreme arctic sea-ice extent in the summers of 2007 and 1996. *Clim Dynam*, **43,** 53-70.

Drobot, S. D., and M. R. Anderson, 2001: An improved method for determining snowmelt onset dates over Arctic sea ice using scanning multichannel microwave radiometer and Special Sensor Microwave/Imager data. *J Geophys Res-Atmos*, **106,** 24033-24049.

Eastman, R., and S. G. Warren, 2010: Interannual Variations of Arctic Cloud Types in Relation to Sea Ice. *Journal of Climate*, **23,** 4216-4232.

Edmon, H. J., B. J. Hoskins, and M. E. Mcintyre, 1980: Eliassen-Palm Cross-Sections for the Troposphere. *J Atmos Sci*, **37,** 2600-2616.

Fletcher, C. G., and P. J. Kushner, 2011: The Role of Linear Interference in the Annular Mode Response to Tropical SST Forcing. *Journal of Climate*, **24,** 778-794.

Garcia, R. R., D. R. Marsh, D. E. Kinnison, B. A. Boville, and F. Sassi, 2007: Simulation of secular trends in the middle atmosphere, 1950-2003. *J Geophys Res-Atmos*, **112**. D09301.

Garfinkel, C. I., and D. L. Hartmann, 2007: Effects of the El Nino-Southern Oscillation and the Quasi-Biennial Oscillation on polar temperatures in the stratosphere. *J Geophys Res-Atmos*, **112**. D19112.

Garfinkel, C. I., and D. L. Hartmann, 2008: Different ENSO teleconnections and their effects on the stratospheric polar vortex. *J Geophys Res-Atmos*, **113**. D18114.

Garfinkel, C. I., D. L. Hartmann, and F. Sassi, 2010: Tropospheric Precursors of Anomalous Northern Hemisphere Stratospheric Polar Vortices. *Journal of Climate*, **23,** 3282-3299.

Garfinkel, C. I., M. M. Hurwitz, D. W. Waugh, and A. H. Butler, 2012: Are the Teleconnections of Central and Eastern Pacific El Nino Distinct in Boreal Wintertime? *Clim Dynam*.

Graf, H. F., and D. Zanchettin, 2012: Central Pacific El Nino, the "subtropical bridge," and Eurasian climate. *J Geophys Res-Atmos*, **117**. D01102.

Graversen, R. G., and M. H. Wang, 2009: Polar amplification in a coupled climate model with locked albedo. *Clim Dynam*, **33,** 629-643.

Graversen, R. G., T. Mauritsen, S. Drijfhout, M. Tjernstrom, and S. Martensson, 2011: Warm winds from the Pacific caused extensive Arctic sea-ice melt in summer 2007. *Clim Dynam*, **36,** 2103-2112.

Hegyi, B. M., and Y. Deng, 2011: A dynamical fingerprint of tropical Pacific sea surface temperatures on the decadal-scale variability of cool-season Arctic precipitation. *J Geophys Res-Atmos*, **116**. D20121.

Hegyi, B. M., Y. Deng, R. X. Black, and R. J. Zhou, 2014: Initial Transient Response of the Winter Polar Stratospheric Vortex to Idealized Equatorial Pacific Sea Surface Temperature Anomalies in the NCAR WACCM. *Journal of Climate*, **27,** 2699-2713.

Holton, J. R., 2004: *An Introduction to Dynamic Meteorology*. 4th ed. Elsevier Academic Press, 535 pp.

Horel, J. D., and J. M. Wallace, 1981: Planetary-Scale Atmospheric Phenomena Associated with the Southern Oscillation. *Mon Weather Rev*, **109,** 813-829.

Hoskins, B. J., and D. J. Karoly, 1981: The Steady Linear Response of a Spherical Atmosphere to Thermal and Orographic Forcing. *J Atmos Sci*, **38,** 1179-1196.

Huntington, H., and Coauthors, 2005: Arctic climate: Past and present, in Arctic Climate Impact Assessment, edited by C. Symon, L. Arris, and B. Heal, Cambridge Univ. Press, New York, pp. 1-20.

Ineson, S., and A. A. Scaife, 2009: The role of the stratosphere in the European climate response to El Nino. *Nat Geosci*, **2,** 32-36.

Intrieri, J. M., C. W. Fairall, M. D. Shupe, P. O. G. Persson, E. L. Andreas, P. S. Guest, and R. E. Moritz, 2002: An annual cycle of Arctic surface cloud forcing at SHEBA. *J Geophys Res-Oceans*, **107**.

Jia, X. J., H. Lin, and J. Derome, 2009: The influence of tropical Pacific forcing on the Arctic Oscillation. *Clim Dynam*, **32,** 495-509.

Kao, H. Y., and J. Y. Yu, 2009: Contrasting Eastern-Pacific and Central-Pacific Types of ENSO. *Journal of Climate*, **22,** 615-632.

Kay, J. E., and A. Gettelman, 2009: Cloud influence on and response to seasonal Arctic sea ice loss. *J Geophys Res-Atmos*, **114**. D18204.

King, M. P., and F. Kucharski, 2006: Observed low-frequency covariabilities between the tropical oceans and the North Atlantic Oscillation in the twentieth century. *Journal of Climate*, **19,** 1032-1041.

Kucharski, F., F. Molteni, and A. Bracco, 2006: Decadal interactions between the western tropical Pacific and the North Atlantic Oscillation. *Clim Dynam*, **26,** 79-91.

L'Heureux, M. L., A. Kumar, G. D. Bell, M. S. Halpert, and R. W. Higgins, 2008: Role of the Pacific-North American (PNA) pattern in the 2007 Arctic sea ice decline. *Geophys Res Lett*, **35**. L20701.

Lee, S., 2012: Testing of the Tropically Excited Arctic Warming Mechanism (TEAM) with Traditional El Nino and La Nina. *Journal of Climate*, **25,** 4015-4022.

Lee, S., S. Feldstein, D. Pollard, and T. White, 2011: Do Planetary Wave Dynamics Contribute to Equable Climates? *Journal of Climate*, **24,** 2391-2404.

Liebmann, B., and C. A. Smith, 1996: Description of a complete (interpolated) outgoing longwave radiation dataset. *B Am Meteorol Soc*, **77,** 1275-1277.

Lindsay, R., M. Wensnahan, A. Schweiger, and J. Zhang, 2014: Evaluation of Seven Different Atmospheric Reanalysis Products in the Arctic. *Journal of Climate*, **27,** 2588-2606.

Manabe, S., and R. T. Wetherald, 1975: Effects of Doubling CO2 Concentration on Climate of a General Circulation Model. *J Atmos Sci*, **32,** 3-15.

Markus, T., J. C. Stroeve, and J. Miller, 2009: Recent changes in Arctic sea ice melt onset, freezeup, and melt season length. *J Geophys Res-Oceans*, **114**. C12024.

Matsuno, T., 1970: Vertical Propagation of Stationary Planetary Waves in Winter Northern Hemisphere. *J Atmos Sci*, **27,** 871-883.

McBean, G., and Coauthors, 2005: An Introduction to the Arctic Climate Impact Assessment, edited by C. Symon, L. Arris, and B. Heal, Cambridge Univ. Press, New York, pp. 21–60.

Naoe, H., and K. Shibata, 2010: Equatorial quasi-biennial oscillation influence on northern winter extratropical circulation. *J Geophys Res-Atmos*, **115**. D19102.

Nishii, K., H. Nakamura, and T. Miyasaka, 2009: Modulations in the planetary wave field induced by upward-propagating Rossby wave packets prior to stratospheric sudden warming events: A case-study. *Q J Roy Meteor Soc*, **135,** 39-52.

Nishii, K., H. Nakamura, and Y. J. Orsolini, 2011: Geographical Dependence Observed in Blocking High Influence on the Stratospheric Variability through Enhancement and Suppression of Upward Planetary-Wave Propagation. *Journal of Climate*, **24,** 6408-6423.

Ogi, M., and J. M. Wallace, 2012: The role of summer surface wind anomalies in the summer Arctic sea ice extent in 2010 and 2011. *Geophys Res Lett*, **39**. L09704.

Ogi, M., I. G. Rigor, M. G. McPhee, and J. M. Wallace, 2008: Summer retreat of Arctic sea ice: Role of summer winds. *Geophys Res Lett*, **35**. L24701.

Parkinson, C. L., and D. J. Cavalieri, 2008: Arctic sea ice variability and trends, 1979-2006. *J Geophys Res-Oceans*, **113**. C07003.

Perovich, D. K., and C. Polashenski, 2012: Albedo evolution of seasonal Arctic sea ice. *Geophys Res Lett*, **39**. L08501.

Perovich, D. K., S. V. Nghiem, T. Markus, and A. Schweiger, 2007: Seasonal evolution and interannual variability of the local solar energy absorbed by the Arctic sea ice-ocean system. *J Geophys Res-Oceans*, **112**. C03005.

Peixoto, J. P., and A. H. Oort, 2004: Physics of Climate, Am. Inst. of Phys., New York.

Plumb, R. A., 1985: On the 3-Dimensional Propagation of Stationary Waves. *J Atmos Sci*, **42,** 217-229.

Polvani, L. M., and D. W. Waugh, 2004: Upward wave activity flux as a precursor to extreme stratospheric events and subsequent anomalous surface weather regimes. *Journal of Climate*, **17,** 3548-3554.

Rayner, N. A., and Coauthors, 2003: Global analyses of sea surface temperature, sea ice, and night marine air temperature since the late nineteenth century. *J Geophys Res-Atmos*, **108**.

Rienecker, M. M., and Coauthors, 2011: MERRA: NASA's Modern-Era Retrospective Analysis for Research and Applications. *Journal of Climate*, **24,** 3624-3648.

Rigor, I. G., J. M. Wallace, and R. L. Colony, 2002: Response of sea ice to the Arctic oscillation. *Journal of Climate*, **15,** 2648-2663.

Sardeshmukh, P. D., and B. J. Hoskins, 1988: The Generation of Global Rotational Flow by Steady Idealized Tropical Divergence. *J Atmos Sci*, **45,** 1228-1251.

Sassi, F., D. Kinnison, B. A. Boville, R. R. Garcia, and R. Roble, 2004: Effect of El Nino-Southern Oscillation on the dynamical, thermal, and chemical structure of the middle atmosphere. *J Geophys Res-Atmos*, **109**. D17108.

Screen, J. A., I. Simmonds, and K. Keay, 2011: Dramatic interannual changes of perennial Arctic sea ice linked to abnormal summer storm activity. *J Geophys Res-Atmos*, **116**. D15105.

Serreze, M. C., and R. G. Barry, 2011: Processes and impacts of Arctic amplification: A research synthesis. *Global and Planetary Change*, **77,** 85-96.

Serreze, M. C., A. H. Lynch, and M. P. Clark, 2001: The Arctic frontal zone as seen in the NCEP-NCAR reanalysis. *Journal of Climate*, **14,** 1550-1567.

Serreze, M. C., F. Carse, R. G. Barry, and J. C. Rogers, 1997: Icelandic low cyclone activity: Climatological features, linkages with the NAG, and relationships with recent changes in the Northern Hemisphere circulation. *Journal of Climate*, **10,** 453-464.

Shimada, K., and Coauthors, 2006: Pacific Ocean inflow: Influence on catastrophic reduction of sea ice cover in the Arctic Ocean. *Geophys Res Lett*, **33**. L08605.

Simmonds, I., C. Burke, and K. Keay, 2008: Arctic Climate Change as Manifest in Cyclone Behavior. *Journal of Climate*, **21,** 5777-5796.

Smith, K. L., C. G. Fletcher, and P. J. Kushner, 2010: The Role of Linear Interference in the Annular Mode Response to Extratropical Surface Forcing. *Journal of Climate*, **23,** 6036-6050.

Sorteberg, A., and J. E. Walsh, 2008: Seasonal cyclone variability at 70 degrees N and its impact on moisture transport into the Arctic. *Tellus A*, **60,** 570-586.

Stroeve, J. C., T. Markus, L. Boisvert, J. Miller, and A. Barrett, 2014: Changes in Arctic melt season and implications for sea ice loss. *Geophys Res Lett*, **41,** 1216-1225. doi: 10.1002/2013GL058951.

Sun, F. P., and J. Y. Yu, 2009: A 10-15-Yr Modulation Cycle of ENSO Intensity. *Journal of Climate*, **22,** 1718-1735.

Sura, P., and J. Barsugli, 2002: A note on estimating drift and diffusion parameters from timeseries. *Phys Lett A*, **305,** 304-311.

Taguchi, M., 2010: Wave Driving in the Tropical Lower Stratosphere as Simulated by WACCM. Part II: ENSO-Induced Changes for Northern Winter. *J Atmos Sci*, **67,** 543-555.

Taguchi, M., and D. L. Hartmann, 2006: Increased occurrence of stratospheric sudden warmings during El Nino as simulated by WACCM. *Journal of Climate*, **19,** 324-332.

Takaya, K., and H. Nakamura, 2001: A formulation of a phase-independent wave-activity flux for stationary and migratory quasigeostrophic eddies on a zonally varying basic flow. *J Atmos Sci*, **58,** 608-627.

Taylor, P. C., M. Cai, A. X. Hu, J. Meehl, W. Washington, and G. J. Zhang, 2013: A Decomposition of Feedback Contributions to Polar Warming Amplification. *Journal of Climate*, **26,** 7023-7043.

Thompson, D. W. J., and J. M. Wallace, 1998: The Arctic Oscillation signature in the wintertime geopotential height and temperature fields. *Geophys Res Lett*, **25,** 1297-1300.

Thompson, D. W. J., and J. M. Wallace, 2000: Annular modes in the extratropical circulation. Part I: Month-to-month variability. *Journal of Climate*, **13,** 1000-1016.

Wallace, J. M., and D. S. Gutzler, 1981: Teleconnections in the Geopotential Height Field during the Northern Hemisphere Winter. *Mon Weather Rev*, **109,** 784-812.

Wang, J., and Coauthors, 2009: Is the Dipole Anomaly a major driver to record lows in Arctic summer sea ice extent? *Geophys Res Lett*, **36**. L05706.

Waugh, D. W., and L. M. Polvani, 2010: Stratospheric Polar Vortices. *Stratosphere: Dynamics, Transport, and Chemistry*, L. M. Polvani, A. H. Sobel, and D. W. Waugh, Eds., Amer Geophysical Union, 43-57.

Weng, H. Y., S. K. Behera, and T. Yamagata, 2009: Anomalous winter climate conditions in the Pacific rim during recent El NiA +/- o Modoki and El NiA +/- o events. *Clim Dynam*, **32,** 663-674.

Wielicki, B. A., B. R. Barkstrom, E. F. Harrison, R. B. Lee, G. L. Smith, and J. E. Cooper, 1996: Clouds and the earth's radiant energy system (CERES): An earth observing system experiment. *B Am Meteorol Soc*, **77,** 853-868.

Winton, M., 2006: Amplified Arctic climate change: What does surface albedo feedback have to do with it? *Geophys Res Lett*, **33**. L03701.

Woods, C., R. Caballero, and G. Svensson, 2013: Large-scale circulation associated with moisture intrusions into the Arctic during winter. *Geophys Res Lett*, **40,** 4717-4721.

Woollings, T., A. Charlton-Perez, S. Ineson, A. G. Marshall, and G. Masato, 2010: Associations between stratospheric variability and tropospheric blocking. *J Geophys Res-Atmos*, **115**. D06108.

Xie, F., J. Li, W. Tian, J. Feng, and Y. Huo, 2012: Signals of El Nino Modoki in the tropical tropopause layer and stratosphere. *Atmos Chem Phys*, **12,** 5259-5273.

Xie, P. P., and P. A. Arkin, 1997: Global precipitation: A 17-year monthly analysis based on gauge observations, satellite estimates, and numerical model outputs. *B Am Meteorol Soc*, **78,** 2539-2558.

Yang, X. Y., J. C. Fyfe, and G. M. Flato, 2010: The role of poleward energy transport in Arctic temperature evolution. *Geophys Res Lett*, **37**. L14803.

Yu, J. Y., and H. Y. Kao, 2007: Decadal changes of ENSO persistence barrier in SST and ocean heat content indices: 1958-2001. *J Geophys Res-Atmos*, **112**. D13106.

Yu, J. Y., and S. T. Kim, 2010: Three evolution patterns of Central-Pacific El Nino. *Geophys Res Lett*, **37**. L08706.

Zhang, J. L., R. Lindsay, M. Steele, and A. Schweiger, 2008: What drove the dramatic retreat of arctic sea ice during summer 2007? *Geophys Res Lett*, **35**. L11505.

Zhang, X. D., J. E. Walsh, J. Zhang, U. S. Bhatt, and M. Ikeda, 2004: Climatology and interannual variability of arctic cyclone activity: 1948-2002. *Journal of Climate*, **17,** 2300-2317.